

Silicon photonic sensors based on low-cost optical sources

by

Leanne Dias

B. Eng. & Mgmt., McMaster University, 2018

A THESIS SUBMITTED IN PARTIAL FULFILLMENT
OF THE REQUIREMENTS FOR THE DEGREE OF

Master of Applied Science

in

THE FACULTY OF GRADUATE AND POSTDOCTORAL
STUDIES

(Electrical and Computer Engineering)

The University of British Columbia
(Vancouver)

June 2021

© Leanne Dias, 2021

The following individuals certify that they have read, and recommend to the Faculty of Graduate and Postdoctoral Studies for acceptance, the thesis entitled:

Silicon photonic sensors based on low-cost optical sources

submitted by **Leanne Dias** in partial fulfillment of the requirements for the degree of **Master of Applied Science in Electrical and Computer Engineering**.

Examining Committee:

Lukas Chrostowski, Professor, Electrical and Computer Engineering, UBC
Co-Supervisor

Sudip Shekhar, Associate Professor, Electrical and Computer Engineering, UBC
Co-Supervisor

Nicolas A.F. Jaeger, Professor, Electrical and Computer Engineering, UBC
Additional Examiner

Abstract

Silicon photonic (SiPh) sensors hold tremendous potential for the advancement of global healthcare. Leveraging mature complementary metal-oxide semiconductor (CMOS) foundry processes, hundreds of SiPh sensors can be integrated into tiny devices, enabling the detection of multiple pathogens, and eliminating the need for expensive in-lab chemical processing. While the performance of SiPh sensors is similar to clinical standards, the implementation costs remain quite high. To realize the potential that SiPh sensor systems hold for global healthcare, their overall cost must be reduced.

SiPh sensors typically rely on high-resolution tunable lasers, which remain an expensive off-chip component. This thesis first summarizes alternative optical sources that are used for SiPh sensors. Fixed-wavelength lasers are a low-cost alternative, and benefit from relative ease of coupling to chip. Unfortunately, the corresponding sensor designs are very sensitive to noise. Broadband optical sources are another lower-cost alternative source; however, their use often requires expensive detection equipment. Despite their drawbacks, implementing these alternative optical sources could significantly reduce the overall cost of a SiPh system..

Three low-cost SiPh architectures are presented in this thesis: two that use a broadband source, and one that uses a fixed-wavelength laser. The broadband SiPh architectures use a sensor-tracker system, where one component, a microring resonator (MRR) or a Mach-Zehnder interferometer (MZI), acts as a sensor and a second component acts as a tracker (by electrically tracking wavelength shifts). Since wavelength shifts from the sensor can be read as electrical power shifts in the tracker, this system eliminates the need for expensive detection equipment. Sensitivity values of 78.9 nm/RIU (refractive index unit) and 218.5 nm/RIU were

obtained, with system limits of detection of 3.4×10^{-4} RIU and 7.7×10^{-4} RIU for the MRR and MZI designs, respectively.

In the fixed-wavelength system, a heater-detector tuning element is placed in the MRR loop. This similarly enables electrical tracking of wavelength shifts, thus reducing the noise sensitivity commonly found in fixed-wavelength systems. Simulation results report sensitivities up to 76 nm/RIU, with calculated intrinsic limits of detection down to 3.8×10^{-4} RIU. The results obtained demonstrates that high-resolution tunable lasers are not required to achieve high sensor performance.

Lay Summary

Miniaturized biosensing devices are crucial for the advancement of global healthcare as they offer fast, reliable, and affordable detection of pathogens, viruses, and bacteria. Silicon-based photonic sensors can perform real-time sensing measurements, eliminating long wait times and the need for expensive chemical lab equipment. These sensors are compatible with the fabrication processes used for electronic devices, allowing them to be made at a very low cost. However, silicon photonic sensors require a light source, which is typically a tunable laser. Since these lasers cannot currently be fabricated easily, this drastically increases the overall cost of the system. For these sensors to make an impact in global healthcare, a low-cost alternative for light sources must be implemented. This thesis presents three low-cost sensor designs that do not rely on tunable lasers, thus lowering the overall system cost and providing a path forward for the realization of silicon photonic sensing systems.

Preface

The content of this thesis is based on two published publications. Section 3.1.1 is partly based on the following conference publication:

1. **L. Dias**, E. Luan, H. Shoman, H. Jayatileka, S. Shekhar, L. Chrostowski, and N. A. F. Jaeger, “Cost-effective, CMOS-compatible, label-free biosensors using doped silicon detectors and a broadband source.” CLEO: Applications and Technology. Optical Society of America, 2019.

I am the main contributor to this publication. N. A. F. Jaeger conceived the idea, which is an extension of work from H. Shoman and H. Jayatileka. H. Shoman designed the chip. I performed the primary measurement and analysis of the devices, with H. Shoman providing support for the electronics measurements. E. Luan contributed to the chip packaging and microfluidics integration for this project. E. Luan and I performed the biosensing measurements and analysis. E. Luan, H. Shoman, and I composed the manuscript. S. Shekhar, L. Chrostowski, and N. A. F. Jaeger supervised the project. A full version of this publication is in the process of being submitted, of which I am also the primary author.

Section 3.1.2 is based on unpublished work, of which I am the main contributor. L. Chrostowski conceived the idea. I designed, measured, and analyzed the fabricated devices. The results from this section may be published at a later date.

Section 3.2 is partly based on the following invited publication:

2. L. Chrostowski, **L. Dias**, M. Mitchell, C. Mosquera, E. Luan, M. Al-Qadasi, A. Randhawa, H. R. Mojaver, E. Lyall, A. Gervais, R. Dubé-Demers, K. Awan, S. Gou, O. Liboiron-Ladouceur, W. Shi, S. Shekhar, K. C. Cheung, “A silicon photonic evanescent-field sensor architecture using a fixed-

wavelength laser.” *Optical Interconnects XXI*. Vol. 11692. International Society for Optics and Photonics, 2021.

This project involved many contributors. For the sake of brevity, I will only mention contributions that are discussed within this thesis. L. Chrostowski conceived the idea. C. Mosquera and L. Chrostowski designed the chip layout, with design parameters supported by simulations that I performed. L. Chrostowski and I simulated the performance of the sensor. H. R. Mojaver collected the measurement data from the device, and I performed the data analysis. Full results from this design have yet to be published.

Table of Contents

Abstract	iii
Lay Summary	v
Preface	vi
Table of Contents	viii
List of Tables	x
List of Figures	xii
Glossary	xx
Acknowledgments	xxii
1 Introduction	1
1.1 Research background	1
1.2 Silicon photonics	2
1.3 Biosensing with integrated photonics	3
1.4 System implementation	4
1.5 Thesis objective	6
1.6 Thesis structure	7
2 Review of system components	8
2.1 Integrated photonic sensor components	8

2.1.1	Waveguides	9
2.1.2	Mach-Zehnder interferometers (MZI)	12
2.1.3	Microring resonators (MRR)	14
2.1.4	Other sensor structures	16
2.1.5	Summary	16
2.2	Optical sources	17
2.2.1	Tunable lasers	17
2.2.2	Fixed-wavelength lasers	20
2.2.3	Broadband sources	21
2.2.4	Summary	24
3	Research contributions	25
3.1	Broadband designs	25
3.1.1	Broadband MRR design	25
3.1.2	Broadband MZI design	36
3.1.3	Comparison of architectures	44
3.1.4	Design benefits and optimization	49
3.2	Fixed-wavelength laser design	51
3.2.1	Operating principles	52
3.2.2	Design and fabrication	52
3.2.3	Results	56
4	Conclusion	60
4.1	Future work	61
4.1.1	Broadband design	62
4.1.2	Fixed-wavelength laser design	62
4.1.3	Overall design considerations	63
	Bibliography	64
A	EECE 584 and ELEC 581 project reports	78

List of Tables

Table 1.1	Comparison of SPR and SiPh sensor performance (analysis time and sLoD) for selected target analytes.	4
Table 2.1	Summary of key considerations when choosing an optical source for a SiPh sensing platform. PWBs have not been demonstrated with broadband sources, and have yet to be demonstrated at high-volume for fixed-wavelength lasers. The optical intensity noise will effect the sLoD in intensity-based approaches for fixed-wavelength laser systems; however, optical intensity variations should not effect other approaches.	24
Table 3.1	Summary of the remaining power incident on the photodetector after accounting for losses in each sensor design. After accounting for losses in the broadband designs, the final power must also be multiplied by the percent power corresponding to the design’s transmission curve (Lorentzian or sinusoidal). . . .	31
Table 3.2	Summary of broadband MZI results. The designed and measured FSRs are within 5% tolerance, with deviations due to fabrication variations. With the exception of MZI ₃ , the sLoDs are within commonly reported SiPh sensor ranges.	38

Table 3.3	Summary of key FOMs for the broadband MRR and MZI designs. Sensitivity in nm/RIU or rad/RIU represents a more accurate representation, as it is not dependent on the heater efficiency. sLOD is difficult to compare as the system noise was not constant across measurements.	46
Table 3.4	Simulated versus measured sensitivities for the broadband designs. The measured values from the isopropyl alcohol experiment match well with simulated values. The sensitivity extracted from the thermal tuning experiments for the MRR produced a higher value than expected, likely due to the refractive index change not being isolated to the cladding. The MZI designs have lower sensitivities than expected, likely arising from the nonlinearity in their tracking method or manufacturing variations.	47
Table 3.5	Summary of preliminary results for the fixed-wavelength MRR architecture.	58

List of Figures

Figure 2.1	a) A standard waveguide, where n_1 refractive index of the waveguide core, and n_2 and n_3 are the refractive indices of the waveguide cladding. In SiPh sensors, the n_3 layer is the solution containing the target analyte. b) The fundamental waveguide mode, as simulated by Lumerical's MODE. The effective index can be extracted.	9
Figure 2.2	a) The evanescent field extends past the silicon waveguide and into the cladding. By functionalizing the surface of the waveguide (green structures), specific analytes (yellow) can bind to the surface and change the effective index. This change will alter the propagation behaviour of light, as in b), where the transmission is shifted $\Delta\lambda$ after molecule binding.	10
Figure 2.3	a) A sub-wavelength gratings (SWG) waveguide structure. The width (w), period (Λ), and depths of both the high and low index blocks (a and b , respectively) are labelled. b) The mode profile of an SWG waveguide. More energy is outside of the silicon core compared to the optical propagation in a straight waveguide (Fig 2.1).	12
Figure 2.4	a) Basic design of a Mach-Zehnder interferometer. b) Typical transmission spectrum from the output, when a path length imbalance (ΔL) exists between the arm.	13

Figure 2.5	a) Basic design of a add-drop microring resonator. b) Typical transmission spectrum as measured from the through port (blue) and drop port (orange) of the ring. The FSR and $\Delta\lambda_{FWHM}$ are labelled.	14
Figure 2.6	Overview of typical sensing setups making use of a) a tunable laser, b) a fixed-wavelength laser, or c) a broadband source. a) The laser wavelength is swept and the output is coupled to the SiPh chip, where it passes through a sensor and is then detected with an on-chip PD. A typical output spectrum is shown on the right, where optical power is a function of wavelength, and the transmission spectrum shifts when the sensor is exposed to an analyte (t_1 and t_2 are before and after analyte exposure, respectively). b) A fixed-wavelength laser is coupled on-chip, where it passes through a sensor and is then detected with an on-chip PD. The typical output spectrum is shown on the right, where optical power is a function of time, since only a single wavelength is being detected. As the sensor is exposed to a sample, the detected optical power will shift due to a change in alignment between the fixed-wavelength input and the sensor's transmission spectrum from t_1 to t_2 , before and after exposure to a sample, respectively. c) The broadband source (containing all wavelengths over a given bandwidth) is coupled to the SiPh chip, where it passes through a sensor, and is then coupled off chip to an OSA. The typical output spectrum is shown on the right, where optical power is a function of wavelength, and the transmission spectrum shifts from t_1 to t_2 , before and after exposure to a sample, respectively.	18

Figure 2.7	a) Broadband sensor-tracker design layout, proposed by Song et al. [103]. b) Transmission spectra of sensor and tracker microrings (first column) and the resultant output (second column). Initially the ring resonances are aligned, producing a peak output transmission. When the sensor resonance shifts due to a change in the effective index, Δn , the total optical power output is lowered. The tracker resonance is realigned to the sensor by applying a power, ΔW . By monitoring the ΔW required to keep the resonances aligned, the Δn caused by the target analyte can be extracted. (Here the output is shown as a function of wavelength, however, this design measures the photocurrent collected by the PD, which is essentially the integral of these output curves. Spectral information is not required in this design.)	23
Figure 3.1	(a) Layout of the photonic sensor, consisting of two MRRs, a sensor and a tracker, using a broadband source. (b) Cross-section of IRPHD tracking MRR. (c) Simulated transmission of the drop-ports of both MRRs. The grey area corresponds to the 6-nm bandwidth that is measured.	27
Figure 3.2	(a) Block diagram of our experimental setup, with measured spectrum shown to the right. A SLED broadband source was filtered using a bandpass tunable filter (BPTF) and amplified by an erbium-doped fiber amplifier (EDFA) before being coupled on chip. (b) Optical microscope image of a test device. Here we include a thermally-tunable ring to simulate a biosensing experiment, and a germanium photodetector (Ge PD) to compare to our doped detectors (IRPHDs).	28

Figure 3.3	(a) Experimental setup used for the measurements in (b) and (c). An SLED broadband source was filtered using a BPTF and amplified with an EDFA before being coupled on chip using grating couplers (GCs). The sensor and tracker MRR were electrically controlled using an off-chip source meter. The photocurrent from the IRPHD and Ge PD was also measured using the off-chip source meter. (b) The IRPHD photocurrent as a function of the tracking ring voltage at various sensing ring voltages (indicated as legends on the line plots). (c) Tracker voltage to maximize the photocurrent (from the IRPHD and Ge PD) at various sensing ring voltage setpoints across time, implemented using a maximum search algorithm (the dither signal can be seen).	32
Figure 3.4	System noise of the (a) IRPHD architecture and (b) GePD architecture, measured for 2.5 min and 10 min, respectively. Inset: Histogram of noise distribution with standard deviation results.	34
Figure 3.5	a) Experimental setup used for the measurements in b). An SLED broadband source was filtered using a BPTF and amplified with an EDFA before being coupled on chip using GCs. The sensor had a microfluidic channel above it, allowing it to be exposed to the IPA dilutions. The tracker IRPHD was electrically controlled and measured using an off-chip source meter. b) Sensogram of the sensor/IRPHD system response to the introduction of IPA dilutions to the sensing ring. A sensitivity of 101.7 V/RIU (or 61.8 nm/RIU) was extracted.	35

Figure 3.6	a) Layout of the broadband MZI design, consisting of a sensor MZI and a tracker MZI, the latter of which is thermally controlled by a resistive heating element. b) Transmission spectra of sensor and tracker MZI (first column) and the resultant output (second column). Initially the transmission spectra are aligned, producing a peak output transmission. When the sensor MZI has a phase shift due to a change in the effective index, Δn , the output is lowered. The tracker phase is realigned to the sensor by applying a power, ΔW . By monitoring the ΔW required to keep the transmission spectra aligned, the Δn caused by the target analyte can be extracted.	37
Figure 3.7	Transmission spectra of MZI ₁ , obtained using a tunable laser. The blue data shows that a 2.0 V signal applied to the tracker MZI ₁ offsets the spectra, allowing the FSRs of each to be extracted. The orange data is the transmission spectrum when 2.5 V is applied to the tracker MZI ₁ . We see that the spectra are roughly overlapped. This is expected as their designs are equivalent.	39
Figure 3.8	a) Experimental setup used for the measurements in b and c. An SLED broadband source was filtered using a BPTF and amplified with an EDFA before being coupled on chip using GCs. The sensor and tracker MZIs were electrically controlled using an off-chip source meter. The optical output was coupled off-chip using GCs and measured with an off-chip PD. b) The detected output optical power as a function of power applied to the tracker MZI ₂ , at various sensor MZI ₂ voltages (indicated as legends on the lineplots). c) The applied tracker MZI power corresponding to peak detected optical power as a function of sensor MZI voltage, for each MZI design. Each data set was fit to a line, with the slope corresponding to the sensitivity of each MZI (in $\text{mW}_{\text{tracker}}/V_{\text{sensor}}$).	40

Figure 3.9	The detected output optical power as a function of power applied to the tracker MZI, at various sensor MZI voltages (indicated in legends) for a) MZI_1 and b) MZI_3	41
Figure 3.10	a) Tracker phase shift required for maximum power output as a function of sensor phase shift, for bandwidths equal to half-integer multiples of the FSR. As more full FSRs are included in the bandwidth, the tracker matches the sensor more linearly at non-integer FSR values. The black dotted line shows the linear value, where exact integer multiples of the FSR are included in the bandwidth (in this case, exactly one FSR). b) Tracker phase shift required for maximum power output as a function of sensor phase shift, for the different MZI configurations in this section. Since the bandwidth was kept constant at 6 nm, the number of bandwidths included is equal to 6 nm divided by the FSR of the device. For MZI_3 , a full FSR was not within the bandwidth, leading to very large deviations.	43
Figure 3.11	System noise in the MZI_1 system, extracted by monitoring the system for 140 seconds. The data was fit with a quadratic function, used to detrend the data. A histogram of the noise distribution is inset, with a standard deviation of ~ 1 mW.	44
Figure 3.12	Tracker power as a function of temperature, measured in the MZI_1 design. After fitting, we see that a 1°C change in temperature change results in a 2.9 mW change in tracker power. If temperature fluctuations are not accounted for in sensing measurements, it may result in incorrect readings.	45
Figure 3.13	Simulated optical spectrum and transmission when the tracker and sensor are slightly out of phase for a) the MRR design and b) the MZI design. In a), we see very low transmission output as the Lorentzian curves do not have any overlap. In b), we continue to detect a signal due to the sinusoidal nature of the transmission, although it is not at its maximum.	49

Figure 3.14	Proposed multiplexing system. Each on-chip CDC filter can be centered at a different wavelength, allowing for different bands of the light to be coupled to each sensing chip. Each sensor ring has its own IRPHD to track transmission shifts. . .	51
Figure 3.15	a) Layout of the fixed-wavelength laser design, consisting of a single MRR in which a portion acts as a sensing region and another portion acts as a heater/detector. b) Simulated resonances in the MRR and IRPHD output, when electrical power W_1 and W_2 are applied to the IRPHD, before and after $\Delta\lambda_{\text{res}}(\Delta n)$, respectively. By monitoring the the electrical power required to keep the transmission spectra aligned to the fixed-wavelength laser, the Δn caused by the target analyte can be extracted. . .	53
Figure 3.16	a) Layout of SWG-assisted structure. b) Sensitivity as a function of waveguide width for SWG and SWG-assisted. Similar sensitivities can be obtained by changing the width of the SWG-assisted blocks.	54
Figure 3.17	a) Layout of transition from strip to SWG waveguides. b) Effective index as a function of width for tapers and SWG waveguide, with a 50% duty cycle, at a 1310 nm wavelength. To keep the effective index of the taper and SWG waveguide matched, the taper must be designed with a width ~ 25 nm larger than the width of the SWG waveguide, as displayed in a).	55
Figure 3.18	Sample diagram of design variations in the fixed-wavelength laser design. On the left, we show the large MRR with 8 sensing sections, using the SWG waveguides. On the right, we have the small MRR with 1 sensing section, using the SWG-Assist waveguides. Various combinations of large versus small, 1 section versus 8 sections, and SWG versus SWG-Assist were fabricated. The cuts shown in the ring indicate that this diagram is not to scale, as the routing waveguides are longer to keep the sensing region farther from the IRPHD.	56

Figure 3.19 Sample resonance peak from the fixed-wavelength laser MRR design measured in water (from the small MRR 8 section SWG-Assist design outlined in Table 3.5). The full-width at half-maximum (FWHM) and extinction ratio (ER) are labelled on the graph. The Q-factor is approximated to be 44,350 using the FWHM = 28.6 pm. 57

Glossary

ASE	Amplified spontaneous emission
BPTF	Band-pass tunable filter
CMOS	Complementary metal-oxide semiconductor
EDFA	Erbium-doped fiber amplifier
ER	Extinction ratio
FOM	Figure of merit
FSR	Free-spectral range
FWHM	Full width at half maximum
GC	Grating coupler
GE	Germanium
ILOD	Intrinsic limit of detection
I/O	Input/output
IPA	Isopropyl alcohol
IRPHD	In-resonator photoconductive heater-detector
LED	Light-emitting diode
LIDAR	Light detection and ranging

LOD	Limit of detection
MRR	Microring resonator
MZI	Mach-Zehnder interferometer
OSA	Optical spectrum analyzer
PD	Photodetector
PDMS	Polydimethylsiloxane
PWB	Photonic wirebond
Q-FACTOR	Quality factor
RIU	Refractive index unit
SIPH	Silicon photonic
SLED	Superluminescent diode
SLOD	System limit of detection
SNR	Signal-to-noise ratio
SOI	Silicon-on-insulator
SPR	Surface plasmon resonance
SWG	Sub-wavelength grating
TE	Transverse electric
TM	Transverse magnetic

Acknowledgments

I would firstly like to thank my supervisors, Prof. Sudip Shekhar and Prof. Lukas Chrostowski, for all the guidance and support they have provided throughout my graduate studies. I appreciate the insightful discussions and the many opportunities they provided for professional and personal growth. I would also like to thank Prof. Nicolas A.F. Jaeger for his support in the lab, expertise in reviewing manuscripts, and patience while teaching me new material. I am very grateful for all his thoughtfulness.

I am extremely thankful for all my colleagues at UBC. In particular, I want to thank Hossam Shoman for the countless hours he spent helping me in the lab, Enxiao Luan for his patience in answering my many biosensing questions, and Mustafa Hammood for always being so quick to help, from guidance in layout designs to debugging lab equipment. I have learned so much from all of them and am truly grateful for the knowledge and skills they taught me. I would also like to thank all my current and former colleagues at UBC, especially Abdelrahman Afifi, Mohammed Al-Qadasi, Steven Gou, Jaspreet Jhoja, Stephen Lin, Ajay Mistry, Connor Mosquera, Avineet Randhawa, Iman Taghavi, Donald Witt and Han Yun.

I would also like to thank my colleagues at other institutions, including Laval University, McGill University, and McMaster University. In particular, I want to thank Piotr Roztocky for his feedback and insights throughout this process.

I am also very grateful for the my internship experience at Lumerical. I would specifically like to thank Ellen Schelew, Zeqin Lu, Ahsan Alam, and all of my colleagues in the Solutions Group for everything they have taught me, and for the many exciting and challenging projects they entrusted with me.

I also would like to acknowledge the Natural Sciences and Engineering Re-

search Council of Canada (NSERC) for financial support, CMC Microsystems and Applied Nanotools Inc. for assistance in fabricating devices, and Luxmux Technology Corporation for providing the broadband source used in my measurements.

Finally, I would like to thank my parents, siblings, family, and friends for the love and support they have continued to show me throughout my graduate studies, and especially over the past year.

Chapter 1

Introduction

1.1 Research background

Miniaturized biosensing devices are crucial for the advancement of global healthcare as they offer fast, reliable, and affordable detection of pathogens, viruses, and bacteria [1, 2]. Services that are typically performed in a lab, such as blood typing or detection of pathogens, can be combined into a single compact device, reducing the required sample size and lowering the cost of materials. Most current diagnostic techniques have been designed for well-equipped laboratory environments, requiring the use of specialized reagents and automated analyzers. This hinders their widespread use, especially in resource-scarce facilities or countries where this equipment or reagents may be unavailable [3]. The importance of global accessible and inexpensive diagnostic testing has been especially highlighted by the COVID-19 pandemic [4]. Although the testing process has significantly improved since the start of the pandemic, it is still far from ideal. For example, in Canada, patients must travel to a designated testing site to have their sample taken, potentially putting others at risk in their route. Samples take several days to be processed, with Ontario alone having a regular backlog of 20,000-60,000 samples [5]. Each test can cost the government upwards of \sim \$40 CAD [6]. With over 26 million tests administered in Canada to date, over \$1 billion CAD has been spent on diagnostic tests alone [7]. Low-cost, high-volume, point-of-care tests are critical not only for COVID-19 detection, but for worldwide healthcare moving forward.

Even prior to the pandemic, 2019 market studies forecast tremendous growth in the biosensor market, growing from \$21.1 billion USD in 2019 to \$31.5 billion USD by 2024 [8, 9]. Over 60% of the projected end use is in point-of-care and at-home diagnostic applications. Of the technologies considered, including electrical, thermal, and piezoelectric platforms, photonic biosensors are expected to experience the most growth. Several photonic sensors based on surface plasmon resonance (SPR) and planar waveguide technologies have been successfully commercialized (by companies such as Biacore Life Sciences and Genaltee [10, 11]), and are continued to be developed (by other researchers and companies such as SiDx and SiPhox, among others [12, 13]).

SPR describes the interaction of light with electrons at a metal/dielectric interface when the light is incident at a critical angle [14]. When the photon frequency matches that of the electrons, the photon energy is absorbed and resonance occurs, causing zero transmission at a specific angle of incidence. This angle is highly dependent on the material properties at the metal/dielectric interface, which can be leveraged for sensors by exposing this interface to organic materials/samples. SPR sensor technology has made tremendous progress over the past 40 years and recently, a point-of-care SPR sensor has been demonstrated [15]. However, this system still requires bulky optical components and large charged-coupled device cameras for detection. While SPR has many advantages compared to traditional chemical diagnostic tests, implementing this technique in a cost-effective, portable manner still faces many challenges.

1.2 Silicon photonics

Silicon photonic (SiPh) sensors based on planar waveguide technology are an exciting alternative to traditional methods. The commercialization of SiPh, while originally driven by applications in telecommunication networks, has shown exceptional progress in many other fields, including quantum information processing [16, 17], light detection and ranging (LIDAR) [18, 19], and sensors [20, 21]. Based on the silicon-on-insulator (SOI) platform, the SiPh platform can confine and route light in very small structures, allowing for extremely compact, yet high density devices. The SOI platform is particularly attractive due to its compatibil-

ity with mature complementary metal-oxide semiconductor (CMOS) fabrication processes. This enables SiPh devices to be produced at a very low cost at high volume [22].

SiPh sensors can perform label-free, real-time measurements, which eliminate long wait times and the need for expensive chemical lab equipment [23]. SiPh devices have demonstrated the ability to detect various pathogens and disease markers, including breast and lung cancer [24, 25], neurodegenerative disorders [26], and SARS-CoV-2 [27]. Because of their CMOS compatibility, these sensors can be produced at very low-cost, enabling the development of scalable, integrated sensing systems.

1.3 Biosensing with integrated photonics

Several figures of merit (FOMs) are commonly used when characterizing the performance of biosensors. These include selectivity, reproducibility, stability, sensitivity, and limit of detection (LoD) [28]. The latter two, sensitivity and LoD, are particularly useful in analyzing SiPh sensors, as they are influenced by the sensor geometry and are independent of chemical factors relating to the analyte (the sample being measured). Sensitivity describes the strength of the sensor response when exposed to an analyte and, as a metric, it is highly dependent on the interaction time between the light and the analyte [29]. There are two types of sensitivity, surface and bulk. Surface sensitivity describes the sensor response due to layers of target analyte on the sensor surface; bulk sensitivity describes the sensor response from a change in mass (or refractive index) of the solution surrounding the sensor due to the presence of the target analyte. Surface sensitivity is highly dependent on the analyte of interest, and is therefore not suitable for a general comparison between sensors. Bulk sensitivity, on the other hand, is not specific to the analyte, and therefore is often used for sensor comparisons.

LoD is defined as the smallest mass (or refractive index) change that is measurable by the sensor, and is given by:

$$\text{LoD} = \frac{3\sigma}{S} \quad (1.1)$$

where σ is the system noise floor, and S is the bulk or surface sensitivity of the

sensor. Since the noise is dependent on instrumental and equipment factors, this LoD is also referred to as the *system* limit of detection (sLoD). For SiPh sensors, LoD can be given in units of refractive index units (RIU), units of pg/mm², or units of ng/mL (or nM) [29]. The latter two are most often used when comparing LoDs for specific analytes. LoD given in RIU is commonly used when comparing between sensors, as it is not specific to the analyte. It can also be used to compare SiPh sensors to other technologies.

Table 1.1 displays results from literature for the detection of selected target analytes using SPR and SiPh sensors, and compares their analysis times and LoDs. Although SPR technologies outperform SiPh sensors in some of the LoD values, the values for SiPh sensors are still comparable and within clinical relevance [30]. They also can be achieved in a much shorter measurement time. SiPh sensors are a promising option, as they produce similar performance to SPR technology and also show the potential to be used in cost-effective, portable sensing systems.

	Target	Analysis time	sLoD
SPR	Avian influenza virus	1.5 hrs	0.128 HAU/mL [31]
	DNA	50 min	1 fM [32]
	Prostate specific antigen	50 min	180 fM [33]
	C-reactive protein	4 hrs	10 ng/mL
	<i>E. coli</i> O157:H7	N/A	3×10^5 CFU/mL [34]
	Gentamicin	N/A	4.7 nM [35]
SiPh	Avian influenza virus	30 min	$5e-4$ HAU/mL [36]
	DNA	10 min	150 fM [37]
	Prostate specific antigen	10 min	0.4 nM [38]
	C-reactive protein	20 min	2.1 ng/mL
	<i>E. coli</i> O157:H7	N/A	10^8 CFU/mL [39]
	Gentamicin	N/A	0.1 nM [40]

Table 1.1: Comparison of SPR and SiPh sensor performance (analysis time and sLoD) for selected target analytes.

1.4 System implementation

An integrated SiPh sensor is just one part of an entire sensing system, which must also include an optical source, a microfluidic system, and a detector/readout sys-

tem. The integration of all these elements remains one of the key challenges for the realization of a SiPh clinical platform [41]. Each component must be optimized for cost, ease-of-use, and compatibility with other system components.

The optical source is one of the main considerations for a SiPh sensor. Most SiPh sensor architectures operate in infrared wavelengths (~ 1550 nm) with a laser as the optical source. While several groups have demonstrated on-chip lasers, based either on optical and electrical pumping methods, these lasers have unfortunately not produced the tunability and resolution required for highly sensitive, low detection-limit sensors [42, 43]. Therefore off-chip, high-resolution tunable lasers remain the most common optical sources for SiPh sensors.

The development of on-chip photodetectors (PDs) is another major area of research. PDs are typically characterized by their responsivity (ratio of photocurrent to optical power) and noise (dark current). For a SiPh sensor, a low dark current is desired, as it results in better detection limits. While several p-n and p-i-n photodetectors have been demonstrated [44, 45], the most widely implemented PDs are based on monolithic germanium (Ge), due to its high optical absorption in the infrared wavelengths [46–49]. These Ge PDs have been reported to have responsivities as high as 0.74 A/W and dark currents of 4 nA [50]. However, fabrication processing of Ge requires temperatures $>300^\circ\text{C}$, which introduces challenges when integrating with standard CMOS electronics processing [46–48, 51]. Doped silicon detectors have been demonstrated as an alternative to Ge PDs, with dark currents of several microns [52]. While their performances are generally lower than Ge PDs, such detectors are fully compatible with the high temperature processing in CMOS electronics fabrication, paving the way towards SiPh sensors with integrated electronics control on a single chip. However, the requirement to detect a small current difference with a single port actuation/sensing complicates the design of the CMOS electronics.

A third component of the sensor system is the delivery of the sample to the SiPh chip. This is typically done through microfluidic integration, where small channels are made above the sensor, through which the sample can flow [53]. Polydimethylsiloxane (PDMS) is a common material used for creating these channels, since it is cheap and easy to fabricate [54]. PDMS can be permanently bound to silicon oxide, enabling a reliable, leakage-free channel. Furthermore, 3D printed

PDMS channels have been demonstrated by several groups, making it a very accessible option [55, 56]. However, PDMS is incompatible with electrode deposition, which makes electronic integration challenging. SU-8, a negative photoresist, is an alternative to PDMS, as it can be used as an electronic passivation layer [57]. However, SU-8 fabrication requires the use of a clean room, increasing the cost of the fabrication process.

Traditional microfluidics require a pumping system to guide the sample through the channels. While simple to implement in a lab, this is a further complication to producing widely available, low-cost sensors, as it requires additional instrumentation. A recent alternative approach is digital microfluidics [58]. Here, droplets of the sample are controlled through a process called electrowetting, where the wettability (i.e., the ability of a liquid to maintain contact with a surface) of the sample is controlled by an applied voltage. Droplets of the sample can be moved without requiring external instruments. Several groups have demonstrated this approach with SiPh sensors [59, 60]. Digital microfluidics promises to offer a low-cost alternative to traditional microfluidic techniques [61–63].

Overall, the optical, electrical, and microfluidic components must combine into a single, stable, compatible package. Several designs for a sensor package have been demonstrated [59, 64]. A promising option is the fan-out wafer-level packaging method [65], which allows for very small device sizes, while still maintaining good electrical contacts and sealed microfluidic delivery. However, this design still relies on off-chip optical and electrical sources with external pumps for microfluidics. Eliminating the need for these expensive, off-chip components is critical for the development of a low-cost sensing system.

1.5 Thesis objective

The objective of this thesis is to demonstrate that high-resolution tunable lasers are not required to achieve high-performance SiPh sensor systems. Tremendous research effort has produced highly sensitive SiPh sensors, however, implementing these sensors into systems remains extremely expensive due to their dependence on high-resolution tunable lasers. Novel SiPh sensor architectures must be introduced in order to move to lower-cost optical sources. This thesis presents three low-cost,

CMOS compatible architectures that do not rely on tunable lasers, thus lowering the overall system cost and providing a potential path forward for the realization of SiPh sensing systems.

1.6 Thesis structure

This introductory chapter provided the background and motivation for the development of low-cost SiPh sensor systems. The remainder of this thesis is organized into three chapters:

Chapter 2 provides a review of fundamental concepts and components required in a SiPh sensing system. On-chip photonic structures are summarized with key equations and figures of merit. Various optical sources used in SiPh sensors are presented and discussed in terms of cost, sensor complexity, and coupling considerations.

Chapter 3 presents three low-cost SiPh sensor designs. The first two utilize a broadband source in place of a tunable laser, and the last design uses a fixed-wavelength laser. Design, simulation, and measurement results are presented, including discussion on the sensors' sensitivities and detection limits.

Chapter 4 summarizes key results from Chapter 3 and discusses limitations to the designs presented. Future work and next steps are outlined in this chapter.

Chapter 2

Review of system components

This chapter provides an overview of different components required for the SiPh sensor, including SiPh sensor structures and optical sources. While numerous SiPh structures and components have been investigated in literature, this section will focus on the basic structures that are utilized in the SiPh sensors discussed in Chapter 3. Three different optical sources categories are presented with their corresponding sensor designs, and are discussed in terms of cost and complexity. While implementing low-cost alternatives to the optical source is imperative to an affordable sensor system, understanding their tradeoffs in terms of complexity and sensor performance is vital.

Microfluidics and photodetectors are two other components that can add additional costs to the system; however, investigation of these topics is out of scope for this work. More information on these topics can be found in [66] and [67].

2.1 Integrated photonic sensor components

Many components work together to create integrated photonic circuits. This subsection provides a brief overview to the simplest of these, the waveguide, and discusses its place in a sensing system. Several sensing architectures are presented, including the Mach-Zehnder interferometer and the microring resonator, along with the key equations used to model their behaviour.

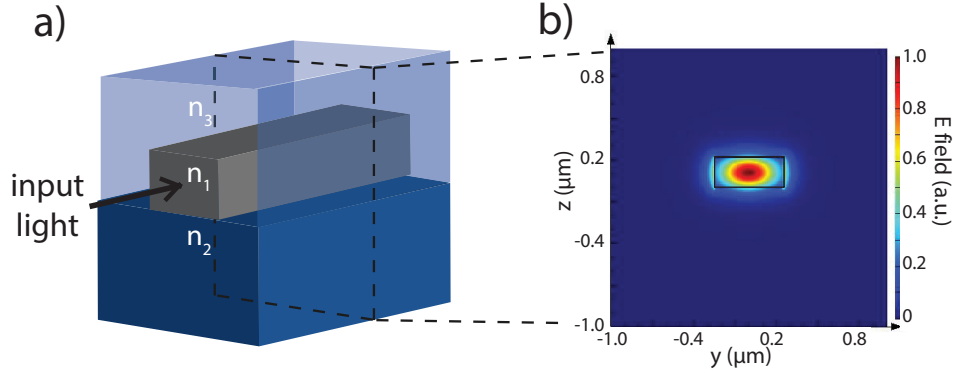


Figure 2.1: a) A standard waveguide, where n_1 refractive index of the waveguide core, and n_2 and n_3 are the refractive indices of the waveguide cladding. In SiPh sensors, the n_3 layer is the solution containing the target analyte. b) The fundamental waveguide mode, as simulated by Lumerical's MODE. The effective index can be extracted.

2.1.1 Waveguides

The fundamental building block of silicon photonics is the waveguide. Waveguides operate on the basis of total internal reflection, where a high refractive index material (the core) is surrounded by a material with a lower refractive index (the cladding) (Fig 2.1a) [68]. Light coupled into the waveguide can be guided into various circuits across the SiPh chip by routing waveguides.

While most of the energy of the light is confined to the silicon core, a small portion of the energy (decaying exponentially with distance away from the core), known as the evanescent field, travels into the cladding (Fig 2.1b). Because of this, the propagation of light is dependent on the properties of both the core and the cladding. The net refractive index experienced by the propagating light is referred to as the effective index (n_{eff}). The effective index of a waveguide can be simulated using software such as Ansys's Lumerical MODE, which was used to generate Fig 2.1b.

The group index (n_g) of the waveguide describes the group velocity of the light, and is dependent on the effective index (n_{eff}), given by:

$$n_g(\lambda) = n_{\text{eff}}(\lambda) - \lambda \frac{dn_{\text{eff}}}{d\lambda} \quad (2.1)$$

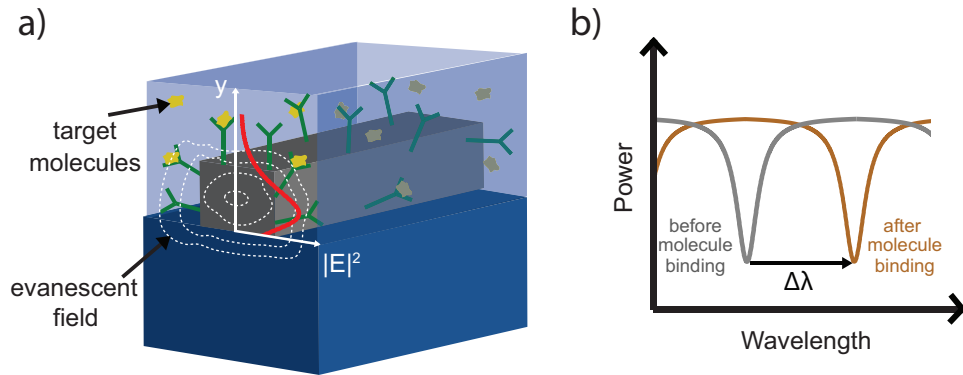


Figure 2.2: a) The evanescent field extends past the silicon waveguide and into the cladding. By functionalizing the surface of the waveguide (green structures), specific analytes (yellow) can bind to the surface and change the effective index. This change will alter the propagation behaviour of light, as in b), where the transmission is shifted $\Delta\lambda$ after molecule binding.

where λ is the wavelength of light. The group index is particularly important for silicon photonic sensors, as it influences the transmission properties of structures [68]. This is discussed in more detail in Section 2.1.2 and 2.1.3.

Evanescent field sensing

As mentioned in the previous section, a small portion of the propagating electrical field extends outside the silicon core, making the optical response sensitive to the refractive index of the cladding [23]. This property is leveraged in the design of silicon photonic sensors. When target molecules are introduced to the solution surrounding the waveguide, it causes a change in the refractive index of the cladding, due to the presence of these new molecules. This index change shifts the effective index of the waveguide, modifying the propagation behaviour of the guided light (Fig 2.2, Eq 2.1). By functionalizing the surface of waveguides to capture specific analytes, the propagation behaviour of light can be monitored and used to measure specific analytes.

Evanescent field sensing can be used as a label-free detection method, which reduces complexity, cost, and time relative to methods based on labelling [29].

Label-free methods rely on detecting the target's molecular properties, such as molecular weight or refractive index, whereas labelled methods attach additional molecules, such as dye molecules or fluorescent tags, to the target to increase the detected signal. While highly selective and achieving low LoD, labelled detection requires multiple chemical processing steps, which increases cost and complexity, and makes it difficult to extract kinetic information. Label free methods also have some shortcomings, as they can only operate if non-specific binding is low (i.e., low binding of molecules other than the target). However despite this, they have been widely researched due to their reduction in processing time and steps. Because label-free methods directly detect the target, they can also be used to extract kinetic information for characterizing molecular interactions.

Extracting kinetic information using evanescent sensors was first demonstrated using SPR technology [14], but has since been demonstrated using numerous SiPh sensors [69–71]. By monitoring the slope of the response curve as the sensor is exposed to the target molecule, bio-specific binding and release can be monitored [29, 72].

Sub-wavelength gratings

One strategy to improve the sensitivity of silicon photonic sensors is to use sub-wavelength gratings (SWGs). First proposed by the National Research Council of Canada in 2006 [73], these structures consist of periodic blocks of high and low index material (Fig 2.3a), with a period, Λ , much smaller than than the Bragg condition (i.e., $\Lambda \ll \frac{\lambda}{2n_{\text{eff}}}$). The effective index of this structure is smaller than that of a straight silicon waveguide, resulting in an increased mode cross-section, and more energy in the evanescent field (Fig 2.3b). This increases the amount of light-matter interaction a propagating field has with the analyte of interest, which can result in higher sensitivities. Several groups have continued research into these devices, reporting sensitivities up to 580 nm/RIU, and detection limits down to 2×10^{-6} RIU [23, 74–76].

Although a lower effective index can result in higher sensitivity, the index cannot be lowered indefinitely. When the effective index drops below 1.65, the propagating waveguide mode is no longer supported [77]. To stay above this threshold,

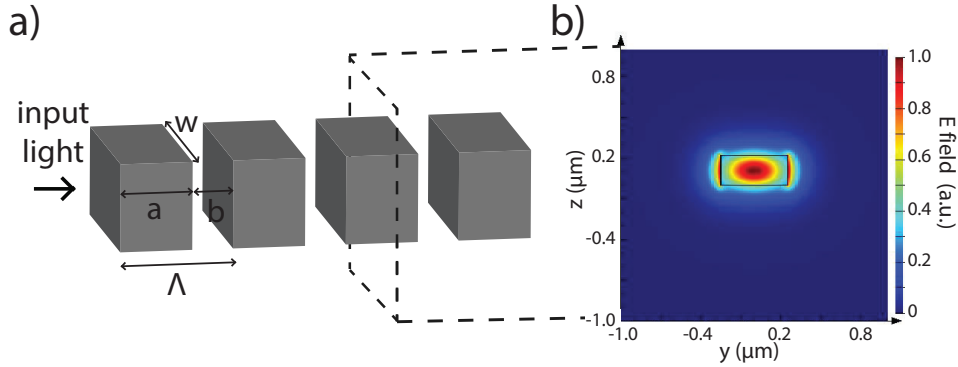


Figure 2.3: a) A sub-wavelength gratings (SWG) waveguide structure. The width (w), period (Λ), and depths of both the high and low index blocks (a and b , respectively) are labelled. b) The mode profile of an SWG waveguide. More energy is outside of the silicon core compared to the optical propagation in a straight waveguide (Fig 2.1).

the duty cycle (a/Λ) is usually set to $\sim 50\%$, depending on the waveguide width (w in Fig 2.3a). Additionally, fabrication of SWGs introduces new challenges. Firstly, the length of both the high and low index blocks (a and b , respectively, in Fig 2.3a) are limited by fabrication minimum feature sizes, which are often in the ~ 150 nm range. Furthermore, these small pieces of silicon can become loose, fall over, or get washed away entirely if the oxide beneath the waveguide is over-etched. This makes their fabrication extremely delicate.

2.1.2 Mach-Zehnder interferometers

One of the lowest complexity structures for SiPh sensing is the interferometer, with the Mach-Zehnder interferometer (MZI) being one of the most common configurations [23]. In an MZI, light is split into two waveguide paths (often using a Y-branch component), with one path exposed to the sample (L_{sens}), and the other used as reference (L_{ref}) (Fig 2.4a). When the light is recombined (using a second Y-branch), the output intensity follows an interference pattern dependent on the phase difference between the two paths (Fig 2.4b). As interaction with the sample introduces a phase shift ($\Delta\phi$) in the sensing arm, the output intensity (I_o) will be a periodic function dependent on that phase shift, given by:

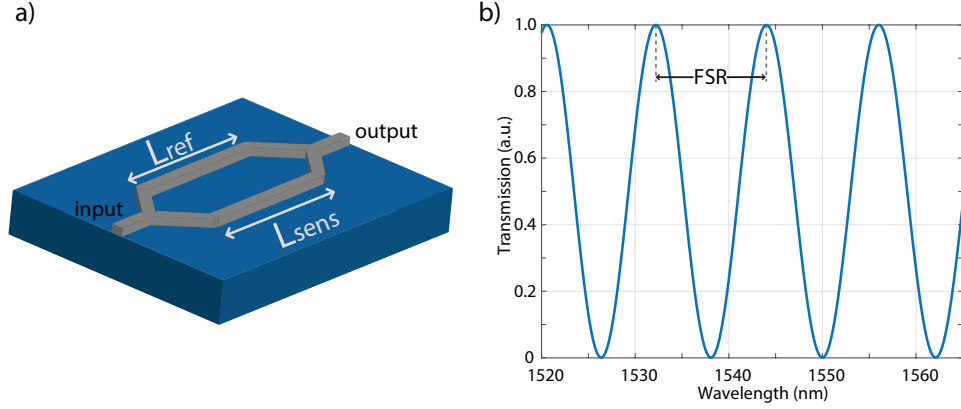


Figure 2.4: a) Basic design of a Mach-Zehnder interferometer. b) Typical transmission spectrum from the output, when a path length imbalance (ΔL) exists between the arm.

$$I_o = I_{\text{sens}} + I_{\text{ref}} + 2\sqrt{I_{\text{sens}}I_{\text{ref}}}\cos(\Delta\phi + \Delta\phi_0) \quad (2.2)$$

where I_{sens} and I_{ref} are the intensities of light in the sensing and reference arms, respectively, and $\Delta\phi_0$ is the initial phase difference between the arms. The phase shift caused by the analyte can be related to the change in effective index (Δn_{eff}) at a given wavelength (λ) by:

$$\Delta\phi = \frac{2\pi}{\lambda}\Delta n_{\text{eff}}L_{\text{sens}} \quad (2.3)$$

where L_{sens} is the length of the sensing arm. Because the sensitivity of the sensor is defined by the change in phase due to the change in the RIU of the cladding, Eq. 2.3 suggests that a longer sensing arm can result in higher sensitivities [78]. However, as the length of the interferometer is scaled, the device also becomes more sensitive to input source fluctuations and temperature variations across the chip, which can result in false positives [79]. Additional modulation approaches to tune the phase are typically required for interferometric sensors [23].

The free-spectral range (FSR) is the spacing between two successive intensity minima or maxima in a periodic transmission spectrum. For an MZI, the FSR at a specific wavelength (λ) is given by:

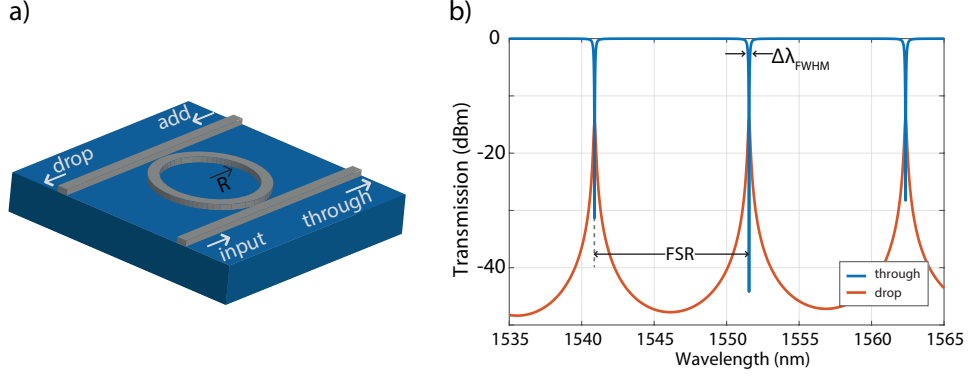


Figure 2.5: a) Basic design of a add-drop microring resonator. b) Typical transmission spectrum as measured from the through port (blue) and drop port (orange) of the ring. The FSR and $\Delta\lambda_{\text{FWHM}}$ are labelled.

$$\text{FSR} = \frac{\lambda^2}{L_1 n_{g1} - L_2 n_{g2}} \quad (2.4)$$

where L_1 , L_2 and n_{g1} , n_{g2} are the lengths and group indices of the two arms, respectively. Often, the denominator in Eq. 2.4 is simplified to $n_g \Delta L$. This does not hold for a sensor, however, since the cladding in each arm is different and therefore the group indices will be independent.

2.1.3 Microring resonators

A microring resonator (MRR) consists of a looped optical waveguide and a coupling element to access the loop (which is typically accomplished via evanescent field coupling) (Fig 2.5a) [80]. The MRR is in resonance when light in the loop interferes constructively (by building up an effective 2π round trip phase shift) (Fig 2.5b). The resonance wavelength (λ_{res}) of the MRR is given by:

$$\lambda_{\text{res}} = \frac{2\pi R \times n_{\text{eff}}}{m} \quad (2.5)$$

where R is the radius of the resonator, n_{eff} is its effective refractive index, and m is a positive integer. When the MRR is exposed to a sample, the effective index (Δn_{eff}) will shift. This will shift the position of the resonant wavelength ($\Delta\lambda_{\text{res}}$) by:

$$\Delta\lambda_{\text{res}} = \frac{\lambda}{n_g} \Delta n_{\text{eff}} \quad (2.6)$$

Unlike the MZI (described by Equation 2.3), this equation shows that the sensitivity of the MRR is independent of the size of the resonator. Instead, it is characterized by the quality factor (Q-factor), which describes how long the photon energy stays within the resonator [29]. The Q-factor is given by:

$$Q = \frac{2\pi \cdot n_g \cdot 4.34}{\lambda_{\text{res}} \cdot \alpha_{(\text{dB/m})}} \approx \frac{\lambda_{\text{res}}}{\Delta\lambda_{\text{FWHM}}} \quad (2.7)$$

where n_g is the group index, $\alpha_{(\text{dB/m})}$ is the total loss in the resonator, and $\Delta\lambda_{\text{FWHM}}$ is the full width half maximum bandwidth (FWHM) of the resonance peak. A higher Q-factor means that light will remain inside the cavity for longer, and will therefore have a higher interaction time with the analyte. Because of this, the Q-factor will effect the *intrinsic* LoD of the microring sensor, given by [81]:

$$iLoD = \frac{\lambda}{Q \times S} \quad (2.8)$$

where λ and S are the wavelength and sensitivity of the sensor, respectively. The iLoD is only dependent on intrinsic sensor characteristics (such as Q-factor), and is therefore useful to compare systems with different experimental setups. Because the Q-factor is dependent on the losses in the structure, it is often difficult to produce high Q-factor devices, as sidewall scattering, bend radiation, and material absorption (including the analyte) contribute significantly to loss [68].

The FSR for an MRR is given by:

$$\text{FSR} = \frac{\lambda^2}{2\pi R n_g} \quad (2.9)$$

where λ , R , n_g are the wavelength, radius, and group index of the ring, respectively. This equation is very similar to that of the MZI (Equation 2.4), however, since the entire ring is exposed to the sample, only a single group index is required. MRRs with the same radius but different claddings will have different FSRs. Furthermore, since group index is wavelength dependent (Equation 2.1), the FSR will also vary with wavelength. However, this effect can be ignored over small wavelength bands.

2.1.4 Other sensor structures

There are several other structures in development for SiPh sensors, most notably ones based on Bragg gratings and photonic crystals [23]. Both are similar to the SWG waveguide architecture, with periodic structures of high and low refractive indices. For a Bragg grating based sensor, the period of the structure is significantly larger than that of an SWG waveguide (i.e., $\Lambda_{\text{Bragg}} = \frac{\lambda}{2n_{\text{eff}}}$), which results in light being reflected at each interface. The repeated reflections at a specific wavelength result in a sharp peak at that wavelength, which can be tracked, similar to resonance peaks in MRRs.

Conversely, photonic crystal based sensors have periodicity on the order of the wavelength of light. This prevents a band of light from passing through the structure. However, by introducing a defect into the crystal, strong optical confinement creates a resonance at a specific wavelength, which once again can be monitored in sensing experiments.

2.1.5 Summary

While interferometric sensors have higher, length-scalable sensitivities, their large size, temperature dependence, and additional modulation requirements can make them more challenging to implement on chip [79]. However, they represent the simplest sensor geometry in terms of fabrication and design. MRRs are a promising option due to their compact size, which also enables high-density integration on chip. However, achieving consistently high Q-factors can be challenging, especially with additional loss from water absorption. Bragg gratings and photonic crystals are similarly compact, however their periodic structures create additional fabrication challenges. Overall, microring resonators are the most commonly implemented structure, with a good trade-off between design simplicity, stability, size and sensitivity.

2.2 Optical sources

In this section, the various light sources used in SiPh sensor systems are outlined, alongside their corresponding sensor designs. Cost, sensor complexity, and coupling considerations are discussed, and a comparison between the optical sources is made.

2.2.1 Tunable lasers

Measuring the wavelength (or phase) shift in a sensor's transmission spectrum is the most common method for analyte detection in silicon photonics. In such a configuration, the light from a high-resolution tunable laser is coupled into a SiPh sensor chip and measured by a PD, either on or off chip (Fig 2.6a). The laser wavelength is continually swept over a set bandwidth, allowing for the reconstruction of the sensor's transmission spectrum in this band. As the transmission spectrum of the sensor shifts in response to a sample (mediated by changes in the effective index, see Section 2.1.1), monitoring these shifts over time allows the extraction of the change in RIU.

This tunable laser configuration has many advantages. Because the linewidth of the laser is very narrow, the detection of resonant wavelength shifts can be very precise [57]. Additionally, reconstruction of the entire spectrum allows for the implementation of post-processing techniques like curve fitting, which can help resolve wavelength shifts smaller than the laser resolution, further lowering the sLoD. Finally, the tunable laser configuration allows for very simple on-chip sensor systems. Only a single sensor structure (such as an MRR or MZI) and detector are required on chip. This keeps the prerequisite on-chip optical design and electronics control simple, and enables a high density of sensors to be fabricated on a single chip, which can be used for detection of multiple analytes (multiplexing).

While tunable lasers aid in the reduction of on-chip sensor complexity, their use significantly complicates the overall sensing system. Because high-resolution tunable lasers remain an off-chip component to the sensor, tremendous cost and complexity is added to the overall system.

The cost for a high-resolution tunable laser remains very high, typically in the \$10k-100k USD range [82]. While development of fixed-wavelength lasers, driven

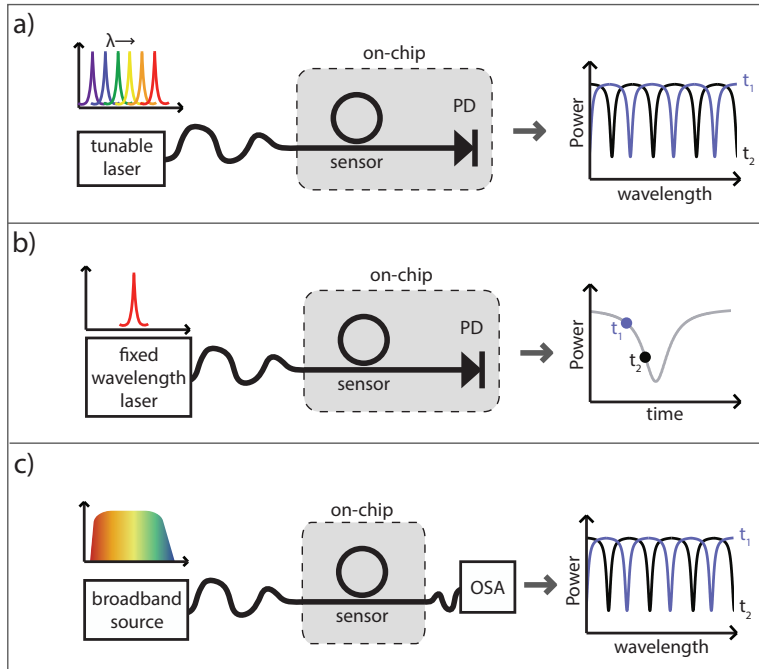


Figure 2.6: Overview of typical sensing setups making use of a) a tunable laser, b) a fixed-wavelength laser, or c) a broadband source. a) The laser wavelength is swept and the output is coupled to the SiPh chip, where it passes through a sensor and is then detected with an on-chip PD. A typical output spectrum is shown on the right, where optical power is a function of wavelength, and the transmission spectrum shifts when the sensor is exposed to an analyte (t_1 and t_2 are before and after analyte exposure, respectively). b) A fixed-wavelength laser is coupled on-chip, where it passes through a sensor and is then detected with an on-chip PD. The typical output spectrum is shown on the right, where optical power is a function of time, since only a single wavelength is being detected. As the sensor is exposed to a sample, the detected optical power will shift due to a change in alignment between the fixed-wavelength input and the sensor's transmission spectrum from t_1 to t_2 , before and after exposure to a sample, respectively. c) The broadband source (containing all wavelengths over a given bandwidth) is coupled to the SiPh chip, where it passes through a sensor, and is then coupled off chip to an OSA. The typical output spectrum is shown on the right, where optical power is a function of wavelength, and the transmission spectrum shifts from t_1 to t_2 , before and after exposure to a sample, respectively.

by applications in telecommunications, has lowered their cost [83], off-chip tunable lasers remain among the most expensive components of a SiPh sensor system. One of the promises of SiPh devices as sensors is that they can be manufactured for very low cost at high volume by leveraging advanced CMOS fabrication technologies [22]. By requiring an expensive tunable laser in the sensing system, these low-cost advantages are reduced, as the total system cost remains high. Furthermore, the sLoD of the sensor is dependent on the resolution of the laser, which can scale with its cost. Therefore, to achieve a lower sLoD, a more expensive laser is required. This creates an intrinsic trade-off between sensor performance and cost for a tunable laser configuration.

Secondly, because the laser is off chip, it adds to the system's complexity and cost by requiring repeatable and precise techniques for coupling light into the sensor chip. One such technique, implemented by Genalyte Inc., uses a mechanical mirror system to focus the laser light onto grating couplers for each sensor [84]. While very precise and effective, these additional components add cost, size, and complexity to the system. Another method includes gluing a fiber array directly onto the chip [85]. While this technique has not been demonstrated specifically for SiPh sensors, it would likely be feasible. Fiber arrays are relatively inexpensive, typically only a few dollars when ordered in high volume; however, this method caps the number of input/output (I/O) channels for the chip to the number of channels in the array. For multiplexing devices where 10+ sensors are on chip, light will need to be split on chip, resulting in less optical power per sensor. This can reduce the measurement signal to noise ratios (SNRs), degrading performance. Furthermore, gluing the fiber array on-chip requires precise alignment [85], which can add more time and cost to the packaging process.

Tunable lasers have remained the standard for SiPh biosensors primarily because of their use in the development stage of these sensors. However, as sensor architectures have matured, the need for tunable lasers has impeded the realization of affordable SiPh sensing platforms.

2.2.2 Fixed-wavelength lasers

Biosensor platforms implementing fixed-wavelength lasers are a promising approach for SiPh sensors due to their low cost and potential for on-chip integration. Unlike systems with tunable lasers, systems with a fixed-wavelength laser cannot directly measure the wavelength resonance shift, and so alternative approaches must be used. The most common method is to monitor the optical power through the sensor over time [78, 86–88]. In this configuration, a fixed-wavelength optical signal is input to the sensor and the output optical power is measured with a PD (Fig 2.6b). When the resonance wavelength of the sensing system shifts, the fixed input wavelength will no longer be aligned to the resonance, and instead will experience a different transmission ratio along the sensor response curve. This results in a change in the output optical power measured by the PD, which can be used to determine the change in RIU.

While very simple, this method is unfortunately extremely sensitive to changes in the input optical power. Water and material absorption can reduce measured optical power, which can be read by the system as a false positive. Additionally, source noise, thermal drifts, and changes in on-chip coupling over time, can cause fluctuations in input power [87, 88]. This necessitates precise control over the input power, which is not trivial for integrated lasers.

Other fixed laser approaches have also been suggested. One alternative is to use a coherent detection approach, where the two arms of an MZI are recombined via a 2×3 coupler, allowing the phase shift to be extracted independent of optical intensity [89]. Another design uses a near-infrared camera to measure the light-scattering from a coupled-resonator optical-waveguide, and determine shifts in refractive index from the imaged intensity patterns [90]. Other approaches include multiple fixed-wavelength lasers for a single sensor [91, 92]. By setting the wavelength of each laser slightly apart, the full transmission spectrum can be reconstructed and monitored by curve fitting. While simple for a single-sensor design, using multiple lasers per sensor cannot scale when moving to designs with multiple sensors on the same chip. Other designs, including phase generated carrier demodulation [93] and microwave filtering [94, 95], require more complex modulation and electronics control, and require additional post-processing steps.

One of the distinct advantages of a fixed-wavelength laser is the relative ease of its coupling integration. Unlike a tunable laser, fixed-wavelength lasers can be fabricated on small dies that can be directly coupled to the SiPh sensor chip. One of the most common coupling techniques, demonstrated in the telecommunications industry, is edge coupling [96, 97]. By carefully aligning the edge of the laser to the input of an on-chip edge coupler, the light can be guided into the chip. A recent alternative approach has been to couple light from a DFB laser to a chip via a photonic wirebond (PWB) [82, 98]. Both of these methods enable the light source to be packaged with the sensor, which reduces off-chip costs and can allow for a simpler, smaller at-home sensor solution. However, the edge-coupling method requires very precise, manual alignment for each laser. This will need to be addressed when moving to high-volume manufacturing, as the time and labour required for this manual alignment could drastically increase cost of production.

Overall, fixed lasers are a promising alternative to tunable lasers due to their lower costs and simpler coupling options. However, their use introduces a high sensitivity to noise and the need for post-processing, which complicates their implementation in scalable and robust systems.

2.2.3 Broadband sources

Broadband light sources, such as light-emitting diodes (LEDs), super-luminescent diodes (SLEDs), and amplified spontaneous emission (ASE) sources, are typically much (10-100x [82]) cheaper than tunable lasers, and therefore are another promising alternative for reducing the costs of a sensing platform. Since the light is emitting over a broad range of wavelengths, a single photodetector cannot distinguish shifts in the resonance wavelength. Instead, an optical spectrum analyzer (OSA) is typically required for the detection step in such systems (Fig 2.6c). OSAs have varying operation principles, usually relying on diffraction gratings or interferometers [99]. Depending on the configuration, the OSA resolutions are typically on the order of 0.1 nm, with very high-precision models accessing resolutions on the order of 0.01 nm.

In the broadband-OSA sensor design, the resolution of the OSA will ultimately determine the sLoD. Like tunable lasers, OSAs are very expensive [100], and their

cost similarly scales upwards with increasing resolution. Additionally, OSAs are an off-chip component, requiring additional off-chip coupling for the sensor and adding more cost, size, and complexity to the system.

Other designs have been proposed to eliminate the need for an OSA. One method relies on intensity tracking, similar to the fixed-wavelength designs [101, 102]. In this case, the intensity change arises due to absorption from the target analyte solution. This design suffers from the same drawbacks as fixed-wavelength laser designs, as the detection is very sensitive to input optical power, and fluctuations and noise can produce false positives.

Song et al. [103] suggested another broadband system, which uses a tracking microring to electrically track resonance shifts from a separate sensing microring (Fig 2.7). Broadband light is input to the first microring, the sensing microring. The drop-port of this ring is coupled to the next microring, the tracking microring, which is electrically controlled by a heater. To align the resonances of the rings, an initial electrical power is applied to the tracker microring, allowing a output signal to be measured. When the resonance of the sensing ring is perturbed due to interaction with an analyte, the transmission spectra of the rings will be misaligned, and a low output signal will be measured. To realign the resonances, a new electrical power is applied to the tracker ring. By monitoring the shift in applied electrical power required to keep the two resonances aligned, the wavelength resonance shift caused by the analyte exposure can be determined. In this design, the sLoD is ultimately limited by the resolution of the control electronics. Because of the advancements in CMOS electronics, this resolution can be increased at a much lower cost compared to the cost required to increase the resolution of a laser.

Like tunable lasers, stable, high-power LEDs remain an off-chip component, and therefore also suffer from the same coupling complexities as lasers. However, like the fixed laser, the option to use a PWB to couple directly from the broadband source die to the SiPh chip could likely be implemented (this has not been explored to date).

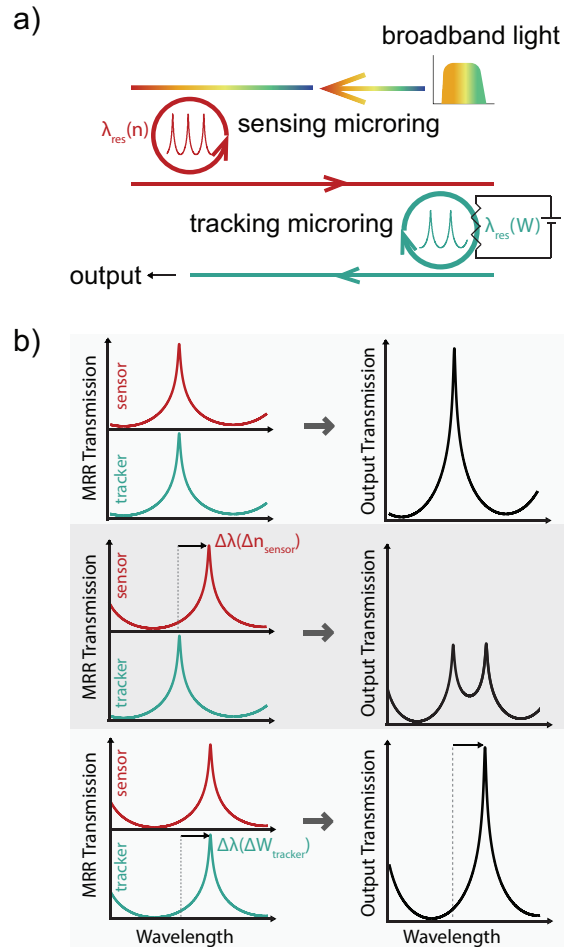


Figure 2.7: a) Broadband sensor-tracker design layout, proposed by Song et al. [103]. b) Transmission spectra of sensor and tracker microrings (first column) and the resultant output (second column). Initially the ring resonances are aligned, producing a peak output transmission. When the sensor resonance shifts due to a change in the effective index, Δn , the total optical power output is lowered. The tracker resonance is realigned to the sensor by applying a power, ΔW . By monitoring the ΔW required to keep the resonances aligned, the Δn caused by the target analyte can be extracted. (Here the output is shown as a function of wavelength, however, this design measures the photocurrent collected by the PD, which is essentially the integral of these output curves. Spectral information is not required in this design.)

2.2.4 Summary

Table 2.1 summarizes considerations when choosing an optical source. Despite their high cost, tunable lasers have been the standard for SiPh sensors due to their simple sensor design and ease of use. However, to enable a cost-effective SiPh sensing platform, other optical sources must be implemented. Fixed-wavelength lasers are a lower-cost alternative with several options for coupling to chip; however, the corresponding sensor design and signal readout can be quite complex. Broadband sources are another alternative that are less expensive than tunable lasers, but more costly than fixed-wavelength lasers. They currently suffer from similar coupling restrictions as tunable lasers.

	Tunable laser	Fixed-wavelength laser	Broadband
Cost	~\$10k-100k	~\$1-10	~\$100-1k
Coupling	off-chip	edge coupling, PWB	off-chip, edge coupling, PWB
sLoD factors	Wavelength resolution	Optical intensity noise, electronics resolution	OSA resolution, electronics resolution

Table 2.1: Summary of key considerations when choosing an optical source for a SiPh sensing platform. PWBs have not been demonstrated with broadband sources, and have yet to be demonstrated at high-volume for fixed-wavelength lasers. The optical intensity noise will effect the sLoD in intensity-based approaches for fixed-wavelength laser systems; however, optical intensity variations should not effect other approaches.

Chapter 3

Research contributions

To lower the overall cost of the SiPh sensing system, designs that do not require a high-resolution tunable laser must be implemented. Alternative optical sources were discussed in the previous chapter. Here, two broadband designs and one fixed laser architecture are presented. Design and experimental characterization is presented for the broadband designs; design and simulation results are discussed for the fixed laser system.

3.1 Broadband designs

3.1.1 Broadband MRR design

In this section, we propose and demonstrate a low-cost SiPh sensor that uses doped silicon detectors and a broadband source, thus eliminating the need for a laser and Ge PDs. The sensor design is similar to the one proposed by Song et al. [103], discussed in Section 2.2.3. The approach demonstrated here replaces the electrically controlled ring with an in-resonance photoconductive heater-detector (IRPHD) [52] to electrically track the MRR sensor, while also acting as the PD to detect the signal. Compared to Ge PDs, the IRPHDs: (1) reduce the overall cost of photonic biosensors; (2) reduce the number of pads by half for electrical I/O, thus reducing the on-chip real estate; (3) have higher quantum efficiencies; (4) can be used to monitor the optical power inside the ring and can thus generate high

photocurrents across a large optical dynamic range; (5) are compatible with high-temperature CMOS fabrication processes. We demonstrate this method first by using thermally-tuned MRRs in simulated biosensing experiments to compare the IRPHD performance to a Ge PD, and second, in a real-time sensing measurement of isopropyl alcohol, reporting a sensitivity of 101.7 V/RIU and a system limit of detection of 9.8×10^{-4} RIU.

Operating Principle

The layout of our broadband SiPh sensor design is shown in Fig 3.1a, with similarities in design to Fig 2.7a. Here, the IRPHD acts as the tracker MRR, which both tunes the resonance and measures the power within the ring. When the two resonance peaks are aligned, the detected photocurrent in the IRPHD is maximized. In practice, two different methods can be used to track the point where the photocurrent is maximized. With the first method, the voltage applied to the IRPHD is scanned repeatedly, and the photocurrent versus voltage curve (such as the one shown in Fig. 3.3) can be fit to find the peak photocurrent position. This peak position can be extracted from each scan and tracked over time. An alternative method makes use of the maximum search algorithm [104]. With this second method, an initial scan is used to find the starting peak position, and the IRPHD is biased at that point. The photocurrent is then sampled at a slightly higher and slightly lower bias point, and compared to the photocurrent at the current bias. If the photocurrent is higher at a sampled point, that point will be set as the new bias point for the IRPHD. This sampling is then continuously repeated to track the peak position over time. While both of these methods should produce the same result, the scanning method is much more reliable in practice. If the signal is noisy, or if the sensor resonance shifts too quickly, the maximum search algorithm may become stuck at a local maximum of the optimization, rather than tracking the global peak. For example, if the sensor resonance shifts quickly, the detected photocurrent will drop drastically into noise, and the photocurrent sampled at higher and lower bias points will also return noise values. This may cause the photocurrent to be stuck at its current position, and would likely require a new scan to properly realign to the peak. The scanning method thus provides a more consistent method to deter-

mine the absolute peak. Furthermore, the scanning method enables post-processing curve fitting, which can benefit from noise averaging, and fitting the peak location to a finer resolution than the sampling resolution, which can thus lower the sLoD. This scanning method is implemented in the following experiments, unless stated otherwise.

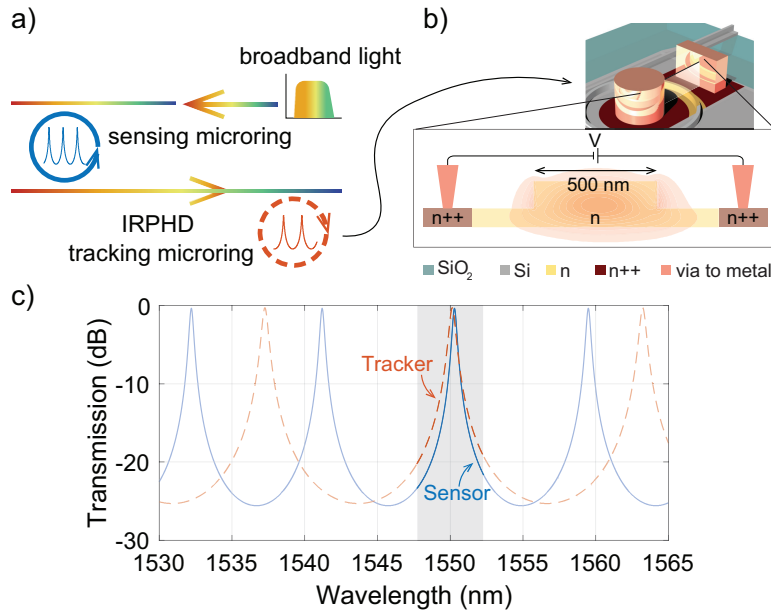


Figure 3.1: (a) Layout of the photonic sensor, consisting of two MRRs, a sensor and a tracker, using a broadband source. (b) Cross-section of IRPHD tracking MRR. (c) Simulated transmission of the drop-ports of both MRRs. The grey area corresponds to the 6-nm bandwidth that is measured.

Fig 3.1b shows the cross-section of the IRPHD. The rib waveguide of the IRPHD is formed using a 500 nm core width with a 90 nm thick slab. The waveguide core was N doped and the sides were N++ doped to form Ohmic contacts. While the n-type doping in the waveguide core is low enough to allow for low-loss (doping loss = 5 dB/cm) propagation, it is sufficient enough to [52]: (1) lower the electrical resistance across the waveguide, enabling the device to function as a thermo-optic tuner over appreciable wavelength ranges driven by low voltages compatible with CMOS circuitry, and (2) increase the measurable photocurrent to

micro-amperes (for micro-watt input optical powers), allowing the device to also function as a precise power monitor inside an optical circuit. To operate as a photodetector in this sensing circuit, IV curves of the IRPHD are taken with and without light in the circuit. By subtracting the curves, we can get a direct measurement of the photocurrent. Since the IRPHD photocurrent is maximized when the sensing and tracking rings' resonances are aligned, the voltage supplied to the IRPHD tracking ring is proportional to the analyte perturbing the microring.

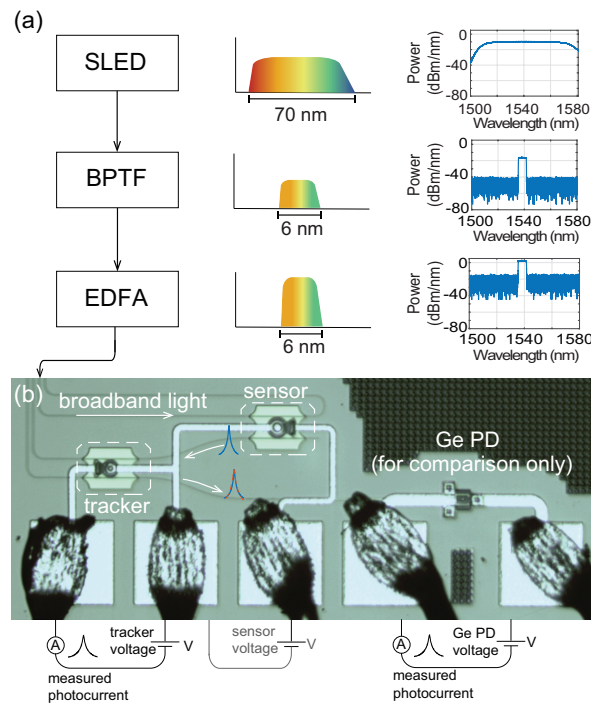


Figure 3.2: (a) Block diagram of our experimental setup, with measured spectrum shown to the right. A SLED broadband source was filtered using a bandpass tunable filter (BPTF) and amplified by an erbium-doped fiber amplifier (EDFA) before being coupled on chip. (b) Optical microscope image of a test device. Here we include a thermally-tunable ring to simulate a biosensing experiment, and a germanium photodetector (Ge PD) to compare to our doped detectors (IRPHDs).

Device design and fabrication

Fig 3.2a displays a block diagram of the experimental setup. A LUXMUX BeST-SLED [105] was used as our optical broadband source. Since the free-spectral range (FSR) of the sensing and tracking MRRs are not identical, other resonance peak overlaps are possible. To ensure only a single resonance mode overlap, we used a 6 nm bandpass tunable filter (BPTF), followed by an erbium-doped fiber amplifier (EDFA) to compensate for the BPTF and on-chip grating coupler losses. Although some work can be done to match the FSRs of the MRRs, the peaks will remain aligned only for a small bandwidth. The group index of the sensor and tracker MRR will vary because of the different cladding materials (water vs oxide), causing two independent FSRs as a function of wavelength (Equations 2.1 and 2.9). A filter will always need to be implemented as long as the broadband source bandwidth is larger than the FSRs. In the future, an on-chip BPF could be utilized [106]. Our devices were fabricated using 248 nm optical lithography at A*STAR IME. Fig 3.2b shows an optical microscope image of a test device, which included a Ge PD that was used for a comparison to the IRPHD.

Power budget

Table 3.1 below summarizes the total remaining power in this design (along with designs discussed further in this chapter) after accounting for losses in each component. Coupling losses are not included in this calculation, as these losses should be equivalent for each system (~ 0.7 dB if using PWBs [82], or > 3.8 dB if using grating couplers [107])¹. Moreover, for the broadband designs, an additional factor (referred to here as the percent power) is necessary to account for the impact of the device transmission curve (Lorentzian for this MRR design, sinusoidal for the MZI design, discussed later). The percent power is here calculated as the integral of the transmission curve, normalized by the total input optical power. The power remaining after accounting for component loss is multiplied by the percent power to get the final output power. The percent power in the Lorentzian shape will depend

¹The calculated loss does not include the on-chip filters, which should be included in future designs. Including this component is expected to add an additional 0.8 dB of loss [106]. In the setups described in this work, the BPTF and grating couplers added ~ 10 dB of loss, while the EDFA added ~ 10 dB of gain. Thus these components are not included.

on the Q-factor of the design used, along with variations due to manufacturing. The 30% estimate used here is based on the simulations from the design in this thesis. Likewise, the percent power in the sinusoidal curve will also depend on the width of integration (i.e., how many FSRs are included in the span of the filter). It was found that as long as the bandwidth is larger than a single FSR, the percent power should remain between 40%-50%. The results from this table demonstrate that if equivalent optical powers are input to each design, the fixed-wavelength laser design will produce the highest optical output.

Experimental results and analysis

As a proof-of-concept, we simulated a biosensing experiment by replacing the sensing ring with an electrically tunable MRR (Fig 3.3). By setting the voltage of the sensing MRR while scanning the voltage of the tracking MRR, a simulated bio-experiment was performed. Fig 3.3b shows the IRPHD photocurrent as a function of the tracking MRR voltage for various sensing MRR voltages (using the scanning method discussed in Section 3.1.1). The sensitivity was extracted from this curve in units of $W_{\text{tracker}}/V_{\text{sensor}}$. To convert sensitivity (S_{MRR}) into units of $W_{\text{tracker}}/\text{RIU}$, we can use the following equation:

$$S_{\text{MRR}} \left[\frac{\text{W}}{\text{RIU}} \right] = \frac{S_{\text{MRR}} \left[\frac{\text{W}}{\text{V}} \right] \times \frac{\delta\lambda}{\delta n_{\text{eff}}} \times \frac{\delta n_{\text{eff}}}{\delta n_{\text{clad}}}}{\frac{\delta\lambda}{\delta V}} \quad (3.1)$$

The change in resonant wavelength due to the change in voltage ($\frac{\delta\lambda}{\delta V}$) can be extracted by monitoring the transmission of the MRR as different voltages are applied to the IRPHD. The change in resonance wavelength due to a change in the effective index ($\frac{\delta\lambda}{\delta n_{\text{eff}}}$) can be calculated using Equation 2.6. The waveguide mode sensitivity ($\frac{\delta n_{\text{eff}}}{\delta n_{\text{clad}}}$) describes the change in effective index due to a change in the cladding index, and was extracted from simulations. Using this conversion, a sensitivity of 0.98 W/RIU was determined.

Broadband MRR							
Component	Directional coupler	Ring (in water [57])	Routing waveguide	Ring (in oxide)	Total loss	Lorentzian curve	Total power remaining
Loss	0.1 dB	5 dB/cm	3 dB/cm	3 dB/cm	0.74 dB (15.7%)	30%	25.3%
Length/Number	4	50 μm	1 mm	50 μm			
Broadband MZI							
Component	Y-branch [108]	Waveguide (in water)	Routing waveguide	Waveguide (in oxide)	Total loss	Sinusoidal curve	Total power remaining
Loss	0.3 dB	5 dB/cm	3 dB/cm	3 dB/cm	1.9 dB (35.4%)	45%	29.1%
Length/Number	4	500 μm	1 mm	500 μm			
Fixed-wavelength MRR							
Component	Directional coupler	Strip to multimode converter [109]	Multimode waveguide [109]	Strip to SWG converter [110]	SWG (in water)	Total loss	Total power remaining
Loss	0.1 dB	0.02 dB	0.085 dB/cm	0.1 dB	8 dB/cm	2.3 dB (41.1%)	58.9%
Length/Number	1	4	1 mm	16	640 μm		

Table 3.1: Summary of the remaining power incident on the photodetector after accounting for losses in each sensor design. After accounting for losses in the broadband designs, the final power must also be multiplied by the percent power corresponding to the design's transmission curve (Lorentzian or sinusoidal).

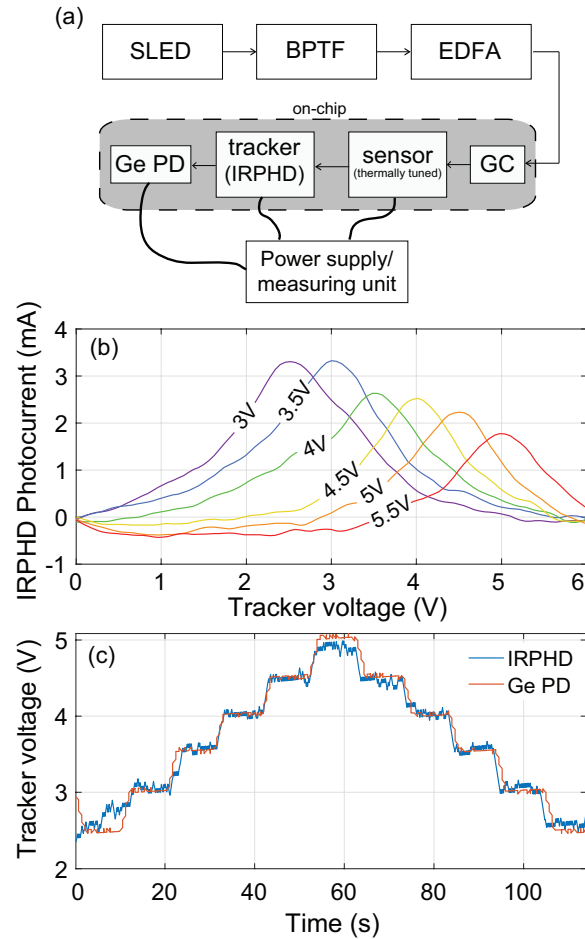


Figure 3.3: (a) Experimental setup used for the measurements in (b) and (c). An SLED broadband source was filtered using a BPTF and amplified with an EDFA before being coupled on chip using grating couplers (GCs). The sensor and tracker MRR were electrically controlled using an off-chip source meter. The photocurrent from the IRPHD and Ge PD was also measured using the off-chip source meter. (b) The IRPHD photocurrent as a function of the tracking ring voltage at various sensing ring voltages (indicated as legends on the line plots). (c) Tracker voltage to maximize the photocurrent (from the IRPHD and Ge PD) at various sensing ring voltage setpoints across time, implemented using a maximum search algorithm (the dither signal can be seen).

Sensitivity values for SiPh sensors are typically reported in units of nm/RIU. This conversion can be made using [103]:

$$S \left[\frac{\text{nm}}{\text{RIU}} \right] = S \left[\frac{\text{W}}{\text{RIU}} \right] \times \frac{\delta\lambda}{\delta P} \left[\frac{\text{nm}}{\text{W}} \right] \quad (3.2)$$

where $\delta\lambda/\delta P$ is the change in wavelength due to a change in applied power. This can be determined by monitoring the output transmission as a function of applied power. For this design, the extracted value was 80 nm/W. This gave a sensitivity of 78.8 nm/W.

The high dynamic ranges of IRPHDs suggest that low optical input powers (<-30 dBm) can be detected. To compare and contrast the IRPHD performance versus that of the Ge PD, we tuned the sensing MRR in real-time and tracked the voltage change of the tracking MRR, once by maximizing the IRPHD photocurrent, and once by maximizing an on-chip Ge PD (placed at the drop port of the tracking MRR (Fig 3.2c)). Fig 3.3b shows the real-time tracking, for the Ge PD and IRPHD, using a maximum search algorithm (discussed in Section 3.1.1); similar performance was obtained, suggesting that the IRPHDs are suitable in a sensing system.

To investigate the sLoD of the system using the IRPHD versus the Ge PD, the noise of the IRPHD and Ge PD were extracted from Fig. 3.3. Fig. 3.4 displays the noise floor of the power at the maximum current for each detector. After detrending, a 110 μW and 51 μW standard deviation was obtained for the IRPHD and Ge PD, respectively, indicating a detection limit of 3.4×10^{-4} RIU and 1.6×10^{-4} RIU, respectively, using Equation 1.1. While the Ge PD has slightly better performance compared to the IRPHD, both sLoDs are similar to values reported for other SiPh sensors, which range from 10^{-3} to 10^{-6} RIU [23]. Furthermore, the noise reported here is significantly higher than the intrinsic noise for both PDs [111], as we are measuring the system noise, which includes other sources of noise (such as the power source or the coupling conditions). In a system controlled and measured via integrated CMOS electronic devices, the noise from additional components (i.e., the trans-impedance amplifier and analog-to-digital converter [82, 112]) will be greater than the intrinsic noise of the PD. The slightly higher noise from the IRPHD is thus not large enough to noticeably influence the system.

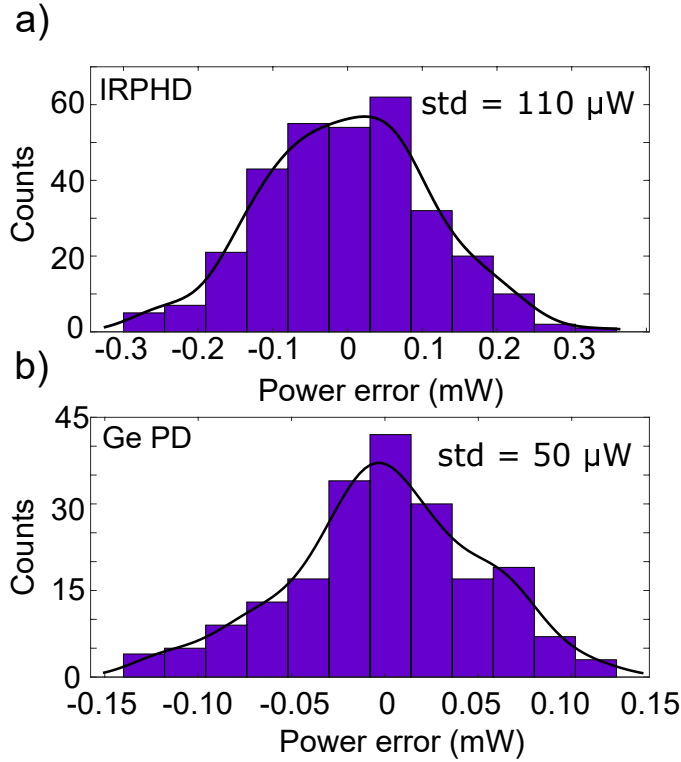


Figure 3.4: System noise of the (a) IRPHD architecture and (b) GePD architecture, measured for 2.5 min and 10 min, respectively. Inset: Histogram of noise distribution with standard deviation results.

A second test device was fabricated with the oxide removed from the sensor MRR, allowing it to be directly exposed to samples. The performance of the sensor was characterized by using a series of isopropyl alcohol (IPA) dilutions from 0% to 20% v/v (Fig 3.5). The voltage corresponding to the maximum IRPHD photocurrent was recorded for each IPA concentration by sweeping the applied voltage of the tracking ring (as discussed in Section 3.1.1), obtaining a bulk sensitivity of 101.7 V/RIU (61.8 nm/RIU) and an sLoD of 9.8×10^{-4} RIU. Although this sensitivity is worse than the state of the art MRR sensors [23], it is similar to standard transverse electric (TE) MRR sensitivities. Since these experiments were designed to validate the IRPHD as the tracking MRR and detector, efforts were not made to optimize the performance of the sensing MRR. However, the sensitivity and limit

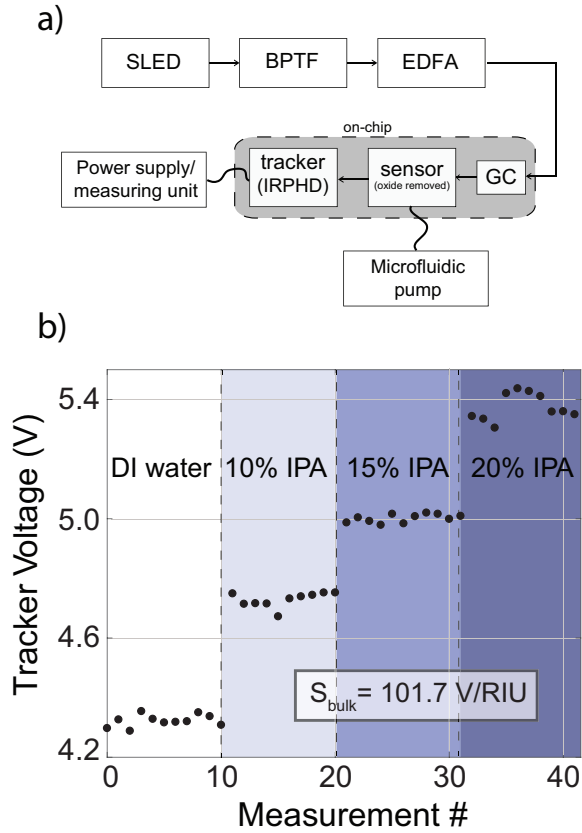


Figure 3.5: a) Experimental setup used for the measurements in b). An SLED broadband source was filtered using a BPTF and amplified with an EDFA before being coupled on chip using GCs. The sensor had a microfluidic channel above it, allowing it to be exposed to the IPA dilutions. The tracker IRPHD was electrically controlled and measured using an off-chip source meter. b) Sensogram of the sensor/IRPHD system response to the introduction of IPA dilutions to the sensing ring. A sensitivity of 101.7 V/RIU (or 61.8 nm/RIU) was extracted.

of detection of this system could be improved by replacing the simple TE strip waveguide with transverse magnetic (TM), slot or SWG rings, which have been shown to produce higher sensitivity [23]. Furthermore, by optimizing the coupling efficiency of the broadband source to the chip, the SNR can be increased, further lowering the sLoD.

3.1.2 Broadband MZI design

In this section, we propose and demonstrate a low-cost silicon photonic sensor similar to the broadband MRR design described above, but instead based on MZI elements. The operational principles of MZI sensors are discussed in Section 2.1.2. Compared to the MRR design, MZIs: (1) are simpler to design, (2) provide sensitivities that can be scaled with component length, and (3) utilize more of the optical power from the broadband source, enabling a higher SNR. A sensitivity of 3.88 W/RIU (322 rad/RIU) and a system limit of detection of 7.7×10^{-4} RIU is demonstrated.

Operating principle

The broadband MZI sensor operates very similarly to the MRR broadband design: light is input to a sensor MZI, which is followed by a tracker MZI (that is thermally controlled by a heater) (Fig 3.6a). The optical transmission spectra of both MZIs are initially aligned by applying an initial electrical power to the tracker MZI, resulting in a high output transmission (Fig 3.6b). When interaction with an analyte induces a phase change ($\Delta\phi$) in the sensor MZI, causing its transmission spectrum to shift, a new electrical power must be applied to the tracker MZI to realign the spectra. By measuring the change in applied electrical power (ΔW) to the tracker MZI, the change in RIU of the sensor MZI can be determined. The change in applied electrical power can similarly be tracked using a scanning or maximum search method; the experiments in this section use the scanning method, since it provides a more reliable method for determining the peak position, as discussed in Section 3.1.1.

Device design and fabrication

The test devices were fabricated using electron beam lithography by Applied Nanotools Inc [113]. This fabrication was performed without any dopants, inhibiting implementation of IRPHDs or other on-chip PDs. Additionally, no oxide open step was performed on the chip, therefore a sensor test with real solutions was not possible. However, several metal layers were available and so, both the sensor and tracker MZIs were fabricated with heaters. The heater on the sensor enabled the

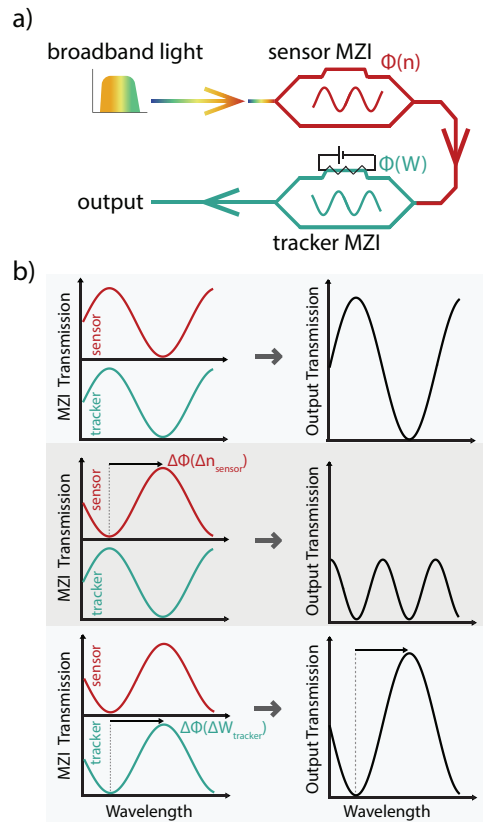


Figure 3.6: a) Layout of the broadband MZI design, consisting of a sensor MZI and a tracker MZI, the latter of which is thermally controlled by a resistive heating element.¹ b) Transmission spectra of sensor and tracker MZI (first column) and the resultant output (second column). Initially the transmission spectra are aligned, producing a peak output transmission. When the sensor MZI has a phase shift due to a change in the effective index, Δn , the output is lowered. The tracker phase is realigned to the sensor by applying a power, ΔW . By monitoring the ΔW required to keep the transmission spectra aligned, the Δn caused by the target analyte can be extracted.

simulation of a biosensing experiment.

Three different test MZIs were designed, each with a different ΔL , but all had the same sensing arm length, L_{sens} . This resulted in distinct FSRs for each device

¹This figure is adapted from the author's EECE 584 course project report (see Appendix A).

(Table 3.2). Because the sensing MZI was not exposed to solutions in this experiment, its group index was essentially identical to that of the tracker MZI (slight variations exist due to fabrication), resulting in identical FSRs for both the sensing and tracking MZI.

The experimental setup is almost identical to that of the broadband MRR design (Fig 3.2). An optical broadband source (LUXMUX BeST-SLED) was input to a BPTF, followed by an EDFA to compensate for the BPTF and on-chip grating coupler losses. In this case, while the BPTF was not necessary since the FSRs of both MZIs were nearly identical, it was kept in place to simulate what a real sensing experiment would look like. Because no PDs were on-chip, the light was coupled out using grating couplers and measured with an off-chip PD (Section 3.1.1 describes the expected optical power output for this system). The on-chip heaters for each MZI were contacted using electrical probes, with electrical power applied and measured using a Keithley 2604B SourceMeter SMU.

	ΔL (μm)	FSR (designed)	FSR (measured)	Sensitivity (W/RIU)	sLoD (RIU)
MZI₁	200	2.87 nm	2.75 nm	3.88	7.7×10^{-4}
MZI₂	100	5.71 nm	5.67 nm	5.09	5.8×10^{-4}
MZI₃	50	11.38 nm	11.30 nm	7.70	3.9×10^{-4}

Table 3.2: Summary of broadband MZI results. The designed and measured FSRs are within 5% tolerance, with deviations due to fabrication variations. With the exception of MZI₃, the sLoDs are within commonly reported SiPh sensor ranges.

Experimental results and analysis

Several of the experiments discussed in Section 3.1.1 (for the broadband MRR design) were repeated for the broadband MZI design. To understand and analyze the spectrum more precisely, the transmission spectrum was collected using a tunable laser (Fig 3.7 displays the results for MZI₁). While their nominal designs were equivalent, the transmission spectra of the tracker and sensor MZIs in the system were slightly offset due to fabrication variations. Here, we can extract the FSRs for each MZI design, and compare to the designed value (Table 3.2). To realign the

transmission spectra, a voltage of 2.5 V was applied to the tracker heater (Fig 3.7 orange data).

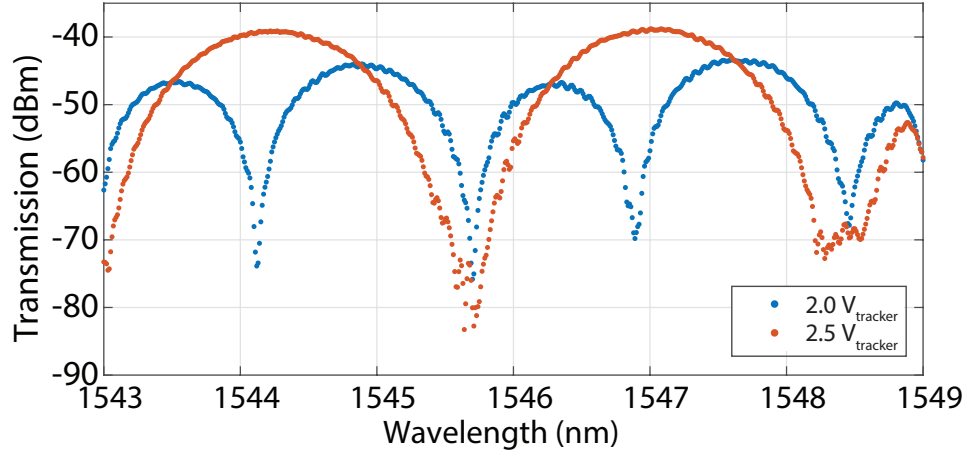


Figure 3.7: Transmission spectra of MZI_1 , obtained using a tunable laser. The blue data shows that a 2.0 V signal applied to the tracker MZI_1 offsets the spectra, allowing the FSRs of each to be extracted. The orange data is the transmission spectrum when 2.5 V is applied to the tracker MZI_1 . We see that the spectra are roughly overlapped. This is expected as their designs are equivalent.

Next, different voltages were applied to the sensor MZI, and the electrical power was scanned on the tracker MZI to find the maximum optical power input to the PD (Fig 3.8a displays the experimental setup, and b shows the results for MZI_2 . Plots for MZI_1 and MZI_3 are included in Fig ??). The sensitivity (in units of $W_{\text{tracker}}/W_{\text{sensor}}$) can be obtained by tracking the electrical power applied to the tracker MZI that corresponds to the peak optical power transmission through the device. To convert sensitivity (S_{MZI}) into units of $W_{\text{tracker}}/\text{RIU}$, we use an equation similar to that for the MRR (Equation 3.1):

$$S_{\text{MZI}} \left[\frac{\text{W}}{\text{RIU}} \right] = \frac{W_{\text{tracker}}}{W_{\text{sensor}}} \times \frac{\delta\phi}{\delta n_{\text{eff}}} \times \frac{\delta n_{\text{eff}}}{\delta n_{\text{clad}}} \quad (3.3)$$

The change in resonant wavelength due to the change in applied power ($\frac{\delta\phi}{\delta P}$) can be extracted by monitoring the transmission of the MZI as different voltages are

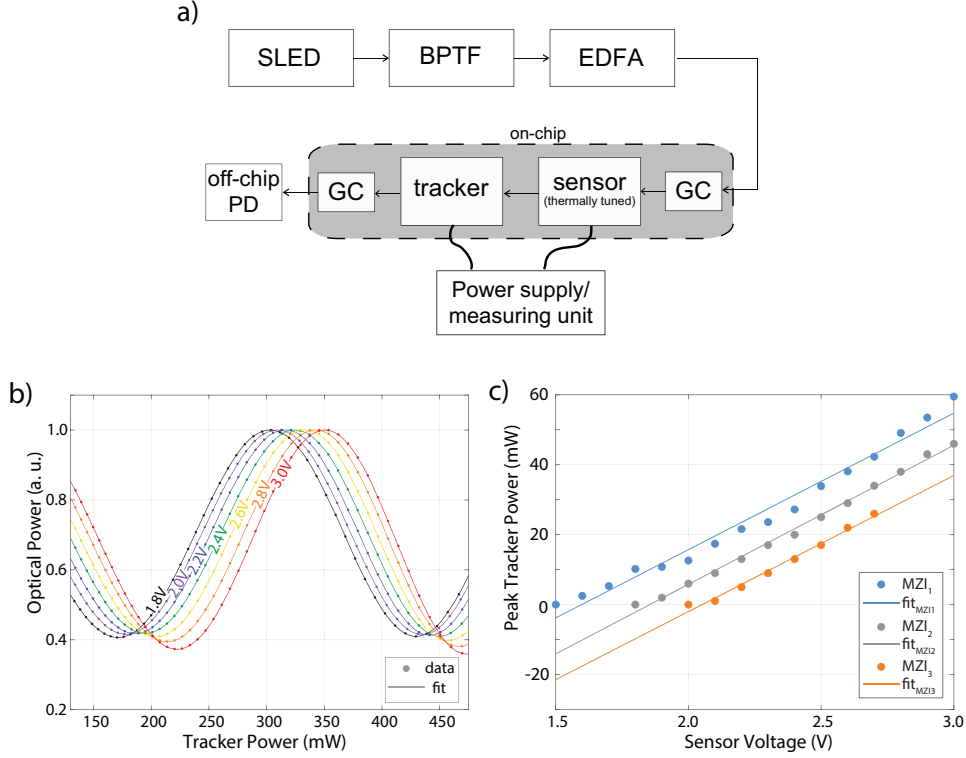


Figure 3.8: a) Experimental setup used for the measurements in b and c. An SLED broadband source was filtered using a BPTF and amplified with an EDFA before being coupled on chip using GCs. The sensor and tracker MZIs were electrically controlled using an off-chip source meter. The optical output was coupled off-chip using GCs and measured with an off-chip PD. b) The detected output optical power as a function of power applied to the tracker MZI₂, at various sensor MZI₂ voltages (indicated as legends on the lineplots). c) The applied tracker MZI power corresponding to peak detected optical power as a function of sensor MZI voltage, for each MZI design. Each data set was fit to a line, with the slope corresponding to the sensitivity of each MZI (in $\text{mW}_{\text{tracker}}/\text{V}_{\text{sensor}}$).

applied to the heater (values of 83.3 rad/W, 58.3 rad/W, and 38.3 rad/W were extracted for MZI₁, MZI₂, and MZI₃, respectively). The change in the phase due to a change in the effective index ($\frac{\delta\phi}{\delta n_{\text{eff}}}$) can be calculated using Equation 2.3. The waveguide mode sensitivity ($\frac{\delta n_{\text{eff}}}{\delta n_{\text{clad}}}$) describes the change in effective index due to

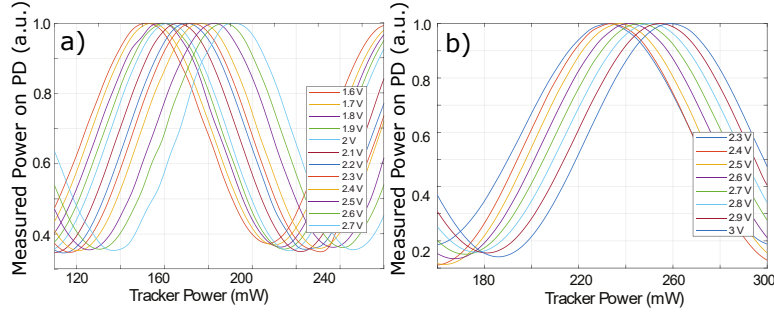


Figure 3.9: The detected output optical power as a function of power applied to the tracker MZI, at various sensor MZI voltages (indicated in legends) for a) MZI₁ and b) MZI₃.

a change in the cladding index, and was extracted from simulations. The extracted values are summarized in Table 3.2, with the highest sensitivity corresponding to 7.7 W/RIU.

To convert this sensitivity into units of rad/RIU, we use an equation similar to that for the MRR (Equation 3.2):

$$S \left[\frac{\text{rad}}{\text{RIU}} \right] = S \left[\frac{\text{W}}{\text{RIU}} \right] \times \frac{\delta\phi}{\delta P} \left[\frac{\text{rad}}{\text{W}} \right] \quad (3.4)$$

where $\delta\phi/\delta P$ is the change in phase due to a change in applied power. The average sensitivity obtained for the broadband MZI design was 309 rad/RIU. This is on the inferior end of sensitivity ranges reported for MZI structures [23], however, like the MRR design, this value could be improved by using sensitivity-enhancing structures, such as SWGs, slots, or TM waveguides.

The above equations are based on several assumptions. The first is that the shift in the tracker MZI transmission linearly follows the shift in the sensor MZI transmission. However, this may not be the case, depending on the ratio between the filter bandwidth and the FSR of the device. Calculations to determine this relationship were performed by integrating the expected transmission curve of two cascaded MZIs to get the expected power incident on the PD, given by¹:

¹This equation is modified from the author's EECE 584 course project report (see Appendix A); it is used here for a separate set of analyses.

$$\int_a^b \sin^2(\phi - k) \times \sin^2(\phi - j) d\phi \quad (3.5)$$

where $\sin^2(\phi - k)$ and $\sin^2(\phi - j)$ describe the transmission of the sensor and tracker MZI with phase shift k and j , respectively, and a and b describe the optical filter bandwidth. When the bandwidth of the filter is equal to integer multiples of the FSR, the tracking follows linearly (Fig 3.10a black line). However, if the bandwidth is in between these values, the linear relationship no longer holds (Fig 3.10a coloured lines). This deviation from linearity decreases as more full FSRs are included in the bandwidth. When the bandwidth is less than a full FSR, the relationship is very nonlinear. For our designs, we had FSRs equal to 2.09, 1.05, and 0.52 times the input optical bandwidth, corresponding to MZI₁, MZI₂, and MZI₃, respectively. Fig 3.10b displays the deviations that this causes in our measurements. This adds a fundamental uncertainty in our measurements of 0.05 rad, 0.06 rad, and 1.3 rad (i.e., if a phase shift of $\pi/2$ is measured in the tracker MZI₁, the real phase shift in the sensor MZI₁ is $\pi/2 \pm 0.05$ rad), corresponding to MZI₁, MZI₂, and MZI₃, respectively.

Another assumption in these equations is that the sensitivity of this cascaded MZI system has the same sensitivity expression as a single MZI. This may not be the case, since the MZI is not operating at its quadrature point where its slope is the highest, and further investigations are necessary to determine the sensitivity relationship for this system. Furthermore, the larger optical bandwidth used in this system corresponds to a shorter coherence length, which reduces the fringe visibility (i.e., the contrast in the interference pattern). In particular, the coherence length (L_c) for our design is approximated (for a square-like source) by [114]:

$$L_c = \frac{\lambda^2}{n_g \Delta\lambda} = \frac{(1550 \text{ nm})^2}{4.3 \times 6 \text{ nm}} \approx 93 \text{ } \mu\text{m} \quad (3.6)$$

where λ is the wavelength, n_g is the group index, and $\Delta\lambda$ is the bandwidth of the optical source. Here, we obtain a coherence length of 93 μm . Since the path length differences in MZI designs were 200 μm , 100 μm , and 50 μm (for MZI₁, MZI₂, and MZI₃, respectively), this corresponds to approximately $\frac{1}{2}L_c$, $1L_c$, and $2L_c$, respectively. Since a single coherence length corresponds to 37%-50% fringe

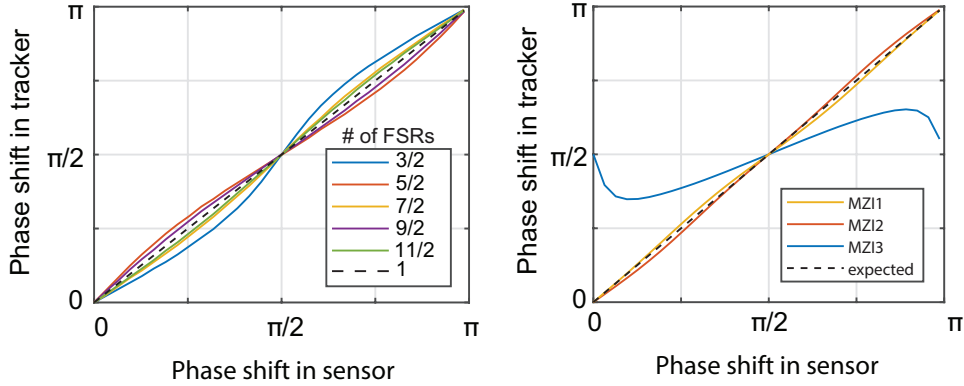


Figure 3.10: a) Tracker phase shift required for maximum power output as a function of sensor phase shift, for bandwidths equal to half-integer multiples of the FSR. As more full FSRs are included in the bandwidth, the tracker matches the sensor more linearly at non-integer FSR values. The black dotted line shows the linear value, where exact integer multiples of the FSR are included in the bandwidth (in this case, exactly one FSR). b) Tracker phase shift required for maximum power output as a function of sensor phase shift, for the different MZI configurations in this section. Since the bandwidth was kept constant at 6 nm, the number of bandwidths included is equal to 6 nm divided by the FSR of the device. For MZI₃, a full FSR was not within the bandwidth, leading to very large deviations.

visibility (for a single MZI), the visibility for the 200 μm case will thus be significantly reduced. Further investigations are necessary to determine the impact that this reduced fringe visibility has on the cascaded MZI system.

System noise measurements were also performed for this setup. The power applied to the sensing MZI was kept constant, and the power was repeatedly swept on the tracker MZI for just under 2 minutes. The tracker power for maximum transmission was obtained (Fig 3.11), detuned, and analyzed for noise. The 3σ deviation was 3 mW. This allowed us to obtain an average sLoD of 5.8×10^{-4} RIU (using Equation 1.1). The device performances are summarized in Table 3.2.

One of the major drawbacks of an MZI sensor is its size, which can lead higher sensitivity to environmental noise sources such as temperature fluctuations [79]. A small investigation was performed towards characterizing this dependence. In

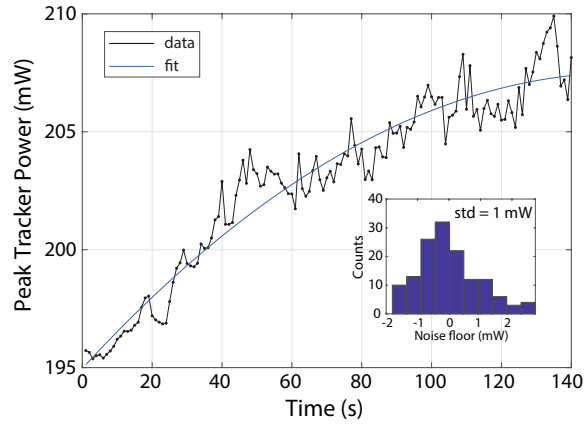


Figure 3.11: System noise in the MZI₁ system, extracted by monitoring the system for 140 seconds. The data was fit with a quadratic function, used to detrend the data. A histogram of the noise distribution is inset, with a standard deviation of ~ 1 mW.

the experimental setup, the SiPh device is placed on a programmable, thermally-controlled stage. By changing the temperature slightly on the stage, temperature fluctuations in the environment can be simulated. Fig 3.12 displays these results. Over a temperature difference of 0.2°C , the tracker power shifted 0.6 mW. Linearly fitting the data produces a slope of $2.9 \text{ mW}/^\circ\text{C}$. Because the sensing arm lengths of each MZI were equivalent, the temperature dependence on arm length could not be experimentally extracted, but it is expected to scale with arm length (as does the sensitivity). This highlights the importance of a completely standalone reference MZI that can be used to monitor sensor drift over time.

3.1.3 Comparison of architectures

While standalone MRRs and MZIs were briefly contrasted in Section 2.1.5, here we compare the performance of the broadband MRR and MZI sensor designs (summarized in Table 3.3). The sensitivities of the MRR and MZI were $78.9 \text{ nm}/\text{RIU}$ ($0.98 \text{ W}/\text{RIU}$) and $322 \text{ rad}/\text{RIU}$ ($3.88 \text{ W}/\text{RIU}$), respectively. SiPh sensor sensitivities are typically given in nm/RIU since the wavelength is being tracked, with a higher sensitivity being more desirable. In the broadband sensor designs, the tracker power is being measured, resulting in a measured sensitivity in W/RIU .

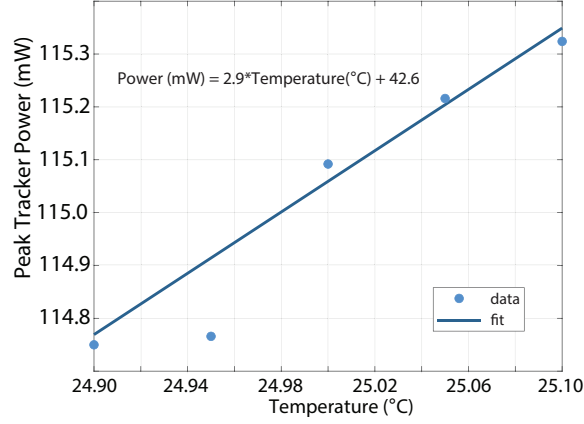


Figure 3.12: Tracker power as a function of temperature, measured in the MZI₁ design. After fitting, we see that a 1°C change in temperature change results in a 2.9 mW change in tracker power. If temperature fluctuations are not accounted for in sensing measurements, it may result in incorrect readings.

However, representing sensitivity in W/RIU introduces challenges when comparing devices, and makes it unclear whether a higher sensitivity is better, since there is a tradeoff between higher device sensitivity and higher electrical power. The measured tracker power is a function of both how sensitive the element is to a change in effective index and a function of the electrical heater efficiency. A higher sensitivity (in W/RIU) could mean that the design is actually more sensitive to RIU changes, but it could also indicate a poor heater design, resulting in a higher power required for the same refractive index shift. The broadband MRR and MZI designs reported here used different heater designs (the MRR was based on doped heaters, the MZI was a metal heater), therefore their heater efficiencies are quite different. Therefore, a comparison in W/RIU does not accurately reflect the sensor performance.

The converted units (in nm/RIU) are independent of the heater efficiency. However, as discussed in Sections 2.1.3 and 2.1.2, the MZI has a length-dependent sensitivity, which is given by [57]:

$$S_{\text{MZI}} = \frac{2\pi L_{\text{sens}}}{\lambda} \left(\frac{\delta n_{\text{eff}}}{\delta n_{\text{clad}}} \right) \quad (3.7)$$

	Sensitivity (W/RIU)	Sensitivity (RIU⁻¹)	sLoD (RIU)
MRR	0.98	78.9 nm	3.4×10^{-4}
MZI	3.88	322 rad	7.7×10^{-4}

Table 3.3: Summary of key FOMs for the broadband MRR and MZI designs. Sensitivity in nm/RIU or rad/RIU represents a more accurate representation, as it is not dependent on the heater efficiency. sLoD is difficult to compare as the system noise was not constant across measurements.

where L_{sens} is the length of the sensing arm of the MZI, λ is the wavelength of light, and $\left(\frac{\delta n_{\text{eff}}}{\delta n_{\text{clad}}}\right)$ is the waveguide sensitivity. The sensitivity of the MRR is given by [57]:

$$S_{\text{MRR}} = \frac{\lambda}{n_g} \left(\frac{\delta n_{\text{eff}}}{\delta n_{\text{clad}}} \right) \quad (3.8)$$

where n_g is the group index. Since the MRR sensitivity does not depend on component size, it is impossible to scale the sensitivity with geometry. Without performance-enhancing structures like SWGs, slot, or TM waveguides, it is difficult to increase the light-matter interaction in the MRR that is needed for higher sensitivity. The MZI, on the other hand, can simply be made larger. Since the sensitivities of these devices are fundamentally linked to their geometries, the sensitivity results are thus not a good metric for comparison.

Using Equations 3.7 and 3.8 above, we can also calculate the expected sensitivities from these devices, using a simulated waveguide mode sensitivity of $0.18 \text{ RIU}_{\text{neff}}/\text{RIU}_{\text{nclad}}$ for both MRR and MZI devices (as the same strip waveguide was used). The results are summarized in Table 3.4. Here, the sensitivity for the broadband MRR extracted experimentally using isopropyl alcohol matches well with the simulated value. However, the sensitivity for the MRR extracted using thermal tuning is higher than the expected value. This is likely because the thermal tuning experiments change the refractive indices of both the core waveguide and the surrounding cladding, whereas the equations and simulations expect the refractive index change to be isolated to the cladding. While the thermal tuning experiments are useful for proof-of-concept demonstrations, the extracted values for

		Calculated sensitivity (RIU⁻¹)	Measured sensitivity (RIU⁻¹)
Broadband MRR	Isopropyl alcohol	69.4 nm	61.8 nm
	Thermally tuned	69.4 nm	78.9 nm
Broadband MZI	MZI ₁	373 rad	322 rad
	MZI ₂	373 rad	304 rad
	MZI ₃	373 rad	302 rad

Table 3.4: Simulated versus measured sensitivities for the broadband designs. The measured values from the isopropyl alcohol experiment match well with simulated values. The sensitivity extracted from the thermal tuning experiments for the MRR produced a higher value than expected, likely due to the refractive index change not being isolated to the cladding. The MZI designs have lower sensitivities than expected, likely arising from the nonlinearity in their tracking method or manufacturing variations.

sensitivity (and therefore also sLoD) may not accurately reflect the results expected in a sensor system measuring a real analyte. Additionally, the broadband MZI measured sensitivities are lower than expected. This may be due to the non-linearity in their tracking (discussed in Section 3.1.2), or due to deviations in the waveguide mode sensitivity arising from manufacturing variations (see Appendix A).

The sLoD values are also reported in Table 3.3. Since these are system LoD, this parameter factors in the noise from the experimental set-up. The noise factors for both systems were slightly different for both designs. The PDs were off chip for the MZI design and heaters were used. The MRR had wirebonded electrical pads, while the MZI pads were contacted using electrical probes. These differences in system noise makes it difficult to arrive at strong conclusions on the relative performance of the platforms, although the MRR sLoD is an order of magnitude better than that of the MZI. The MZI design suffers from the deviations in the linearity of the sensitivity, which adds additional uncertainty. However, more similar experimental setups would be required to properly characterize the noise discrepancies between the MRR and MZI systems. Despite the challenge in comparing the reported values, these sLoD are similar to values reported for other SiPh sensors,

which range from 10^{-3} to 10^{-6} RIU [23]. This is very promising, as it highlights that a SiPh system is not dependent on a high-resolution laser to achieve high sensor performances.

While both the MRR and MZI architectures operate on the same principles of a sensor and tracker element, their results are fundamentally different due to the differences in their transmission spectra. When the sensor and tracker are misaligned in the MRR case, very low (< -60 dBm) transmissions are possible, as the responses correspond to convolutions of Lorentzian-based transmission curves (Fig 3.13a). The peak measured power is highly dependent on the Q-factor of the rings, with high Q-factors leading to near-zero transmission when misaligned. As investigated by Prasad et al. [115], a high Q-factor is necessary for a high SNR in the sensor-tracker system. Furthermore, a near-zero transmission can be problematic if the maximum search detection algorithm is used to find the resonance alignment (as discussed in Section 3.1.1). If no power is transmitted and the slope of transmission curve is roughly flat, the maximum search algorithm may get stuck in noise, and it may be difficult to realign the peaks. The MZI transmission, on the other hand, is sinusoidal, resulting in a high optical (> -20 dBm) transmission even when the sensor and tracker are misaligned (Fig 3.13b), which should make it easier to keep track of the peak power. However, this misalignment issue will not arise in the scanning method, which, as discussed in Section 3.1.1, provides a more reliable method for determining the peak position. Thus, this near-zero transmission of the MRRs when misaligned should not impact device performance.

Finally, the design size must also be considered when choosing the architecture that makes more practical sense in a sensing system. As previously discussed, the MRR is significantly more compact than an MZI. The footprint savings of the MRR are doubled compared to the MZI design, since two elements are needed for each sensor. Furthermore, the MRR design suggested here has further footprint savings since the PD and heater are combined. While an IRPHD could be implemented in the MZI design, it would have to be placed at the output of the MZI, rather than contained within it (since the sinusoidal transmission is not detected within the MZI). This increases the footprint of the MZI design by requiring space for the PD, and also increases the number of electrical contacts. Overall, the MRR design footprint is significantly smaller than even the smallest MZI architecture.

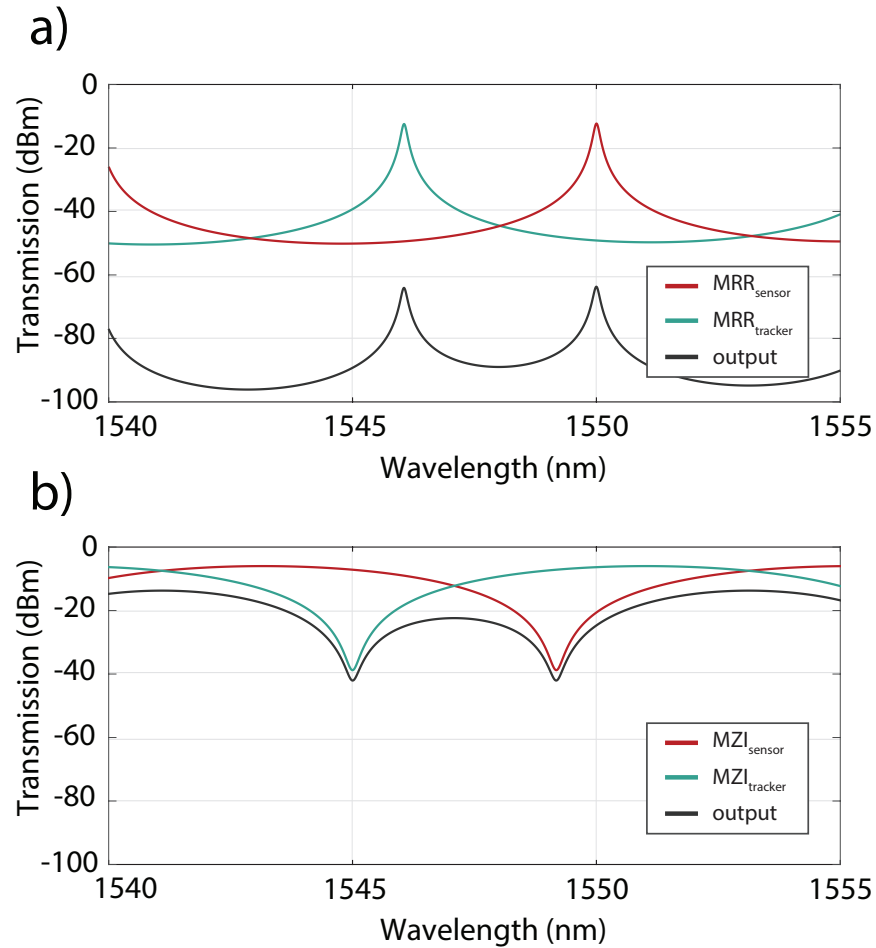


Figure 3.13: Simulated optical spectrum and transmission when the tracker and sensor are slightly out of phase for a) the MRR design and b) the MZI design. In a), we see very low transmission output as the Lorentzian curves do not have any overlap. In b), we continue to detect a signal due to the sinusoidal nature of the transmission, although it is not at its maximum.

3.1.4 Design benefits and optimization

By using a broadband source rather than a tunable laser, the cost of implementing silicon photonic sensor systems is significantly reduced. Furthermore, in a tunable laser architecture, the system limit of detection is limited by the resolution of the

laser. In order to lower the limit of detection, the wavelength resolution of the laser must be increased, which further increases costs. In broadband source architectures, the sLoD is dictated by the resolution of the power supply, which can be increased in a much more cost-effective way.

A broadband source can also simplify the coupling process for multiplexing systems. Designs that include multiple sensors can be used for noise cancellation between sensors, thus lowering the limit of detection, and for detection of multiple analytes on the same chip. In lieu of using mechanical coupling systems, both the tunable laser and broadband coupling will be limited by the number of input channels that can be attached to the chip. In order to route light to multiple sensors, the light needs to be split on chip. This reduces the optical power in each sensor, and can reduce performance. While the optical power can be scaled, laser amplification significantly increases the noise [116], thus reducing sensor performance. Furthermore, the sensor-tracker broadband source architecture does not have to suffer from reduced optical power when multiplexing, since only a small bandwidth of light is used for each sensor. Instead of splitting the optical power, this system could split the light based on wavelength, sending separate wavelength bands to each sensor. The broadband source used in our experiments has a bandwidth of 35 nm, however we only use a small bandwidth (corresponding to the band over which the sensor and tracker FSRs remain similar). In these experiments, a single 6 nm window was used due to the limitations of the off-chip BPTF. By moving to on-chip bandpass filters [106], multiple bandpass filters centered at different frequencies could be implemented, allowing for multiple sensors in either the MRR or the MZI design (Fig 3.14). The number and bandwidth of the filters will depend on the expected sensor range (i.e., the maximum resonant wavelength shift from an expected RIU shift), the Q-factor, and the bandwidth of the broadband source. These filters will likely need thermal tuners to compensate for drifts from their designed center wavelengths due to fabrication variations. This design offers the benefits of multiplexing without sacrificing the optical power in each ring.

Additionally, using IRPHDs in place of Ge PDs broadens the range of applications in two ways. Firstly, rapid prototyping foundries (such as AMO, Applied Nanotools Inc, Cornerstone [117]) do not have germanium available in their fabrication processes. By replacing Ge PDs with IRPHDs, designers can create fully

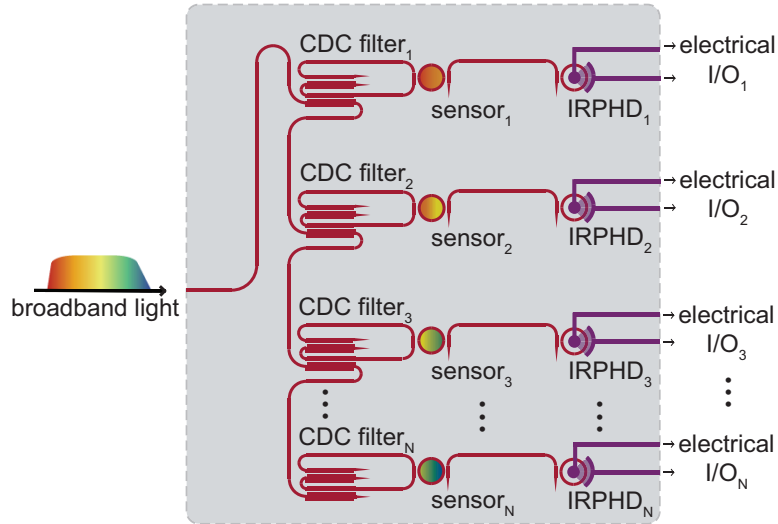


Figure 3.14: Proposed multiplexing system. Each on-chip CDC filter can be centered at a different wavelength, allowing for different bands of the light to be coupled to each sensing chip. Each sensor ring has its own IRPHD to track transmission shifts.

functional sensor designs that do not rely on off-chip detectors, at a fraction of the turnaround time for tapeouts with traditional CMOS foundries [118]. Secondly, the high temperature processing required to grow germanium on silicon introduces challenges when integrating with CMOS processes [46–49], although several foundries have solved these challenges, to different degrees [51, 119]. In the future, the control for the sensor should be accomplished using an electronic CMOS circuit integrated onto the same chip as the sensor. Since IRPHDs do not require high temperature processing, they would enable SiPh sensors to be fully integrated with CMOS devices, allowing for low-cost fabrication, and an overall more cost-effective sensing platform.

3.2 Fixed-wavelength laser design

In this section, a third low-cost SiPh sensor design is presented, in which a fixed-wavelength laser is used for the optical source. Compared to the broadband sensor architectures described above, this fixed-wavelength design: (1) uses a lower-cost

optical source, (2) benefits from simple coupling of light from source to chip, and (3) reduces the number of components by eliminating the need for an on-chip filter.

3.2.1 Operating principles

In this fixed-wavelength laser design, a single MRR contains a sensing region and a tracking region, in this case an IRPHD (Fig 3.15). A single wavelength is coupled to the ring, and the IRPHD can apply an initial power to shift the MRR resonance to align with the fixed wavelength. When the sensing region is exposed to an analyte, the resonance wavelength of the MRR will shift due to the change in effective index. Due to the misalignment between the fixed wavelength and the MRR resonance, very little optical power will be detected in the IRPHD. A new electrical power will need to be applied to the IRPHD to bring the resonance peak back to its original position, spectrally aligned with the fixed-wavelength laser (the resonance peak can be shifted to the left by reducing the power applied to the IRPHD). By measuring the change in electrical power applied to the IRPHD (using either the scanning or maximum search method discussed in Section 3.1.1), the change in the RIU of the sensor can be extracted.

3.2.2 Design and fabrication

Since a single ring must contain both an oxide open window for sensing and an electrically-tunable region for thermal control and detection, this introduces a few practical design considerations to ensure the electronics and microfluidics can be integrated smoothly. Since MRRs are typically very compact, placing the sensing region very close to the IRPHD is quite difficult for microfluidics, as the fluids need to avoid the electrical contacts. In this design, the rings were made much longer than in typical MRR designs in order to keep these regions separate.

As the size of the ring increases, the optical loss likewise increases. This is undesirable, as increased optical loss results in a lower ring Q-factor and higher iLoD. To mitigate this effect, several designs were implemented. Firstly, the circuit was designed to operate at 1310 nm wavelength rather than 1550 nm. This was chosen due to the lower water absorption at 1310 nm compared to 1550 nm [120], and also the availability of low-cost fixed-wavelength lasers at 1310 nm [121].

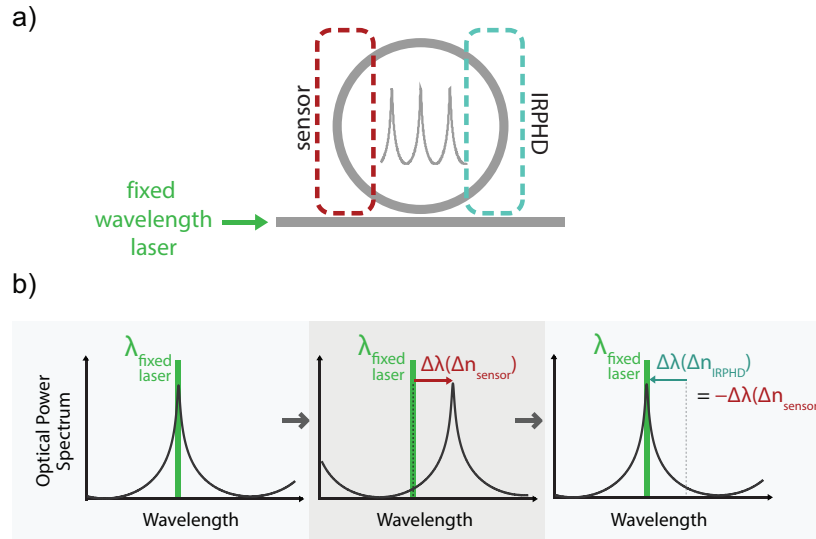


Figure 3.15: a) Layout of the fixed-wavelength laser design, consisting of a single MRR in which a portion acts as a sensing region and another portion acts as a heater/detector. b) Simulated resonances in the MRR and IRPHD output, when electrical power W_1 and W_2 are applied to the IRPHD, before and after $\Delta\lambda_{\text{res}}(\Delta n)$, respectively. By monitoring the the electrical power required to keep the transmission spectra aligned to the fixed-wavelength laser, the Δn caused by the target analyte can be extracted.

Secondly, most of the ring length was designed with wider waveguides, as this confines the light more and leads to lower loss. Finally, only a small portion of the total ring length was actually exposed to the solution, thus lowering the overall interaction with the water, and therefore lowering total loss. However, reducing the length of the sensing region also reduces the sensitivity of the design. To increase the sensitivity, SWG waveguides were implemented in the sensing region.

As discussed in Section 2.1.1, there is some difficulty in the fabrication of SWG waveguides, which is particularly undesirable when designing a robust sensor architecture. An alternative to the SWG structure is the SWG-assisted, or “fishbone” structure (Fig 3.16) [122, 123]. Since there are no free-standing pieces of silicon, this structure is less fragile in both fabrication and operation. However, having a continuous strip of silicon throughout the structure increases the effective index

of the design when compared to traditional SWG waveguides, therefore decreasing sensitivity. However, this is less detrimental at larger waveguide widths, and similar sensitivities between the SWG and SWG-assisted can be obtained.

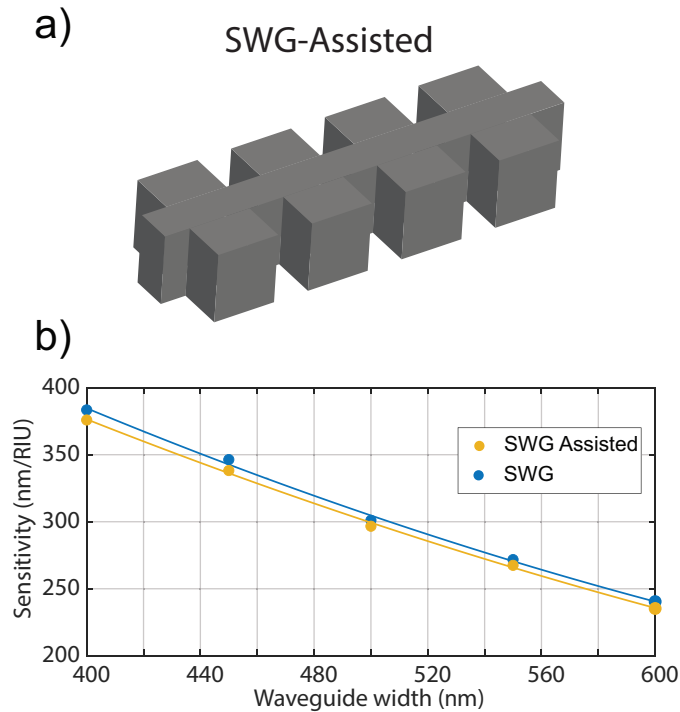


Figure 3.16: a) Layout of SWG-assisted structure. b) Sensitivity as a function of waveguide width for SWG and SWG-assisted. Similar sensitivities can be obtained by changing the width of the SWG-assisted blocks.

For traditional SWG waveguides, there is an additional mode-matching concern when converting from strip to SWG waveguides. If the modes are not changed gradually enough, the sharp difference in effective indices can cause reflections at these interfaces. While tapers can be used to help with the gradual transition (Fig 3.17a), there is still a change in effective index at the interface. To implement a smoother transition, the widths of the tapers and SWG waveguides can be designed to create a better effective index match. Simulations that varied the widths of the tapers and SWGs were performed, and the effective indices were extracted as a function of waveguide width (Fig 3.17b). In order to keep the effective indices

matched, the taper waveguide width should be on average 25 nm smaller than the SWG waveguide width, for a 50% duty cycle SWG waveguide, at a 1310 nm wavelength.

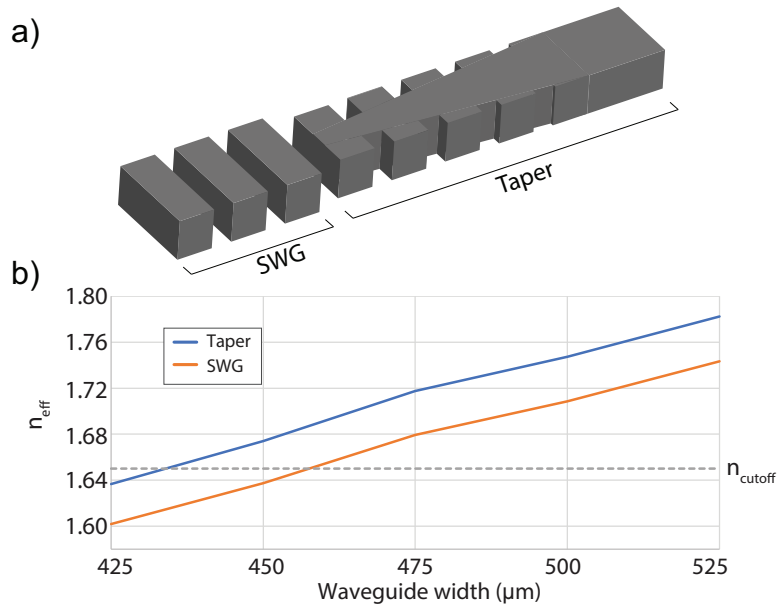


Figure 3.17: a) Layout of transition from strip to SWG waveguides. b) Effective index as a function of width for tapers and SWG waveguide, with a 50% duty cycle, at a 1310 nm wavelength. To keep the effective index of the taper and SWG waveguide matched, the taper must be designed with a width ~ 25 nm larger than the width of the SWG waveguide, as displayed in a).

To test the efficacy of this design, several devices were fabricated through Applied Nanotools Inc. Several design variations were included, as summarized in Table 3.5 and illustrated in Fig 3.18. Two different sizes of MRRs were fabricated, with the larger one having approximately 2x the circumference of the small design. For each size, a series of SWG and SWG-assisted waveguides were used in the sensing region, where either a single section (1x) or eight sections (8x) of SWG or SWG-assisted waveguides were used in the sensing region. This fabrication run did not include any active devices and therefore the IRPHD regions were not included in these designs. However, the aim of these designs was to better understand

the impacts that different design variables had on the circuit. Full simulations of this design were also performed and are discussed by Mosquera in [66], and the expected power budget for this design is included in Section 3.1.1.

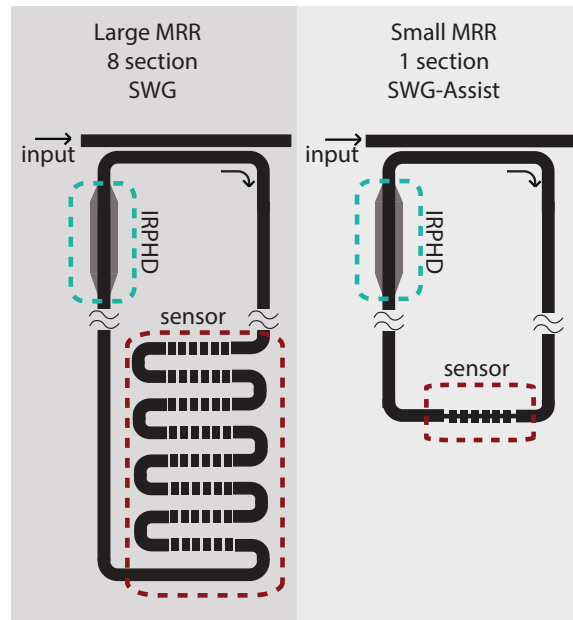


Figure 3.18: Sample diagram of design variations in the fixed-wavelength laser design. On the left, we show the large MRR with 8 sensing sections, using the SWG waveguides. On the right, we have the small MRR with 1 sensing section, using the SWG-Assist waveguides. Various combinations of large versus small, 1 section versus 8 sections, and SWG versus SWG-Assist were fabricated. The cuts shown in the ring indicate that this diagram is not to scale, as the routing waveguides are longer to keep the sensing region farther from the IRPHD.

3.2.3 Results ¹

The transmission through each device described above was taken using a high-resolution tunable laser. Resonance peaks were curve-fit with Lorentzian function, an example curve is shown in Fig 3.19. The resonance wavelengths and FWHMs

¹The measurement data for this section was obtained and provided by Hassan Rahbardar Mojaver from McGill University. It is being used here with permission.

of the peaks were extracted and used to calculate the Q-factor (using the approximation in Equation 2.7). A summary of the results is in Table 3.5.

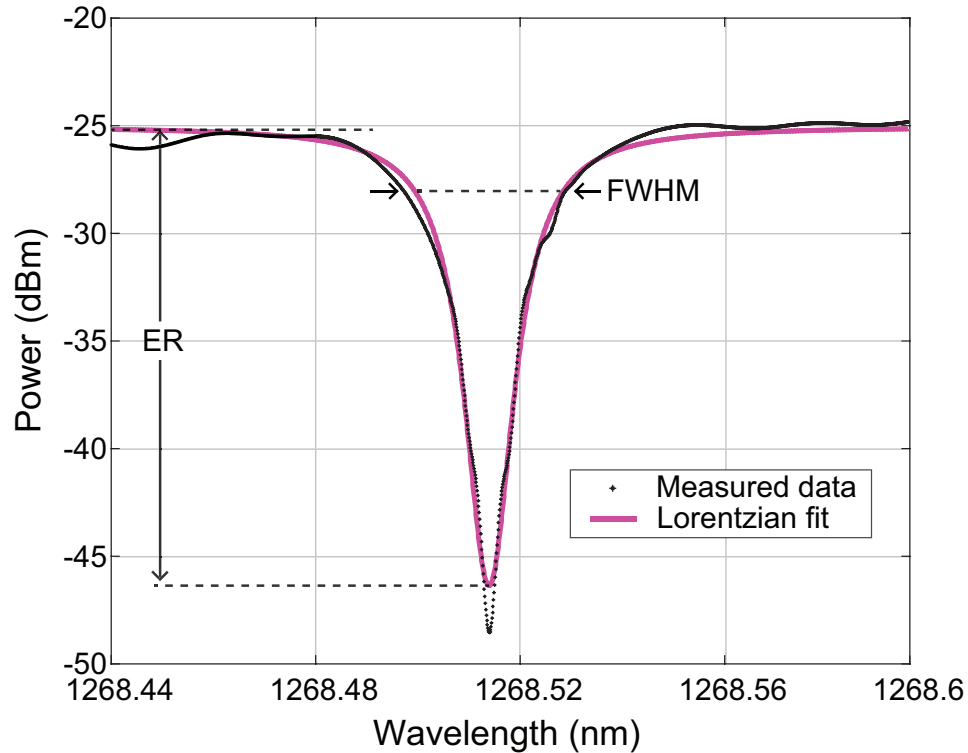


Figure 3.19: Sample resonance peak from the fixed-wavelength laser MRR design measured in water (from the small MRR 8 section SWG-Assist design outlined in Table 3.5). The full-width at half-maximum (FWHM) and extinction ratio (ER) are labelled on the graph. The Q-factor is approximated to be 44,350 using the FWHM = 28.6 pm.

The sensitivity of these devices could not be extracted since the entire structure was exposed to air. Any solution deposited would change the effective index of all elements in the design, rather than just the SWG/SWG-Assist sections, producing inaccurate sensitivity measurements, and also increasing loss significantly due to additional water absorption. However, using the simulated sensitivity values along with the extracted Q-factors, the iLoD can be calculated using Equation 2.8.

The large MRR designs have higher Q-factors compared to the corresponding

		Q factor (measured)	Sensitivity (simulated) [nm/RIU]	iLoD (calculated) [RIU]
Large MRR	1 section SWG	223,630	2.10	2.7×10^{-3}
	8 section SWG	139,090	15.7	5.8×10^{-4}
	1 section SWG-Assist	165,000	2.2	3.5×10^{-3}
	8 section SWG-Assist	121,170	16.7	6.3×10^{-4}
Small MRR	1 section SWG	60,970	12.6	1.6×10^{-3}
	8 section SWG	45,300	71.8	3.9×10^{-4}
	1 section SWG-Assist	56,040	13.3	1.7×10^{-3}
	8 section SWG-Assist	44,350	76.0	3.8×10^{-4}

Table 3.5: Summary of preliminary results for the fixed-wavelength MRR architecture.

small MRR designs, however, they also have lower sensitivity. This is because a smaller fraction of the total MRR length is exposed to the solution compared to the shorter MRR structures. Despite the high Q-factor, the long MRR designs have poorer iLoD values compared to the short MRR designs. Because of the higher sensitivity and lower iLoD, the short MRR designs are preferable to the long ones. Likewise, while the 8x devices have lower Q-factors, their increased sensitivities result in better iLoD, making them the preferred choice. In these designs, the SWG-Assist waveguides were designed with higher sensitivities (by reducing the waveguide width), resulting in slightly better iLoD performance compared to the SWG devices on average. Overall, the best performing device was the short, 8x SWG-Assist design, which demonstrated a simulated sensitivity of 76 nm/RIU, and a calculated iLoD of 3.8×10^{-4} RIU.

While these initial results are promising, a full device test with the IRPHDs and a fixed-wavelength laser has not yet been performed and will be necessary for better characterizing the performance of this design.

Chapter 4

Conclusion

In summary, we have studied silicon photonic sensor architectures that do not rely on high-resolution tunable lasers, thus demonstrating that high sensor performance is not dependent on high-resolution tunable lasers. Various optical sources and their implementation in silicon photonic sensor systems were discussed, including considerations of cost, ease of use, and ease of coupling. Two broadband sensor approaches, one using a microring resonator and the other using a Mach-Zehnder interferometer, were designed, simulated, characterized, and compared. The design of a fixed-wavelength laser architecture introduced other design considerations, including sub-wavelength grating tapers and sub-wavelength grating-assisted waveguides. The main contributions of this thesis include:

- Characterization of a broadband microring resonator sensor that included CMOS-compatible IRPHDs, including extraction of the system sensitivity, noise, and sLoD. Simulated biosensing experiments enabled comparison between the IRPHDs and traditional Ge PDs, proving the efficacy of the IRPHDs in a sensing system. Sensing experiments using isopropyl alcohol extracted a real sensitivity value of 78.9 nm/RIU and an sLoD of 9.8×10^{-4} RIU. A multiplexing system based on this approach was proposed. Overall, this design reduces the overall cost of the sensing system by eliminating the need for a tunable laser, and by enabling CMOS-compatible integration.

- Design, simulation, and measurement of a broadband Mach-Zehnder interferometer sensor, including the extraction of the system sensitivity, noise, and limit of detection. A simulated biosensing experiment using thermally-controlled MZIs was used to extract a sensitivity of 322 rad/RIU and an sLoD of 7.7×10^{-4} RIU. Compared to the MRR design, the MZI design produces a higher optical power output, which could enable use of lower-power, cheaper optical sources. However, this MZI design suffers from nonlinearity in tracking, which is dependent on the FSR to optical bandwidth ratio. If the FSR and optical bandwidth values are known, this nonlinearity can be accounted for in post-processing. Additionally, the MZI design will have a larger on-chip footprint, and requires more electrical contacts than the MRR design. Like the MRR design, this system reduces overall cost through its implementation of a broadband source. Further work is necessary to fully characterize this design.
- Design, simulation, and initial characterization of a fixed-wavelength laser sensor system that combined the sensor and tracker into a single ring. Design of this system included a comparison between the sensitivities of SWG and SWG-assisted structures and taper design for SWG waveguides. Passive optical measurements allowed for the extraction of Q-factor, which, along with simulated sensitivities, enabled the calculation of iLoDs in the 10^{-4} range. The low cost of fixed-wavelength lasers, along with their ease of integration and minimalist design, make this architecture extremely promising.

4.1 Future work

This thesis aimed to propose and demonstrate alternative approaches to tunable laser sensor designs, which can improve and enable the development of low-cost SiPh sensor systems. While the initial demonstrations of these designs are promising, there is still considerable room for their improvement, as well as additional research required prior to their implementation in a real sensing system.

4.1.1 Broadband design

The main disadvantage of the broadband design is its reliance on off-chip components, namely the broadband source and the tunable filter. While a design for an on-chip filter has been proposed and demonstrated in separate work [106], it has yet to be demonstrated in this sensor architecture. Fabrication variations could cause the filter to become off-centered, or change its bandwidth. Without a tunable laser to monitor the initial state of the filter, it may be difficult to realign it with the transmission of the sensors. Further investigation is necessary to determine the viability of this option.

On-chip integration with the broadband source should be further investigated. The broadband source used in this work was high-powered, with a flat transmission and highly stable optical power, and while cheaper than tunable lasers, it is still quite expensive. To reduce the cost of the sensor, other broadband sources should be investigated. The effect that various transmission profiles have on this sensor system will have to be researched. Furthermore, more research will need to be done to determine if these broadband sources can easily be coupled to the SiPh chip, similar to what is done for a fixed-wavelength laser. Without simple coupling integration, implementation of these designs in a real sensing platform will be difficult.

Finally, the MZI version of this system requires further investigation to fully characterize it. The tradeoff between increasing the path length difference to create smaller FSRs (to obtain more linear tracking) and lowering the fringe visibility should be investigated further. The relationship between the sensitivity for this design versus the sensitivity of a single MZI design also requires further study.

4.1.2 Fixed-wavelength laser design

While simulation and initial results were discussed for this design, it is still in the preliminary stage of development, as no experimental data has confirmed the sensitivity of the design, nor the viability of the IRPHD detection readout in this system. Further experimental investigations will be necessary to fully characterize the performance of the sensor. Additionally, further investigation is required to assess the impact fabrication variations have on this design, in particular, their

impact on the critical coupling condition of the ring.

Further work would also be required to realize a multiplexed version of this system. The PWB approach to integrate fixed-wavelength lasers is promising as it can allow multiple lasers to be easily coupled to the same chip. However, there will likely be packaging space considerations that will ultimately limit the number of devices. Additional research is required to better understand how many sensors can be monitored using a single laser. The input power of such a laser will be split between devices, which will reduce the signal; the minimum detectable signal will ultimately limit the number of sensors that can be integrated using a single laser.

4.1.3 Overall design considerations

The packaging of SiPh sensor devices is a key area of development. While the SiPh chips can be rapidly produced at high volume, current packaging techniques require careful, manual alignment of some components, including the microfluidics and PWB integration. Without automated processes for integrating such components, the overall cost of production of these sensors will be increased. Further research is required to determine how these processes can be improved.

Finally, microfluidics and electronics integration should be further investigated. The microfluidics used in this work were controlled by a fluidic pump, which could inhibit the widespread implementation of these devices due to their large size. Integration with digital microfluidics is a promising option that can be explored to reduce system size and cost. This will also require more electronics control. In this work, all electronic elements were controlled by off-chip equipment. To realize a fully packaged sensor, however, all electronics will need to be on-chip, with a single CMOS electronics chip to control and measure both the sensor, the microfluidics, and the laser. Integration of all these components is necessary to provide a fully packaged, cost-effective, silicon photonics sensor platform.

Bibliography

- [1] M Mascini and S Tombelli. Biosensors for biomarkers in medical diagnostics. Biomarkers, 13(7-8):637–657, 2008. → page 1
- [2] Atam P Dhawan, William J Heetderks, Misha Pavel, Soumyadipta Acharya, Metin Akay, Anurag Mairal, Bruce Wheeler, Clifford C Dacso, T Sunder, Nigel Lovell, et al. Current and future challenges in point-of-care technologies: a paradigm-shift in affordable global healthcare with personalized and preventive medicine. IEEE journal of translational engineering in health and medicine, 3:1–10, 2015. → page 1
- [3] Paul Yager, Gonzalo J Domingo, and John Gerdes. Point-of-care diagnostics for global health. Annual review of biomedical engineering, 10, 2008. → page 1
- [4] Yosra A Helmy, Mohamed Fawzy, Ahmed Elawad, Ahmed Sobieh, Scott P Kenney, and Awad A Shehata. The covid-19 pandemic: a comprehensive review of taxonomy, genetics, epidemiology, diagnosis, treatment, and control. Journal of clinical medicine, 9(4):1225, 2020. → page 1
- [5] Jessica Patton. Ontario reports 1,553 new coronavirus cases, 15 more deaths. Global News, 2021. URL <https://globalnews.ca/news/7704063/ontario-covid-19-coronavirus-march-18/>. → page 1
- [6] Richard Southern. Cost of administering covid-19 tests to ontario taxpayers revealed. CityNews, 2020. URL <https://toronto.citynews.ca/2020/09/30/680-news-ontario-pharmacies-testing-reimburse-covid-money/>. → page 1
- [7] Government of Canada. Coronavirus disease 2019 (covid-19): Epidemiology update, 2021. URL <https://health-infobase.canada.ca/covid-19/epidemiological-summary-covid-19-cases.html>. → page 1
- [8] MarketsandMarkets. Biosensors market by type (sensor patch and embedded device), product (wearable and nonwearable), technology

(electrochemical and optical), application (poc, home diagnostics, research lab, food & beverages), and geography - global forecast to 2024, 2019. URL <https://www.marketsandmarkets.com/Market-Reports/biosensors-market-798.html>. → page 2

- [9] Grand View Research. Biosensors market size, share & trends analysis report by application (medical, agriculture, bioreactor) by technology (thermal, electrochemical, optical), by end use, by region, and segment forecasts, 2020 - 2027, 2020. URL <https://www.grandviewresearch.com/industry-analysis/biosensors-market>. → page 2
- [10] Biacore life sciences. URL <https://www.biacore.com/lifesciences/index.html>. → page 2
- [11] Genalyte. Modernizing diagnostics. URL <https://www.genalyte.com/>. → page 2
- [12] SiDx. Modernizing blood testing. URL <https://www.sidx.com/>. → page 2
- [13] SiPhox. A new era of biosensing with photonic integrated circuits. URL <https://siphox.com/>. → page 2
- [14] Jiří Homola, Sinclair S Yee, and Günter Gauglitz. Surface plasmon resonance sensors. Sensors and actuators B: Chemical, 54(1-2):3–15, 1999. → pages 2, 11
- [15] Dorin Harpaz, Brescia Koh, Robert S Marks, Raymond Seet, Ibrahim Abdulhalim, and Alfred IY Tok. Point-of-care surface plasmon resonance biosensor for stroke biomarkers nt-probnp and s100 β using a functionalized gold chip with specific antibody. Sensors, 19(11):2533, 2019. → page 2
- [16] Xiaogang Qiang, Xiaoqi Zhou, Jianwei Wang, Callum M Wilkes, Thomas Loke, Sean O’Gara, Laurent Kling, Graham D Marshall, Raffaele Santagati, Timothy C Ralph, et al. Large-scale silicon quantum photonics implementing arbitrary two-qubit processing. Nature photonics, 12(9):534–539, 2018. → page 2
- [17] Piotr Roztocki, Michael Kues, Christian Reimer, Benjamin Wetzel, Stefania Sciara, Yanbing Zhang, Alfonso Cino, Brent E Little, Sai T Chu, David J Moss, et al. Practical system for the generation of pulsed quantum frequency combs. Optics Express, 25(16):18940–18949, 2017. → page 2

- [18] Weiqiang Xie, Tin Komljenovic, Jinxi Huang, Minh Tran, Michael Davenport, Alfredo Torres, Paolo Pintus, and John Bowers. Heterogeneous silicon photonics sensing for autonomous cars. Optics express, 27(3):3642–3663, 2019. → page 2
- [19] Christopher V Poulton, Ami Yaacobi, David B Cole, Matthew J Byrd, Manan Raval, Diedrik Vermeulen, and Michael R Watts. Coherent solid-state lidar with silicon photonic optical phased arrays. Optics letters, 42(20):4091–4094, 2017. → page 2
- [20] Sahba Talebi Fard, Samantha M Grist, Valentina Donzella, Shon A Schmidt, Jonas Flueckiger, Xu Wang, Wei Shi, Andrew Millspaugh, Mitchell Webb, Daniel M Ratner, et al. Label-free silicon photonic biosensors for use in clinical diagnostics. In Silicon Photonics VIII, volume 8629, page 862909. International Society for Optics and Photonics, 2013. → page 2
- [21] Enxiao Luan, Han Yun, Minglei Ma, Daniel M Ratner, Karen C Cheung, and Lukas Chrostowski. Label-free biosensing with a multi-box sub-wavelength phase-shifted bragg grating waveguide. Biomedical optics express, 10(9):4825–4838, 2019. → page 2
- [22] Richard Soref. The past, present, and future of silicon photonics. IEEE Journal of selected topics in quantum electronics, 12(6):1678–1687, 2006. → pages 3, 19
- [23] Enxiao Luan, Hossam Shoman, Daniel M Ratner, Karen C Cheung, and Lukas Chrostowski. Silicon photonic biosensors using label-free detection. Sensors, 18(10):3519, 2018. → pages 3, 10, 11, 12, 13, 16, 33, 34, 35, 41, 48
- [24] John T Gohring, Paul S Dale, and Xudong Fan. Detection of her2 breast cancer biomarker using the opto-fluidic ring resonator biosensor. Sensors and Actuators B: Chemical, 146(1):226–230, 2010. → page 3
- [25] Swapnajit Chakravarty, Wei-Cheng Lai, Yi Zou, Harry A Drabkin, Robert M Gemmill, George R Simon, Steve H Chin, and Ray T Chen. Multiplexed specific label-free detection of nci-h358 lung cancer cell line lysates with silicon based photonic crystal microcavity biosensors. Biosensors and Bioelectronics, 43:50–55, 2013. → page 3
- [26] Ying-Jen Chen, Wei Xiang, Jochen Klucken, and Frank Vollmer. Tracking micro-optical resonances for identifying and sensing novel procaspase-3 protein marker released from cell cultures in response to toxins. Nanotechnology, 27(16):164001, 2016. → page 3

- [27] Delphine Sterlin, Alexis Mathian, Makoto Miyara, Audrey Mohr, François Anna, Laetitia Claër, Paul Quentric, Jehane Fadlallah, Hervé Devilliers, Pascale Ghillani, et al. Iga dominates the early neutralizing antibody response to sars-cov-2. Science translational medicine, 2020. → page 3
- [28] Bhalla Nikhil, Jolly Pawan, Formisano Nello, and Estrela Pedro. Introduction to biosensors. Essays in Biochemistry, 60(1):1–8, 2016. → page 3
- [29] Xudong Fan, Ian M White, Siyka I Shopova, Hongying Zhu, Jonathan D Suter, and Yuze Sun. Sensitive optical biosensors for unlabeled targets: A review. analytica chimica acta, 620(1-2):8–26, 2008. → pages 3, 4, 10, 11, 15
- [30] JL Arlett, EB Myers, and ML Roukes. Comparative advantages of mechanical biosensors. Nature nanotechnology, 6(4):203–215, 2011. → page 4
- [31] Hua Bai, Ronghui Wang, Billy Hargis, Huaguang Lu, and Yanbin Li. A spr aptasensor for detection of avian influenza virus h5n1. Sensors, 12(9):12506–12518, 2012. → page 4
- [32] Terry T Goodrich, Hye Jin Lee, and Robert M Corn. Direct detection of genomic dna by enzymatically amplified spr imaging measurements of rna microarrays. Journal of the American Chemical Society, 126(13):4086–4087, 2004. → page 4
- [33] Gizem Ertürk, Haluk Özen, M Aşkın Tümer, Bo Mattiasson, and Adil Denizli. Microcontact imprinting based surface plasmon resonance (spr) biosensor for real-time and ultrasensitive detection of prostate specific antigen (psa) from clinical samples. Sensors and Actuators B: Chemical, 224:823–832, 2016. → page 4
- [34] Yixian Wang, Zunzhong Ye, Chengyan Si, and Yibin Ying. Subtractive inhibition assay for the detection of e. coli o157: H7 using surface plasmon resonance. Sensors, 11(3):2728–2739, 2011. → page 4
- [35] Yinqiang Xia, Rongxin Su, Renliang Huang, Li Ding, Libing Wang, Wei Qi, and Zhimin He. Design of elution strategy for simultaneous detection of chloramphenicol and gentamicin in complex samples using surface plasmon resonance. Biosensors and Bioelectronics, 92:266–272, 2017. → page 4
- [36] Jie Xu, David Suarez, and David S Gottfried. Detection of avian influenza virus using an interferometric biosensor. Analytical and bioanalytical chemistry, 389(4):1193–1199, 2007. → page 4

- [37] Abraham J Qavi and Ryan C Bailey. Multiplexed detection and label-free quantitation of micrnas using arrays of silicon photonic microring resonators. Angewandte Chemie International Edition, 49(27):4608–4611, 2010. → page 4
- [38] Adam L Washburn, Matthew S Luchansky, Adrienne L Bowman, and Ryan C Bailey. Quantitative, label-free detection of five protein biomarkers using multiplexed arrays of silicon photonic microring resonators. Analytical chemistry, 82(1):69–72, 2010. → page 4
- [39] S Janz, D-X Xu, M Vachon, N Sabourin, P Cheben, H McIntosh, H Ding, S Wang, JH Schmid, A Delâge, et al. Photonic wire biosensor microarray chip and instrumentation with application to serotyping of escherichia coliisolates. Optics express, 21(4):4623–4637, 2013. → page 4
- [40] Hai Yan, Chun-Ju Yang, Naimei Tang, Yi Zou, Swapnajit Chakravarty, Amanda Roth, and Ray T Chen. Specific detection of antibiotics by silicon-on-chip photonic crystal biosensor arrays. IEEE Sensors Journal, 17(18): 5915–5919, 2017. → page 4
- [41] Soeren Schumacher, Jörg Nestler, Thomas Otto, Michael Wegener, Eva Ehrentreich-Förster, Dirk Michel, Kai Wunderlich, Silke Palzer, Kai Sohn, Achim Weber, et al. Highly-integrated lab-on-chip system for point-of-care multiparameter analysis. Lab on a Chip, 12(3):464–473, 2012. → page 5
- [42] Haisheng Rong, Ansheng Liu, Richard Jones, Oded Cohen, Dani Hak, Remus Nicolaescu, Alexander Fang, and Mario Paniccia. An all-silicon raman laser. Nature, 433(7023):292–294, 2005. → page 5
- [43] Rodolfo E Camacho-Aguilera, Yan Cai, Neil Patel, Jonathan T Bessette, Marco Romagnoli, Lionel C Kimerling, and Jurgen Michel. An electrically pumped germanium laser. Optics express, 20(10):11316–11320, 2012. → page 5
- [44] Hui Yu, Dietmar Korn, Marianna Pantouvaki, Joris Van Campenhout, Katarzyna Komorowska, Peter Verheyen, Guy Lepage, Philippe Absil, David Hillerkuss, Luca Alloatti, et al. Using carrier-depletion silicon modulators for optical power monitoring. Optics letters, 37(22):4681–4683, 2012. → page 5
- [45] Monireh Moayedi Pour Fard, Christopher Williams, Glenn Cowan, and Odile Liboiron-Ladouceur. High-speed grating-assisted all-silicon photode-

tectors for 850 nm applications. Optics express, 25(5):5107–5118, 2017. → page 5

- [46] Jurgen Michel, Jifeng Liu, and Lionel C Kimerling. High-performance ge-on-si photodetectors. Nature photonics, 4(8):527–534, 2010. → pages 5, 51
- [47] Guoliang Li, Ying Luo, Xuezhe Zheng, Gianlorenzo Masini, Attila Mekis, Subal Sahni, Hiren Thacker, Jin Yao, Ivan Shubin, Kannan Raj, et al. Improving cmos-compatible germanium photodetectors. Optics express, 20(24):26345–26350, 2012.
- [48] MW Geis, SJ Spector, ME Grein, RT Schulein, JU Yoon, DM Lennon, S Deneault, F Gan, FX Kaertner, and TM Lyszczarz. Cmos-compatible all-si high-speed waveguide photodiodes with high responsivity in near-infrared communication band. IEEE Photonics Technology Letters, 19(3):152–154, 2007. → page 5
- [49] J Prince, B Draper, E Rapp, J Kronberg, and L Fitch. Performance of digital integrated circuit technologies at very high temperatures. IEEE Transactions on Components, Hybrids, and Manufacturing Technology, 3(4):571–579, 1980. → pages 5, 51
- [50] Hongtao Chen, P Verheyen, P De Heyn, G Lepage, J De Coster, S Balakrishnan, P Absil, W Yao, L Shen, Günther Roelkens, et al. - 1 v bias 67 ghz bandwidth si-contacted germanium waveguide pin photodetector for optical links at 56 gbps and beyond. Optics Express, 24(5):4622–4631, 2016. → page 5
- [51] Ken Giewont, Karen Nummy, Frederick A Anderson, Javier Ayala, Tymon Barwicz, Yusheng Bian, Kevin K Dezfulian, Douglas M Gill, Thomas Houghton, Shuren Hu, et al. 300-mm monolithic silicon photonics foundry technology. IEEE Journal of Selected Topics in Quantum Electronics, 25(5):1–11, 2019. → pages 5, 51
- [52] Hasitha Jayatilleka, Hossam Shoman, Lukas Chrostowski, and Sudip Shekhar. Photoconductive heaters enable control of large-scale silicon photonic ring resonator circuits. Optica, 6(1):84–91, 2019. → pages 5, 25, 27
- [53] Kuo-Kang Liu, Ren-Guei Wu, Yun-Ju Chuang, Hwa Seng Khoo, Shih-Hao Huang, and Fan-Gang Tseng. Microfluidic systems for biosensing. Sensors, 10(7):6623–6661, 2010. → page 5

- [54] David C. Duffy, J. Cooper McDonald, Olivier J. A. Schueller, and George M. Whitesides. Rapid prototyping of microfluidic systems in poly(dimethylsiloxane). *Anal. Chem.*, 70(23):4974–4984, 1998. doi:10.1021/ac980656z. URL <https://doi.org/10.1021/ac980656z>. → page 5
- [55] Yongha Hwang, Omeed H Paydar, and Robert N Candler. 3d printed molds for non-planar pdms microfluidic channels. *Sensors and Actuators A: Physical*, 226:137–142, 2015. → page 6
- [56] Thomas J Hinton, Andrew Hudson, Kira Pusch, Andrew Lee, and Adam W Feinberg. 3d printing pdms elastomer in a hydrophilic support bath via freeform reversible embedding. *ACS biomaterials science & engineering*, 2(10):1781–1786, 2016. → page 6
- [57] Enxiao Luan. Improving the performance of silicon photonic optical resonator-based sensors for biomedical applications. PhD thesis, University of British Columbia, 2020. → pages 6, 17, 31, 45, 46
- [58] Manasi Raje. A brief introduction to digital microfluidics. uFluidix, 2019. URL <https://www.ufluidix.com/circle/a-brief-introduction-to-digital-microfluidics/>. → page 6
- [59] Cristina Lerma Arce, Daan Witters, Robert Puers, Jeroen Lammertyn, and Peter Bienstman. Silicon photonic sensors incorporated in a digital microfluidic system. *Analytical and bioanalytical chemistry*, 404(10):2887–2894, 2012. → page 6
- [60] Sentayehu F Wondimu, Sebastian von der Ecken, Ralf Ahrens, Wolfgang Freude, Andreas E Guber, and Christian Koos. Integration of digital microfluidics with whispering-gallery mode sensors for label-free detection of biomolecules. *Lab on a Chip*, 17(10):1740–1748, 2017. → page 6
- [61] David S Millington, Ramakrishna Sista, Allen Eckhardt, Jeremy Rouse, Deeksha Bali, Ronald Goldberg, Michael Cotten, Rebecca Buckley, and Vamsee Pamula. Digital microfluidics: a future technology in the newborn screening laboratory? In *Seminars in perinatology*, volume 34, pages 163–169. Elsevier, 2010. → page 6
- [62] Vandana Jain, T Pravin Raj, Raghvendra Deshmukh, and Rajendra Patrikar. Design, fabrication and characterization of low cost printed circuit board based ewod device for digital microfluidics applications. *Microsystem Technologies*, 23(2):389–397, 2017.

- [63] Mohamed Abdelgawad and Aaron R Wheeler. Low-cost, rapid-prototyping of digital microfluidics devices. Microfluidics and nanofluidics, 4(4):349–355, 2008. → page 6
- [64] Carl Fredrik Carlborg, Kristinn Björgvin Gylfason, Andrzej Kaźmierczak, Fabian Dortu, MJ Banuls Polo, A Maquieira Catala, Gerhard M Kresbach, Hans Sohlström, Thomas Moh, Laurent Vivien, et al. A packaged optical slot-waveguide ring resonator sensor array for multiplex label-free assays in labs-on-chips. Lab on a Chip, 10(3):281–290, 2010. → page 6
- [65] Loic Laplatine, Enxiao Luan, Karen Cheung, Daniel M Ratner, Yonathan Dattner, and Lukas Chrostowski. System-level integration of active silicon photonic biosensors using fan-out wafer-level-packaging for low cost and multiplexed point-of-care diagnostic testing. Sensors and Actuators B: Chemical, 273:1610–1617, 2018. → page 6
- [66] Connor Mosquera. Photoconductive heater-detectors for photonic integrated circuits. PhD thesis, University of British Columbia, 2020. → pages 8, 56
- [67] Zerong Liao, Yang Zhang, Yongrui Li, Yunfei Miao, Shimeng Gao, Fankai Lin, Yulin Deng, and Lina Geng. Microfluidic chip coupled with optical biosensors for simultaneous detection of multiple analytes: A review. Biosensors and Bioelectronics, 126:697–706, 2019. → page 8
- [68] Lukas Chrostowski and Michael Hochberg. Silicon photonics design: from devices to systems. Cambridge University Press, 2015. → pages 9, 10, 15
- [69] Sanja Zlatanovic, Laura W Mirkarimi, Mihail M Sigalas, Maggie A Bynum, Edmond Chow, Karla M Robotti, Geoffrey W Burr, Sadik Esener, and Annette Grot. Photonic crystal microcavity sensor for ultracompact monitoring of reaction kinetics and protein concentration. Sensors and Actuators B: Chemical, 141(1):13–19, 2009. → page 11
- [70] Abraham J Qavi, Thomas M Mysz, and Ryan C Bailey. Isothermal discrimination of single-nucleotide polymorphisms via real-time kinetic desorption and label-free detection of dna using silicon photonic microring resonator arrays. Analytical chemistry, 83(17):6827–6833, 2011.
- [71] Shannon P Wetzler, Kali A Miller, Lydia Kisley, Alexandra LD Stanton, Paul V Braun, and Ryan C Bailey. Real-time measurement of polymer brush dynamics using silicon photonic microring resonators: Analyte partitioning and interior brush kinetics. Langmuir, 36(35):10351–10360, 2020. → page 11

- [72] Bo Liedberg, Claes Nylander, and Ingemar Lundström. Biosensing with surface plasmon resonance—how it all started. Biosensors and Bioelectronics, 10(8):i–ix, 1995. → page 11
- [73] P Cheben, DX Xu, S Janz, and A Densmore. Subwavelength waveguide grating for mode conversion and light coupling in integrated optics. Optics express, 14(11):4695–4702, 2006. → page 11
- [74] Enxiao Luan, Han Yun, Loic Laplatine, Yonathan Dattner, Daniel M Ratner, Karen C Cheung, and Lukas Chrostowski. Enhanced sensitivity of subwavelength multibox waveguide microring resonator label-free biosensors. IEEE Journal of Selected Topics in Quantum Electronics, 25(3):1–11, 2018. → page 11
- [75] Jonas Flueckiger, Shon Schmidt, Valentina Donzella, Ahmed Sherwali, Daniel M Ratner, Lukas Chrostowski, and Karen C Cheung. Subwavelength grating for enhanced ring resonator biosensor. Optics express, 24(14):15672–15686, 2016.
- [76] Hai Yan, Lijun Huang, Xiaochuan Xu, Swapnajit Chakravarty, Naimei Tang, Huiping Tian, and Ray T Chen. Unique surface sensing property and enhanced sensitivity in microring resonator biosensors based on subwavelength grating waveguides. Optics express, 24(26):29724–29733, 2016. → page 11
- [77] J Darío Sarmiento-Merenguel, Alejandro Ortega-Moñux, Jean-Marc Fédéli, J Gonzalo Wangüemert-Pérez, Carlos Alonso-Ramos, Elena Durán-Valdeiglesias, Pavel Cheben, Íñigo Molina-Fernández, and Robert Halir. Controlling leakage losses in subwavelength grating silicon metamaterial waveguides. Optics letters, 41(15):3443–3446, 2016. → page 11
- [78] M-Carmen Estevez, Mar Alvarez, and Laura M Lechuga. Integrated optical devices for lab-on-a-chip biosensing applications. Laser & Photonics Reviews, 6(4):463–487, 2012. → pages 13, 20
- [79] Stefania Dante, Daphné Duval, Borja Sepúlveda, Ana Belen González-Guerrero, José Ramón Sendra, and Laura M Lechuga. All-optical phase modulation for integrated interferometric biosensors. Optics express, 20(7):7195–7205, 2012. → pages 13, 16, 43
- [80] Wim Bogaerts, Peter De Heyn, Thomas Van Vaerenbergh, Katrien De Vos, Shankar Kumar Selvaraja, Tom Claes, Pieter Dumon, Peter Bienstman,

- Dries Van Thourhout, and Roel Baets. Silicon microring resonators. Laser & Photonics Reviews, 6(1):47–73, 2012. → page 14
- [81] Tomoyuki Yoshie, Lingling Tang, and Shu-Yu Su. Optical microcavity: sensing down to single molecules and atoms. Sensors, 11(2):1972–1991, 2011. → page 15
- [82] Lukas Chrostowski, Leanne Dias, Matthew Mitchell, Connor Mosquera, Enxiao Luan, Mohammed Al-Qadasi, Avineet Randhawa, Hassan R Mojaver, Eric Lyall, Antoine Gervais, et al. A silicon photonic evanescent-field sensor architecture using a fixed-wavelength laser. In Optical Interconnects XXI, volume 11692, page 116920W. International Society for Optics and Photonics, 2021. → pages 17, 21, 29, 33
- [83] Di Liang and John E Bowers. Recent progress in lasers on silicon. Nature photonics, 4(8):511–517, 2010. → page 19
- [84] Lawrence Cary Gunn III, Muzammil Iqbal, Brad Spaugh, and Frank Tybor. Biosensors based on optical probing and sensing, December 19 2017. US Patent 9,846,126. → page 19
- [85] Pieter Dumon, Wim Bogaerts, Dries Van Thourhout, Dirk Taillaert, Roel Baets, J Wouters, S Beckx, and P Jaenen. Compact wavelength router based on a silicon-on-insulator arrayed waveguide grating pigtailed to a fiber array. Optics Express, 14(2):664–669, 2006. → page 19
- [86] Chung-Yen Chao and L Jay Guo. Biochemical sensors based on polymer microrings with sharp asymmetrical resonance. Applied Physics Letters, 83(8):1527–1529, 2003. → page 20
- [87] Nan Jokerst, Matthew Royal, Sabarni Palit, Lin Luan, Sulochana Dhar, and Talmage Tyler. Chip scale integrated microresonator sensing systems. Journal of biophotonics, 2(4):212–226, 2009. → page 20
- [88] Xiaoyan Zhou, Lin Zhang, and Wei Pang. Performance and noise analysis of optical microresonator-based biochemical sensors using intensity detection. Optics express, 24(16):18197–18208, 2016. → page 20
- [89] Jonas Leuermann, Vladimir Stamenkovic, Patricia Ramirez-Priego, Alejandro Sánchez-Postigo, Adrián Fernández-Gavela, Cole A Chapman, Ryan C Bailey, Laura M Lechuga, Ezequiel Perez-Inestrosa, Daniel Collado, et al. Coherent silicon photonic interferometric biosensor with an inexpensive laser source for sensitive label-free immunoassays. Optics Letters, 45(24): 6595–6598, 2020. → page 20

- [90] Jiawei Wang, Zhanshi Yao, Ting Lei, and Andrew W Poon. Silicon coupled-resonator optical-waveguide-based biosensors using light-scattering pattern recognition with pixelized mode-field-intensity distributions. Scientific reports, 4(1):1–9, 2014. → page 20
- [91] Markus Knoerzer, Crispin Szydzik, Guanghui Ren, Cesar S Huertas, Sonya Palmer, Phuong Tang, Thach G Nguyen, Lam Bui, Andreas Boes, and Arnan Mitchell. Optical frequency comb based system for photonic refractive index sensor interrogation. Optics express, 27(15):21532–21545, 2019. → page 20
- [92] Paulo SS dos Santos, Pedro AS Jorge, José MMM de Almeida, and Luis Coelho. Low-cost interrogation system for long-period fiber gratings applied to remote sensing. Sensors, 19(7):1500, 2019. → page 20
- [93] Yisbel Eloisa Marin, Veronica Toccafondo, Philippe Velha, Simona Scarano, Stefano Tirelli, Alessandro Nottola, Yoonah Jeong, Hyunpyo Jeon, Sanghun Kim, Maria Minunni, et al. Silicon photonic biochemical sensor on chip based on interferometry and phase-generated-carrier demodulation. IEEE Journal of Selected Topics in Quantum Electronics, 25(1):1–9, 2018. → page 20
- [94] Xiaoyi Tian, Keith Powell, Liwei Li, Suenxin Chew, Xiaoke Yi, Linh Nguyen, and Robert Minasian. Silicon photonic microdisk sensor based on microwave photonic filtering technique. In 2019 International Topical Meeting on Microwave Photonics (MWP), pages 1–4. IEEE, 2019. → page 20
- [95] Hong Deng, Weifeng Zhang, and Jianping Yao. High-speed and high-resolution interrogation of a silicon photonic microdisk sensor based on microwave photonic filtering. Journal of Lightwave Technology, 36(19):4243–4249, 2018. → page 20
- [96] Christophe Kopp, Stephane Bernabe, Badhise Ben Bakir, Jean-Marc Fedeli, Regis Orobtcouk, Franz Schrank, Henri Porte, Lars Zimmermann, and Tolga Tekin. Silicon photonic circuits: on-cmos integration, fiber optical coupling, and packaging. IEEE Journal of selected topics in quantum electronics, 17(3):498–509, 2010. → page 21
- [97] David Thomson, Aaron Zilkie, John E Bowers, Tin Komljenovic, Graham T Reed, Laurent Vivien, Delphine Marris-Morini, Eric Cassan, Léopold Virot, Jean-Marc Fédéli, et al. Roadmap on silicon photonics. Journal of Optics, 18(7):073003, 2016. → page 21

- [98] Muhammad Rodlin Billah, Matthias Blaicher, Tobias Hoose, Philipp-Immanuel Dietrich, Pablo Marin-Palomo, Nicole Lindenmann, Aleksandar Nesic, Andreas Hofmann, Ute Troppenz, Martin Moehrle, et al. Hybrid integration of silicon photonics circuits and inp lasers by photonic wire bonding. *Optica*, 5(7):876–883, 2018. → page 21
- [99] RP Photonics Encyclopedia. Optical spectrum analyzers. URL https://www.rp-photonics.com/optical_spectrum_analyzers.html. → page 21
- [100] ThorLabs. URL https://www.thorlabs.com/newgrouppage9.cfm?objectgroup_ID=5276. → page 21
- [101] Devesh Barshilia, Lai-Kwan Chau, and Guo-En Chang. Low-cost planar waveguide-based optofluidic sensor for real-time refractive index sensing. *Optics Express*, 28(19):27337–27345, 2020. → page 22
- [102] Qingzhong Deng, Xinbai Li, Ruobing Chen, and Zhiping Zhou. Low-cost silicon photonic temperature sensor using broadband light source. In 11th International Conference on Group IV Photonics (GFP), pages 85–86. IEEE, 2014. → page 22
- [103] Junfeng Song, Xianshu Luo, Xiaoguang Tu, Mi Kyoung Park, Jack Sheng Kee, Huijuan Zhang, Mingbin Yu, Guo-Qiang Lo, and Dim-Lee Kwong. Electrical tracing-assisted dual-microring label-free optical bio/chemical sensors. *Optics express*, 20(4):4189–4197, 2012. → pages xiv, 22, 23, 25, 33
- [104] Hasitha Jayatileka, Kyle Murray, Miguel Ángel Guillén-Torres, Michael Caverley, Ricky Hu, Nicolas AF Jaeger, Lukas Chrostowski, and Sudip Shekhar. Wavelength tuning and stabilization of microring-based filters using silicon in-resonator photoconductive heaters. *Optics express*, 23(19):25084–25097, 2015. → page 26
- [105] Luxmux Technology Corporation. Multi-sled optical spectral engine. URL <https://luxmux.com/products/ASM000110>. → page 29
- [106] Mustafa Hammood, Ajay Mistry, Minglei Ma, Han Yun, Lukas Chrostowski, and Nicolas AF Jaeger. Compact, silicon-on-insulator, series-cascaded, contradirectional-coupling-based filters with 50 db adjacent channel isolation. *Optics letters*, 44(2):439–442, 2019. → pages 29, 50, 62
- [107] Yun Wang, Wei Shi, Xu Wang, Zeqin Lu, Michael Caverley, Richard Bojko, Lukas Chrostowski, and Nicolas AF Jaeger. Design of broadband subwavelength grating couplers with low back reflection. *Optics letters*, 40(20):4647–4650, 2015. → page 29

- [108] Yi Zhang, Shuyu Yang, Andy Eu-Jin Lim, Guo-Qiang Lo, Christophe Galland, Tom Baehr-Jones, and Michael Hochberg. A compact and low loss y-junction for submicron silicon waveguide. Optics express, 21(1):1310–1316, 2013. → page 31
- [109] Miguel A Guillén-Torres, Michael Caverley, Edmond Cretu, Nicolas AF Jaeger, and Lukas Chrostowski. Large-area, high-q soi ring resonators. In 2014 IEEE Photonics Conference, pages 336–337. IEEE, 2014. → page 31
- [110] Yun Wang, Minglei Ma, Han Yun, Zeqin Lu, Xu Wang, Nicolas AF Jaeger, and Lukas Chrostowski. Ultra-compact sub-wavelength grating polarization splitter-rotator for silicon-on-insulator platform. IEEE Photonics Journal, 8(6):1–9, 2016. → page 31
- [111] Safa O Kasap et al. Optoelectronics and photonics. Pearson Education UK, 2013. → page 33
- [112] Jonas Leuermann, Adrián Fernández-Gavela, Antonia Torres-Cubillo, Sergio Postigo, Alejandro Sánchez-Postigo, Laura M Lechuga, Robert Halir, and Íñigo Molina-Fernández. Optimizing the limit of detection of waveguide-based interferometric biosensor devices. Sensors, 19(17):3671, 2019. → page 33
- [113] Applied Nanotools Inc. Nanosoi fabrication service. URL <https://www.appliednt.com/nanosoi-fabrication-service/>. → page 36
- [114] John Staples. Fiber laser, michaelson interferometer, and coherence length, 2007. URL https://uspas.fnal.gov/materials/08UCSC/mml19_fiber_laser.pdf. → page 42
- [115] Prashanth R Prasad, Shankar K Selvaraja, and Manoj M Varma. Full-range detection in cascaded microring sensors using thermo-optical tuning. Journal of Lightwave Technology, 34(22):5157–5163, 2016. → page 48
- [116] Jia-Ming Liu. Principles of photonics. Cambridge University Press, 2016. → page 50
- [117] Wei Shi, Ye Tian, and Antoine Gervais. Scaling capacity of fiber-optic transmission systems via silicon photonics. Nanophotonics, 9(16):4629–4633, 2020. → page 50
- [118] Lukas Chrostowski, Hossam Shoman, Mustafa Hammood, Han Yun, Jaspreet Jhoja, Enxiao Luan, Stephen Lin, Ajay Mistry, Donald Witt, Nicolas AF Jaeger, et al. Silicon photonic circuit design using rapid prototyping

foundry process design kits. IEEE Journal of Selected Topics in Quantum Electronics, 25(5):1–26, 2019. → page 51

- [119] Yimin Kang, Han-Din Liu, Mike Morse, Mario J Paniccia, Moshe Zadka, Stas Litski, Gadi Sarid, Alexandre Pauchard, Ying-Hao Kuo, Hui-Wen Chen, et al. Monolithic germanium/silicon avalanche photodiodes with 340 ghz gain–bandwidth product. Nature photonics, 3(1):59–63, 2009. → page 51
- [120] Joseph A Curcio and Charles C Petty. The near infrared absorption spectrum of liquid water. JOSA, 41(5):302–304, 1951. → page 52
- [121] ViaLite Communications. Choice of wavelength for rf over fiber – 1310nm vs 1550nm. URL <https://www.vialite.com/resources/guides/choice-of-wavelength-for-rf-over-fiber-1310nm-vs-1550nm/>. → page 52
- [122] ML Povinelli, Steven G Johnson, and JD Joannopoulos. Slow-light, band-edge waveguides for tunable time delays. Opt. Express, 13(18):7145–7159, 2005. → page 53
- [123] Justin R Bickford, Pak Cho, Mikella Farrell, and Ellen Holthoff. Fish-bone subwavelength grating waveguide photonic integrated circuit sensor array. In Chemical, Biological, Radiological, Nuclear, and Explosives (CBRNE) Sensing XIX, volume 10629, page 1062910. International Society for Optics and Photonics, 2018. → page 53

Appendix A

EECE 584 and ELEC 581 project reports

The following pages contain course project reports for EECE 584 (Titled: Free spectral range matching for cascaded Mach Zehnder interferometer sensors) and ELEC 581 (Titled: Impact of fabrication variations on silicon photonic evanescent field sensors). These reports contain additional investigations of the effects of FSR matching and fabrication variations in low-cost sensor designs.

Free spectral range matching for cascaded Mach-Zehnder interferometer sensors

Leanne Dias

Department of Electrical and Computer Engineering, University of British Columbia,
Vancouver, Canada

1. SUMMARY

A silicon photonics sensor consisting of two cascaded Mach-Zehnder interferometers (MZIs) is investigated through simulations and experiments. This sensor design uses a broadband source, and has one MZI that acts as the sensor, with one arm exposed to analytes, while the other MZI acts as a tracker, with one thermally tunable arm. Ideally, the free spectral ranges (FSRs) of both MZIs would be designed to be identical. In this work, we demonstrate through experiment and simulation that analyte exposure and thermal tuning will shift the group indices, and thus the FSRs, of each MZI in opposite directions, causing initially matched FSRs to become misaligned. We also investigate the impact this misalignment will have on the device performance. We simulate a decrease in the extinction ratio of the detected output power, and an induced non-linearity in phase tracking when the FSRs are not matched.

2. INTRODUCTION

Integrated photonic circuits have demonstrated tremendous potential for replacing traditional systems in numerous fields. Silicon photonics, based on the silicon-on-insulator (SOI) platform, routes light on-chip through waveguides, which, due to the high contrast between refractive indices, can create extremely compact, high density devices.¹ The SOI platform is compatible with mature complementary metal-oxide semiconductor (CMOS) fabrication processes, which enables the fabrication of these devices at a very low cost at high volume.^{1,2} The commercialization of silicon photonics was initially driven by applications in the telecommunication industry, but has since demonstrated in many other fields, including quantum information processing,^{3,4} light detection and ranging (LIDAR),^{5,6} and sensors.^{7,8} Many of the components and designs that were initially used for transceiver networks can be redesigned for use in these other fields.

One such system is based on cascading on-chip components, such as micro-ring resonators^{9,10} or Mach-Zehnder interferometers (MZIs),^{11,12} to create filters for wavelength division multiplexing (WDM). In these circuits, the free spectral range (FSR) of the components are designed to create filters at specific wavelengths, allowing some wavelengths to pass, while others are suppressed. The FSRs of the cascaded components are typically offset from one another to create better filtering. This cascaded approach has since been researched and modified for use in cost-effective sensing applications.¹³⁻¹⁶ In these sensor designs, the on-chip components are once again cascaded. The sensor operates by tuning the transmission spectrum of one component to match the transmission spectrum of the other. Thus, shifts in the second transmission can be detected by monitoring the tuning power required to keep the transmissions aligned.

The FSRs in these sensors are typically designed to be matched at a specific wavelength, as a mismatch can cause complications in detection. Prasad et al.¹⁷ investigated various factors that could influence the performance of such a sensor design based on micro-ring resonators, including the impact that the quality factor of the ring and FSR mismatches, and found that both could decrease the detected extinction ratio. In this report, we aim to characterize a cascaded MZI sensor, by investigating factors that could contribute to mismatched FSRs, and simulate the impact that these mismatches could have on such a system.

3. SENSOR DESIGN

In our cascaded MZI sensor design, one MZI acts as the sensor, while the other MZI acts as a tracker, and is electrically tunable with a heater (Figure 1a). Both MZIs are unbalanced, with one arm longer than the other, to create a sinusoidal transmission, which can be more easily monitored. Broadband light is input to the sensor MZI, and the output is input to the tracker. The output can be monitored with a single photodetector. Both MZIs will have their own sinusoidal transmission (Figure 1b). The output will be the multiplication of their transmissions (Figure 1c).

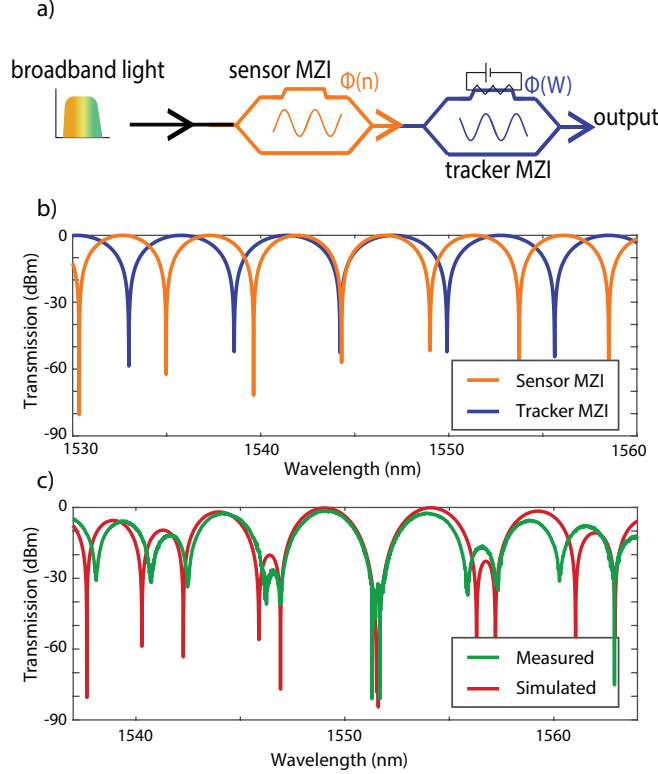


Figure 1. a) Layout of the cascaded MZI sensor. Light is coupled on-chip through grating couplers. The first MZI has one arm exposed to water. The second MZI is thermally tunable. The output is coupled off-chip with grating couplers and measured off chip. b) Simulated spectra of the sensor MZI and the tracker MZI. c) Simulated and measured (with a tunable laser) transmission of the $\Delta L = 100 \mu\text{m}$ cascaded system.

In a sensing experiment, an electrical power would be applied to the thermal tuner on the tracker MZI, and would continually be scanned. A photodetector would measure the output power through the cascaded MZI system. A high output power detected by the photodetector would indicate that the transmission spectra of the MZIs are aligned. When the water-clad sensor arm of the MZI is exposed to an analyte, the effective index of the waveguide will shift. This will create a phase shift ($\Delta\phi$) in the transmission of the sensor MZI, given by:⁷

$$\Delta\phi = \frac{2\pi}{\lambda} \Delta n_{\text{eff}} L_{\text{sens}} \quad (1)$$

where Δn_{eff} is the effective index change, λ is the wavelength, and L_{sens} is the length of the sensing arm. Now, when the electrical power on the thermal tuner of the tracker MZI is scanned, the peak output power will occur at a new electrical power applied to the thermal tuner. By measuring the shift in applied electrical power to the thermal tuner, the refractive index shift caused by the analyte can be extracted.

$L_{\text{Ref S}}$ (μm)	L_{S} (μm)	$\Delta L_{\text{S MZI}}$ (μm)	$L_{\text{Ref H}}$ (μm)	L_{H} (μm)	$\Delta L_{\text{H MZI}}$ (μm)
950	1000	50	950	1000	50
900	1000	100	900	1000	100
800	1000	200	800	1000	200
700	1000	300	700	1000	300

Table 1. Design variations for the cascaded MZI sensor. “Ref” refers to the reference arm in the MZI, and “S” and “H” refer to the sensor and heater, respectively.

Figure 2 displays the layout of the sensor as it was fabricated on chip. Spiral waveguides were used for the MZIs to try to keep the footprint of the device to a minimum. The total area of all four device variations, excluding grating couplers, was $1215 \mu\text{m} \times 440 \mu\text{m}$ (dotted line in Figure 2). The open-oxide arm of the sensor MZI was designed with $500 \mu\text{m}$ spacing from the grating coupler, in order to be able to expose it to solutions without the grating coupler interfering. This can be done by either placing droplets of solutions on the MZI, or fabricating a microfluidics channel to cover the open oxide area (the latter being the more reliable option). The tracker MZI was spaced $650 \mu\text{m}$ away from the sensor MZI in order to reduce thermal cross-talk. The electrical contact pads were placed $550 \mu\text{m}$ away from the sensor MZI so that the fluidics would not interfere with the electrical contacting, and placed $500 \mu\text{m}$ away from the grating couplers so that the electrical probes would not interfere with the grating coupler. In future designs, it is suggested to create larger spacings between the oxide-open area and the electrical contacts and grating couplers, for simpler testing.

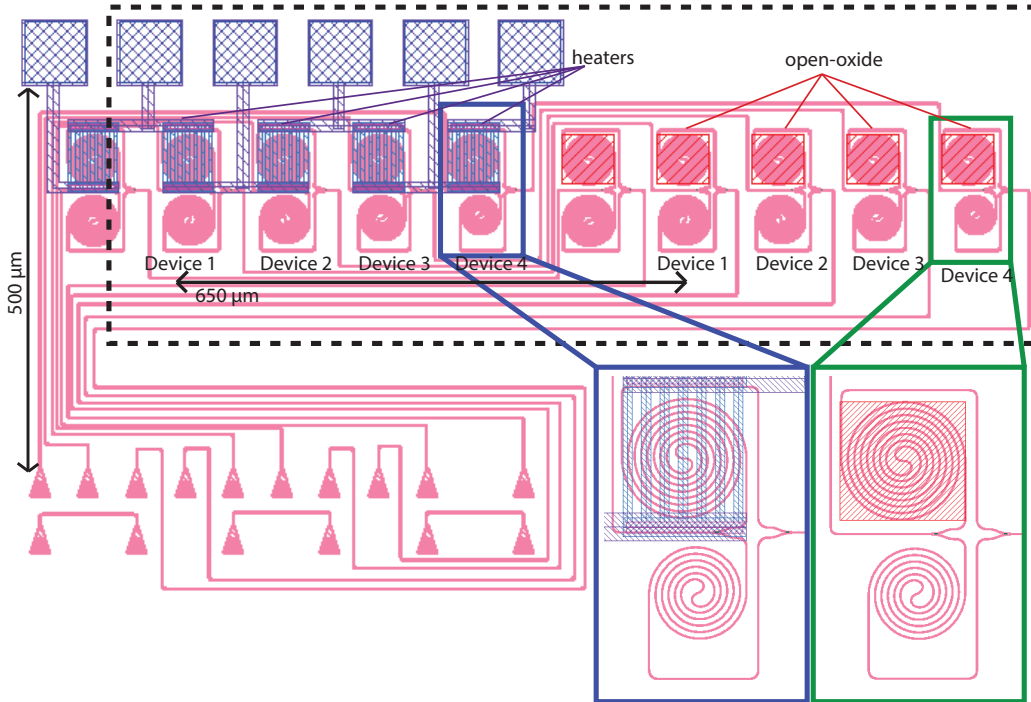


Figure 2. Layout of the cascaded sensor design, with close up insets of the tracker and sensor MZIs. Each set of devices is labelled with their matching sensor and tracker (trackers on the left, with sensors on the right). The distance between sensor and tracker is $650 \mu\text{m}$, and the distance between grating couplers and electrical contact pads is $500 \mu\text{m}$.

There are four variations of the design, as summarized in Table 1. The arm lengths of the sensor and tracker MZIs that are exposed to phase shifts were kept at a constant length, while the reference arms, buried in oxide, had varying lengths. The difference in path lengths of the sensor and tracker MZI were equivalent in each device, respectively.

4. GROUP INDEX VARIATIONS

Ideally, the transmission spectra of the two MZIs would be identical, and the FSRs would match perfectly. The FSR for an MZI is given by:¹⁸

$$\text{FSR} = \frac{\lambda^2}{L_1 n_{g1} - L_2 n_{g2}} \quad (2)$$

where λ is the wavelength, L_1 and L_2 are the lengths of the two MZI arms, and n_{g1} and n_{g2} are the group indices of the two MZI arms, respectively. If the FSRs were matched and the transmission spectra were aligned, the output from the cascaded system would look like a single MZI transmission. Unfortunately, our designs were not matched, as is visible in Figure 1c (for a ΔL of 100 μm). Our designs were fabricated with identical arms lengths for both the sensor MZI and the tracker MZI. However, the group indices of these MZIs are different because of their different cladding materials. One of the arms in the sensor MZI is exposed to water, which gives it a group index of ~ 4.28 RIU (at 1550 nm wavelength), while both arms of the tracker MZI have an oxide cladding (group index of ~ 4.24 RIU at 1550 nm wavelength). The FSR mismatches in our designs are summarized in Table 2.

ΔL (μm)	$\text{FSR}_{\text{heater}}$ (nm)	$\text{FSR}_{\text{sensor}}$ (nm)	Deviation (%)
50	11.34	10.26	10.6
100	5.67	5.38	5.3
200	2.83	2.76	2.6
300	1.89	1.86	1.8

Table 2. FSR mismatches for the fabricated devices. Mismatches are less apparent for larger arm imbalances.

The arm lengths of the MZIs can be designed to compensate for the mismatch in the group index of the MZIs. However, group index (n_g) is wavelength (λ) dependent, given by:¹⁸

$$n_g(\lambda) = n_{\text{eff}}(\lambda) - \lambda \frac{dn_{\text{eff}}}{d\lambda} \quad (3)$$

where n_{eff} is the effective index, which is also a function of wavelength. Because the sensor and tracker arms have different claddings, they will also have different effective indices, and different dependencies on wavelength. Tuning the arm lengths to match the FSRs at a specific wavelength does not guarantee matching at across all wavelengths. Table 3 shows the arm length differences for the sensor and tracker to have matched FSRs at 1550 nm wavelength (and $L_{\text{sens}} = 500 \mu\text{m}$), and shows the percent deviation of the FSRs at 1535 nm wavelength. The calculated deviation is quite small (0.4% in the worst case); however, this is for the nominal design case, where no refractive index shifts have occurred in the sensor or tracker MZI. Exposure to an analyte or thermal tuning of the effective index will also effect the group index, which will be discussed further.

ΔL_{sensor} (μm)	ΔL_{heater} (μm)	$\text{FSR}_{\text{sensor}}$ (nm)	$\text{FSR}_{\text{heater}}$ (nm)	Deviation (%)
50	55.3	10.11	10.07	0.4
100	105.3	5.296	5.285	0.2
200	205.3	2.713	2.710	0.1
300	305.3	1.824	1.822	0.07

Table 3. FSR mismatches at wavelengths for which the arm lengths were not designed to be matched. In this case, the heater arm was modified to match the sensor FSR at 1550 nm. At 1535 nm, we start to see slight deviations from the FSR matching.

The group index can be extracted from the measured data by measuring the FSR at various wavelengths (1550 nm and 1535 nm, in our case), and using Equation 2 to calculate n_g . Figure 3a shows the measured output transmission (of the $\Delta L = 300 \mu\text{m}$ MZI) at two different voltages. From this, we can measure the FSRs (labelled) at 1535 nm and 1550 nm for each voltage. The group index dependence on applied power can then be extracted by repeating this measurement across various voltages. Figure 3b displays the extracted and simulated group index versus applied power. While there is some deviation between the measured and simulated values, the trends are fairly similar, and the difference may arise due to fabrication variations, or variations between the simulated and fabricated heaters.

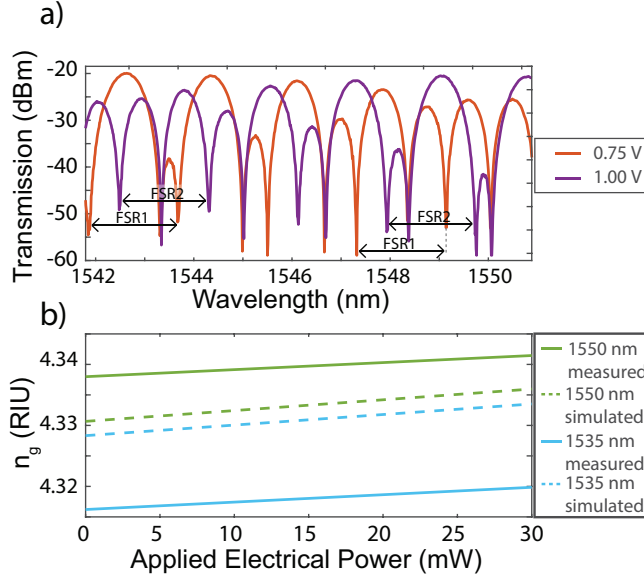


Figure 3. a) Measured (with a tunable laser) optical transmission of the $\Delta L = 300 \mu\text{m}$ design at 0.75 V and 1.00 V. The FSRs of the tracker MZI at two different wavelengths are marked on each. b) Simulated and measured group index as a function of voltage at 1550 nm and 1535 nm.

The expected change in effective index due to the applied power was also extracted by simulating the temperature profile of the waveguide using Lumerical’s HEAT, and importing that temperature map into Lumerical’s MODE to extract the effective index, at various applied biases. Across a 30 mW applied power, a change in effective index of 4.08×10^{-3} RIU was extracted. This change in effective index can then be converted to change in refractive index of the cladding for the sensor MZI arm, using a waveguide mode sensitivity⁷ of 0.151 RIU/RIU. The change in cladding refractive index was calculated to be 0.027 RIU.

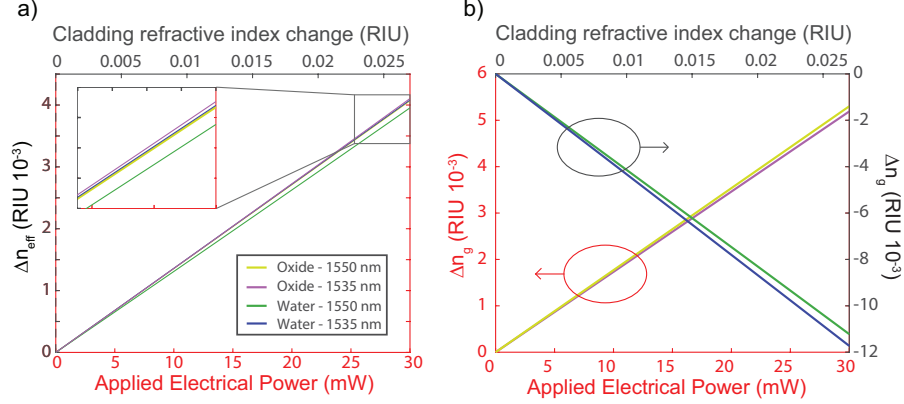


Figure 4. a) Simulated change in effective index for the oxide-clad and water-clad waveguides, as a function of applied power and cladding refractive index, respectively, for wavelengths at 1550 nm and 1535 nm. Here, we see the oxide and water results match well. b) Simulated change in group index for the oxide-clad and water-clad waveguides, as a function of applied power and cladding refractive index, respectively, for wavelengths at 1550 nm and 1535 nm. Here, we see a large deviation between the oxide-clad and water-clad waveguide group indices.

Lumerical's MODE was once again used to simulated the change in effective index of the sensor MZI arm over a 0.027 RIU change in the cladding. In Figure 4a, we see that the change in effective index between the sensor and the tracker match very well, meaning that a phase induced in one MZI can be matched well in the other. However, although the phase shifts are matched, the group indices will not be. The mode solvers were also used to extract the group index across the same range of powers/RIU shifts. In Figure 4b, we see that the change in group index of the oxide-clad waveguide has a positive slope, while the change in group index of the water-clad waveguide has a negative trend, with a slope almost a two times larger in magnitude than the oxide-clad waveguide. Here, we see that even if the FSRs of the sensor and tracker MZIs were initially matched, they would become unmatched in a sensor-tracker experiment due to uneven changes in the group indices.

5. FREE SPECTRAL RANGE VARIATIONS

As we have seen experimentally in the previous section, there will be some FSR mismatch between the sensor and tracker MZI, due to the group index variations across wavelengths or variations that arise when the sensor is exposed to an analyte, even when the MZIs are designed and fabricated perfectly. Here, we aim to simulate the impact this mismatch will have on the device performance.

Because the group index varies across wavelengths, we will filter the broadband to only use a bandwidth over a small range of wavelengths, since the variations should not be large over a small range. The expected output power can therefore be modelled as the integration of two sinusoidal functions multiplied:

$$\int_a^b \sin^2(\phi - k) \times \sin^2(h(\phi - j)) d\phi \quad (4)$$

where $\sin^2(\phi - k)$ and $\sin^2(h(\phi - j))$ describe the transmission of the sensor and tracker MZI with phase shift k and j , respectively, and a and b describe the optical filter bandwidth. The sinusoidal-squared functions nominally have a period of π ; however, here, we introduce a change in the period of the tracker MZI with the factor of h . We can then integrate over 1, 2, 3, and 10 FSRs for various percent deviations in the period (\sim FSR). The results are displayed in Figure 5. In the ideal case with 0% deviation, we see an extinction ratio of ~ 0.6 . However, as the deviation is increased, the extinction ratio gets smaller, eventually to where it is zero. Furthermore, we see

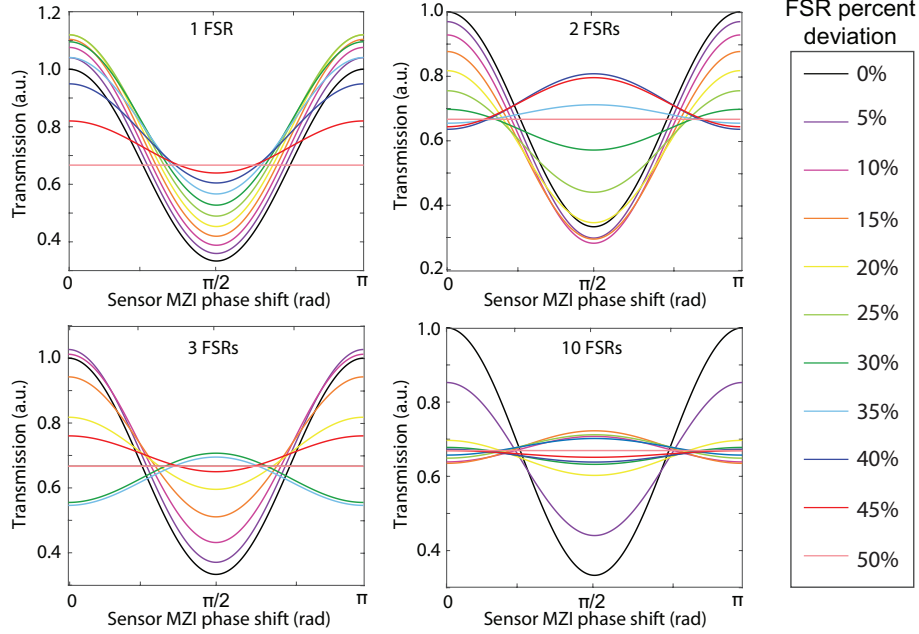


Figure 5. Output optical power through the cascaded system by integrating over 1, 2, 3, and 10 FSRs, as a function of sensor MZI phase shift, for various FSR mismatches. Here, we would like a large extinction ratio, as in the 0% deviation case.

that as more FSRs are included in the integration, the transmission (output power measured) can actually change signs, where the peak power is no longer when there is zero phase shift between transmissions, but rather occurs when the transmission spectra are out of phase. In the 10 FSR case, any deviations greater than $\sim 5\text{-}10\%$ results in quite low extinction ratios (~ 0.1). Conversely, in the 1 FSR case, deviations up to 40% still produce ~ 0.3 extinction ratio. Even with large FSR deviations, using an optical bandwidth over a single FSR can still produce decent results.

Unfortunately, the mismatch in FSR effects more than just the extinction ratio. It also effects the output power measured across different sensor MZI phase shifts. In Figure 6a, we plot the measured output power (measured over 1 FSR bandwidth) versus the phase shift in the sensor MZI for various phase shifts in the tracker MZI, and for 0% and 10% FSR deviations. In the case where the FSRs are matched, we see that the peak output power remains constant (black solid line). In the 10% deviation case, we can see that the output power changes depending on the phase shift (black dotted line). This measurement was repeated for deviations up to 50%, as shown in Figure 6b. Here, we see that the power difference have the greatest variation around 30% FSR mismatch.

Finally, we also see that the FSR mismatches causes non-linearity in tracking the phase shift of the sensor MZI. Figure 6c displays the tracker MZI phase shift required to obtain peak output power as a function of sensor MZI phase shift. Ideally, a phase shift in the sensor MZI would be matched with an equal phase shift in the tracker MZI (linear line, shown in black for 0% deviation). However, as the FSR mismatch becomes larger, we can see larger deviations from this linearity (coloured lines, labelled in the legend). In cases where the FSRs are not matched, a phase shift measured by the tracker MZI will not be equal to the phase shift in the sensor MZI. In order to properly track the phase shift in the sensor, the mismatch between the FSRs must be known prior to sensing measurements.

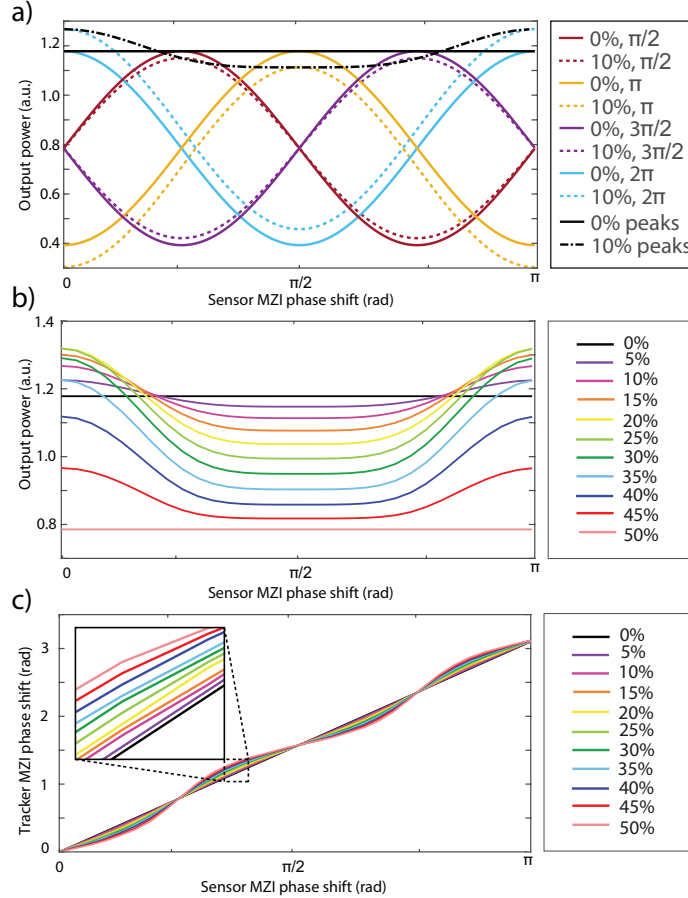


Figure 6. a) Output power as a function of sensor MZI phase shift, for various tracker phase shifts, and for FSR mismatches of 0% and 10%, as labelled in the legend. The black lines indicate the trend for the peak powers, and are used to create: b) The peak output power as a function of sensor MZI phase shift, for various FSR mismatches. c) Tracker MZI phase shift for peak output power as a function of sensor MZI phase shift, for various FSR mismatches. Ideally, the trends would be linear, as shown by the 0% line.

6. CONCLUSION

In this report, we characterized a silicon photonics cascaded MZI design for applications in sensing. The group index of an oxide-clad waveguide was simulated and extracted from fabricated designs. The group index of a water-clad waveguide was also simulated. Over the same shift in effective index, the oxide-clad and water-clad waveguide experience different changes in group index, which would cause the FSRs to become misaligned. An investigation into the impact of this misalignment was also performed. When the FSRs of the cascaded MZIs are not matched, the extinction ratio and linearity of phase tracking decreases. Ideally, the cascaded MZI sensor device should be designed to initially have matched FSRs. If the optical bandwidth of the source matches the FSR of the MZI, changes in group index should not greatly effect the extinction ratio, although some non-linearity will still exist in the phase tracking.

REFERENCES

- [1] Bogaerts, W. and Chrostowski, L., "Silicon photonics circuit design: methods, tools and challenges," *Laser & Photonics Reviews* **12**(4), 1700237 (2018).
- [2] Soref, R., "The past, present, and future of silicon photonics," *IEEE Journal of selected topics in quantum electronics* **12**(6), 1678–1687 (2006).

- [3] Carolan, J., Harrold, C., Sparrow, C., Martín-López, E., Russell, N. J., Silverstone, J. W., Shadbolt, P. J., Matsuda, N., Oguma, M., Itoh, M., et al., “Universal linear optics,” *Science* **349**(6249), 711–716 (2015).
- [4] Qiang, X., Zhou, X., Wang, J., Wilkes, C. M., Loke, T., O’Gara, S., Kling, L., Marshall, G. D., Santagati, R., Ralph, T. C., et al., “Large-scale silicon quantum photonics implementing arbitrary two-qubit processing,” *Nature photonics* **12**(9), 534–539 (2018).
- [5] Poulton, C. V., Yaacobi, A., Cole, D. B., Byrd, M. J., Raval, M., Vermeulen, D., and Watts, M. R., “Coherent solid-state lidar with silicon photonic optical phased arrays,” *Optics letters* **42**(20), 4091–4094 (2017).
- [6] Miller, S. A., Chang, Y.-C., Phare, C. T., Shin, M. C., Zadka, M., Roberts, S. P., Stern, B., Ji, X., Mohanty, A., Gordillo, O. A. J., et al., “Large-scale optical phased array using a low-power multi-pass silicon photonic platform,” *Optica* **7**(1), 3–6 (2020).
- [7] Luan, E., Shoman, H., Ratner, D. M., Cheung, K. C., and Chrostowski, L., “Silicon photonic biosensors using label-free detection,” *Sensors* **18**(10), 3519 (2018).
- [8] Fard, S. T., Grist, S. M., Donzella, V., Schmidt, S. A., Flueckiger, J., Wang, X., Shi, W., Millspaugh, A., Webb, M., Ratner, D. M., et al., “Label-free silicon photonic biosensors for use in clinical diagnostics,” in [*Silicon Photonics VIII*], **8629**, 862909, International Society for Optics and Photonics (2013).
- [9] Zhou, L., Zhang, X., Lu, L., and Chen, J., “Tunable vernier microring optical filters with *p-i-p*-type microheaters,” *IEEE Photonics Journal* **5**(4), 6601211–6601211 (2013).
- [10] Manganelli, C., Pintus, P., Gambini, F., Fowler, D., Fournier, M., Faralli, S., Kopp, C., and Oton, C., “Large-fsr thermally tunable double-ring filters for wdm applications in silicon photonics,” *IEEE Photonics Journal* **9**(1), 1–10 (2017).
- [11] Horst, F., Green, W. M., Assefa, S., Shank, S. M., Vlasov, Y. A., and Offrein, B. J., “Cascaded mach-zehnder wavelength filters in silicon photonics for low loss and flat pass-band wdm (de-) multiplexing,” *Optics express* **21**(10), 11652–11658 (2013).
- [12] Ovvyan, A., Gruhler, N., Ferrari, S., and Pernice, W., “Cascaded mach-zehnder interferometer tunable filters,” *Journal of Optics* **18**(6), 064011 (2016).
- [13] Song, J., Luo, X., Tu, X., Park, M. K., Kee, J. S., Zhang, H., Yu, M., Lo, G.-Q., and Kwong, D.-L., “Electrical tracing-assisted dual-microring label-free optical bio/chemical sensors,” *Optics express* **20**(4), 4189–4197 (2012).
- [14] Dai, D. and He, S., “Highly-sensitive sensor with large measurement range realized with two cascaded-microring resonators,” *Optics communications* **279**(1), 89–93 (2007).
- [15] Kim, H.-T. and Yu, M., “Cascaded ring resonator-based temperature sensor with simultaneously enhanced sensitivity and range,” *Optics Express* **24**(9), 9501–9510 (2016).
- [16] Shao, L.-Y., Luo, Y., Zhang, Z., Zou, X., Luo, B., Pan, W., and Yan, L., “Sensitivity-enhanced temperature sensor with cascaded fiber optic sagnac interferometers based on vernier-effect,” *Optics Communications* **336**, 73–76 (2015).
- [17] Prasad, P. R., Selvaraja, S. K., and Varma, M. M., “Full-range detection in cascaded microring sensors using thermo-optical tuning,” *Journal of Lightwave Technology* **34**(22), 5157–5163 (2016).
- [18] Chrostowski, L. and Hochberg, M., [*Silicon photonics design: from devices to systems*], Cambridge University Press (2015).

Impact of fabrication variations on silicon photonic evanescent-field sensors

Leanne Dias

Electrical and Computer Engineering, University of British Columbia, Vancouver, Canada

1. SUMMARY

Silicon photonic sensors show potential in global healthcare, however, they suffer from manufacturing challenges, which can lead to variability in device performance. In this report, we simulate fabrication variations in the waveguide mode sensitivity and phase shifter efficiency, and analyze their effect on the overall sensor performance. Variations in the waveguide mode sensitivity were analyzed by varying the waveguide width and height, while variations in the phase shifter efficiency were extracted by varying the dopant concentrations. Here, we propose a sensor system using both components, and demonstrate the possible false interpretation of results if fabrication variations are not addressed.

2. INTRODUCTION

Miniaturized biosensing devices are crucial for the advancement of global healthcare as they offer fast, reliable, and affordable detection.^{1,2} Services that are typically performed in a lab can be combined into a single compact device, reducing the required sample size and lowering the cost of materials. Silicon-based photonic sensors can perform real-time measurements, which can accelerate the diagnosis process and allow for earlier treatment.³ These silicon photonic devices have been shown to detect diseases, viruses, and pathogens, including biomarkers for breast and lung cancer,^{4,5} neurodegenerative disorders,⁶ and SARS-CoV-2.⁷ Additionally, these sensors are compatible with the complementary metal-oxide-semiconductor (CMOS) fabrication processes, which can be leveraged to produce silicon photonic sensors at a very low cost.⁸

While silicon photonic sensors can be made for low-cost, the total cost of the sensing system remains quite high, due to their reliance on high-resolution tunable lasers. There has been a push towards lower cost optical sources, including using fixed-wavelength lasers and broadband sources.⁹⁻¹⁵ Some of these designs rely on extracting the refractive index shift of the sensor using an electronic readout, rather than directly measuring optical transmission shifts. Rather than scanning the laser wavelength to extract the sensor transmission spectrum, these methods typically use a tuning element to shift the transmission of the sensor and track where the photodetector output is maximized. By tracking the change in electrical power applied to the tuning element, the shift in the sensor refractive index can be extracted. This assumes a precise knowledge of the effect that applied electrical power has on the refractive index.

However, silicon photonic circuits suffer from variations in manufacturing,¹⁶ which leads to uncertainties in their design metrics. Fabrication errors in the waveguide geometries effect the propagation of light in the waveguide. While these errors can differ from wafer to wafer, then can also occur across a single wafer. These variations can be somewhat difficult to determine, as they either require the use of characterization equipment, such as scanning electron microscopy (SEM) or atomic force microscopy (AFM),¹⁷ or additional on-chip test circuits across the wafer, which, for a sensor system, is not very practical. While some studies have demonstrated methods to predict the performance of silicon photonic circuits with manufacturing errors,^{18,19} studies have not been specifically performed for silicon photonic sensors. In this paper, we simulate fabrication variations on several sensor components, and use these results to simulate the resultant performance of a low-cost silicon photonic sensor design.

3. OPERATING PRINCIPLES

In this section, we provide a brief overview of some of the components used in silicon photonic sensors. We also introduce the basic operating principles of our low-cost sensor architecture.

3.1 Sensitivity in silicon photonics MZI sensors

In our proposed sensor system, we will use a Mach-Zehnder interferometer (MZI) as our sensor component. Here, the input light is split into two waveguide paths, where one path is exposed to the sample (L_{sens}), and the other is our phase shifter (L_{ps}). The light from the two arms is then recombined. When there is no phase difference between the arms, constructive interference occurs at the output. However, as a phase shift is introduced (either from exposure to the sample in the sensor arm, or a bias in the phase shifter), the light will no longer be in phase, and destructive interference will occur. The phase shift ($\Delta\phi$) due to exposure to a sample (assuming the phase shifter arm is constant) can be related to the change in effective index (Δn_{eff}) at a given wavelength (λ) by:²⁰

$$\Delta\phi = \frac{2\pi}{\lambda} \Delta n_{\text{eff}} L_{\text{sens}} \quad (1)$$

where L_{sens} is the length of the arm.

Silicon photonic sensors are often characterized by their sensitivity performance, which quantifies the strength of the sensor response when exposed to an analyte. For an MZI sensor, sensitivity (S_{MZI}) is often measured in rad/RIU (refractive index units), and is given by:²⁰

$$S_{\text{MZI}} = \frac{2\pi L_{\text{sens}}}{\lambda} \left(\frac{\delta n_{\text{eff}}}{\delta n_{\text{clad}}} \right) = \frac{\Delta\phi}{\Delta n_{\text{eff}}} \left(\frac{\delta n_{\text{eff}}}{\delta n_{\text{clad}}} \right) \quad (2)$$

where $\left(\frac{\delta n_{\text{eff}}}{\delta n_{\text{clad}}} \right)$ is the waveguide mode sensitivity. The waveguide mode sensitivity describes how the effective index of the waveguide will change due to a change in the refractive index of the cladding. It is independent of the sensor component (i.e., the MZI), and is based on the geometry of the waveguide. Therefore, as we will see in sections below, the waveguide mode sensitivity is highly dependent on the width and height of the waveguide.

3.2 Phase shifters in silicon photonics sensors

A second component needed for a low-cost silicon photonics sensor is an on-chip optical tuning element. This element is used to shift the transmission curve of the sensor across a fixed-wavelength input. This tuning behaviour arises from the ability to electrically control the effective index of the waveguide. This can be done with two methods: thermal tuning, and plasma dispersion.

Thermal tuning arises from the temperature dependence of the refractive index. A generated change in temperature (ΔT) will change the refractive index of silicon (Δn) according to the thermo-optic coefficient of silicon.²¹

$$\Delta n(\text{at } 1550 \text{ nm}) = 1.8 \times 10^{-4} \Delta T \quad (3)$$

There are several common heater types in silicon photonics, both based on resistive heating. The first uses metallic heaters placed above (or to the side of) the silicon waveguide. A voltage is applied across the metal, causing a current to flow through, and the metal will heat up. The heat will then transfer through the oxide layers to the silicon beneath. The second method uses the silicon waveguide itself as the resistor. In this case, the silicon waveguide is doped (which will add additional losses to the waveguide). Contacts are placed on both sides of the waveguide, and a voltage is once again applied, allowing current to flow. In this case, the silicon waveguide itself will heat up.

The second method to control the effective index of silicon is through the plasma dispersion effect. This effect describes the dependence of the refractive index of silicon (Δn) on the carrier densities of electrons or holes (ΔN and ΔP , respectively, in $[\text{cm}^{-3}]$), given by:²²

$$\Delta n(\text{at } 1550 \text{ nm}) = -5.4 \times 10^{-22} \Delta N^{1.011} - 1.53 \times 10^{-18} \Delta P^{0.838} \quad (4)$$

As noted above, doping the waveguide will incur additional losses. The change in the absorption is given by:

$$\Delta \alpha(\text{at } 1550 \text{ nm}) = 8.88 \times 10^{-21} \Delta N^{1.167} + 5.84 \times 10^{-20} \Delta P^{1.109} \quad (5)$$

There are several types of phase shifters based on the plasma dispersion effect, including carrier depletion and carrier injection. In the depletion case, the waveguide is doped to have a pn-junction at zero bias. By applying a reverse bias to the waveguide, a depletion region will form at the pn-junction, thus depleting carriers in the waveguide. The width of the depletion region (W), which is dependent on the doping concentrations (N and P for electrons and holes, respectively) and applied voltage (V), is given by:²³

$$W(V, N, P) = \sqrt{\frac{2\epsilon_r\epsilon_o}{q} \frac{(N + P)(V_b - V)}{NP}} \quad (6)$$

where ϵ_r and ϵ_o are the relative permittivities of silicon and free space, respectively, q is the fundamental charge, and V_b is the built in voltage potential, given by:

$$V_b = \frac{kT}{q} \log\left(\frac{NP}{n_i^2}\right) \quad (7)$$

where k is the Boltzmann constant, T is temperature, and n_i is the intrinsic carrier concentration.

In the carrier injection phase shifter, the waveguide is doped to have a PIN structure. When the waveguide is forward biased, carriers will be injected into the intrinsic region, thus altering the refractive index. The PIN structure benefits from eliminating excess optical loss when the waveguide is unbiased.

For all phase shifter designs, the effective index of the waveguide will change depending on the applied bias. Here, we will refer to this change in effective index due to an applied voltage as the phase shifter efficiency. In this report, we will focus specifically on the pn-junction phase shifter design.

3.3 Silicon photonic sensor design

Our proposed low-cost sensor design is displayed in Figure 1. Here, we use a fixed-wavelength laser as the optical source, which is input to an MZI. One arm of the MZI acts as the sensor, and can be exposed to the analyte, while the other arm acts as the tracker, as it contains a phase shifter tuning element. The output of the MZI is detected with a single photodetector. Initially, the arms of the MZIs are balanced. When the voltage applied to the phase shifter is scanned, the effective index in that arm will change, resulting in a phase shift. This causes the output transmission detected by the photodetector to fluctuate between constructive and destructive interference, resulting in a sinusoidal output. When the sensor is exposed to an analyte, the effective index in its arm will also shift, adding an additional phase shift to that arm. Now, when the phase shifter voltage is scanned, the points of constructive and destructive interference will have shifted, according to the phase shift. By measuring the voltage shift in the phase shifter, the change in effective index of the sensing arm can be extracted.

Here, we can see that we need a reliable way to convert the applied voltage to a change in effective index of the phase shifter (phase shifter efficiency), and a conversion for the change in effective index of the sensor arm to a change in the cladding index (waveguide mode sensitivity). Unfortunately, both of these metrics for conversion are subject to fabrication variations.

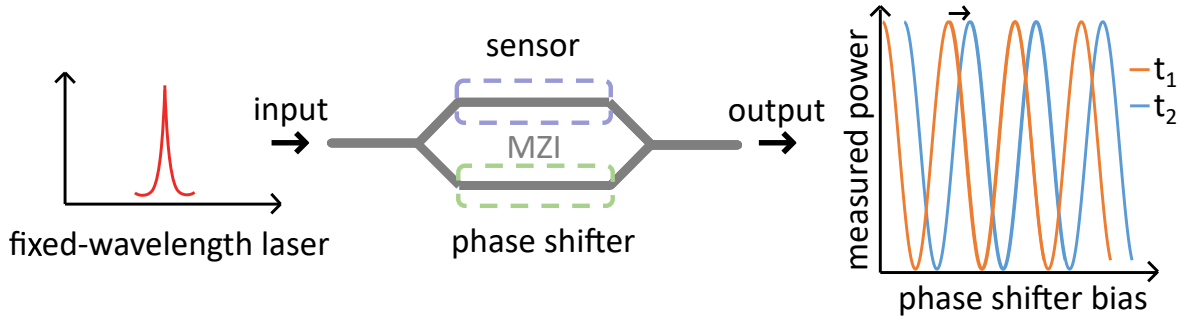


Figure 1. Silicon photonic sensor design using a fixed-wavelength laser and an MZI. The output signal is read as a function of phase shifter bias, and the shift can be seen from t_1 and t_2 , corresponding to before and after analyte exposure in the sensor arm.

Figure 2 displays the layout of the sensor as it was designed for fabrication on chip. The MZI arms were designed to be separated from one another to keep the microfluidic area away from the rest of the design. Likewise, the grating coupler, photodetector, and electrical contact pads for the phase shifter are also placed 500 μm , 700 μm , and 650 μm away from the open oxide area, respectively. The total area of the MZI was 90 μm \times 470 μm , excluding the grating coupler, photodetector, and electrical contacts.

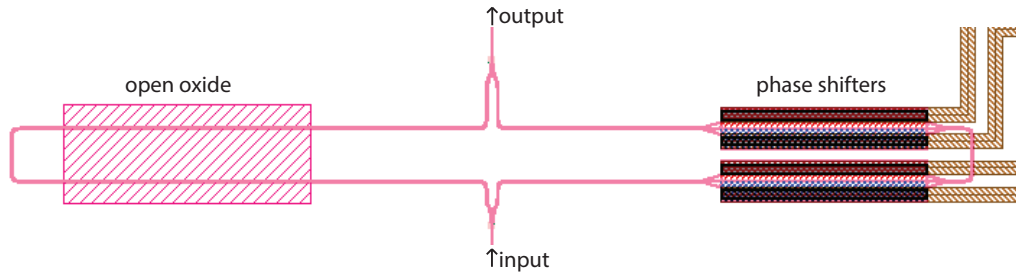


Figure 2. The layout of the proposed sensor design, which can be used to extract variations in device performance due to fabrication variations. The grating coupler, electrical contacts, and photodetector are not shown here, as they are spaced farther away from the main device.

No design variations were included for this design. Although the length of the sensor/phase-shifter arms could be adjusted, including this as a design variation would not be helpful in investigating fabrication variations across the wafer. A single design, with MZI arm lengths of 505 μm , which included oxide-open sensor and phase shifter lengths of 200 μm , was designed (in future designs, a small path difference should be included to compensate for differences in effective indices of the sensor and phase shifter arms). Instead of adding design variations, the design shown in Figure 2 can be duplicated multiple times across the chip. With approximately 30 chips across the wafer, and often two wafers (with different lithography processes) in a single multi-project wafer (MPW) fabrication run, this should provide close to 200 duplicate devices placed at different locations across the wafers. Practically, it would be quite time consuming to measure each device, since each device would require microfluidics and electrical contacting, which is not automated. Initially, devices that are spaced far apart should be measured, as these are expected to have larger fabrication variations.

4. WAVEGUIDE MODE SENSITIVITY VARIABILITY

Our first set of simulations aim to determine the waveguide mode sensitivity variations due to changes in manufacturing. While other work has characterized how variations in width and height will effect the the effective index of the waveguide,¹⁸ the effects they have on the the waveguide mode sensitivity has not been analyzed. In this section, we run simulations to characterize these effects.

We use a mode solver to calculate the effective index of the waveguide for the fundamental transverse electric (TE) mode in a strip waveguide for various widths, heights, and cladding indices. Fig. 3 shows the cross-section of the waveguide with width, height, and refractive indices labelled. Fig. 4 displays the simulated effective index for various waveguide widths, height, and cladding index. From this figure, we see that effective index varies by over 10% across these parameters.

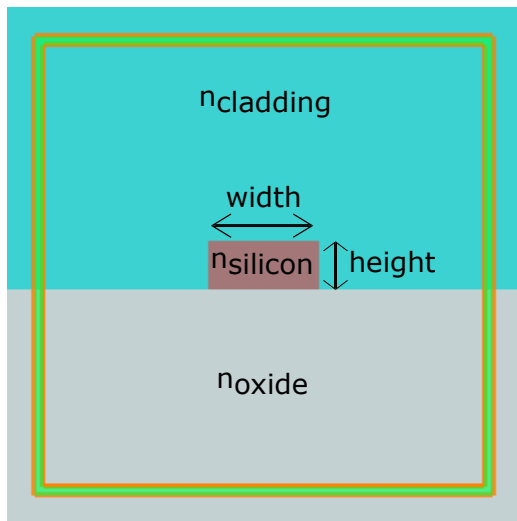


Figure 3. Cross-section of the waveguide, with width, height, and refractive indices labelled.

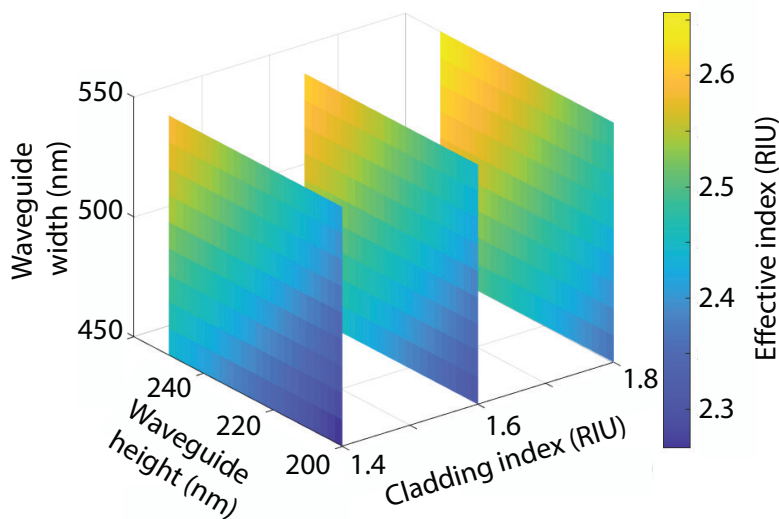


Figure 4. Effective index of a fundamental transverse electric strip waveguide as a function of waveguide width, height, and cladding index.

We can extract the waveguide mode sensitivity by taking the change in the effective index due to the change in cladding index for each width/height combination. Fig. 5 displays the results. Here, we see that the waveguide mode sensitivity can vary by over 70% across these width/height variations.

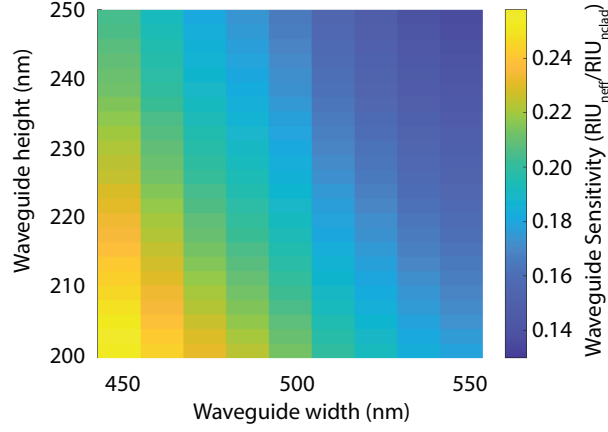


Figure 5. Waveguide mode sensitivity as a function of waveguide width and height, extracted from the results displayed in Fig. 4.

We can use the data from Fig. 5 to extract a function for the sensitivity based on the width and height of the waveguide. Approximating it as a linear function, the sensitivity (S) can be given as:

$$S(h, w) = m(h) \times w + c(h) \quad \text{or} \quad S(h, w) = m(w) \times h + c(w) \quad (8)$$

where w and h are the width and height of the waveguide (in nm), and m and c describe the slope and constant for a linear fit. Here, we can fit the sensitivity to a curve as a function of width and height. We do this by plotting sensitivity versus height (or width) for different widths (or heights) as shown in Fig. 6a, for sensitivity versus waveguide height. Each curve is fit to a line, with the slope and constants extracted for each waveguide width. Next, we fit the slopes and constants as a function of waveguide width to extract a linear equation, as shown in Fig. 6b. From these curves, we extract:

$$m(h) = 2.693 \times 10^{-6} \times h - 0.001391 \quad \text{and} \quad c(h) = -0.002312 \times h + 1.096 \quad (9)$$

for $m(h)$ and $c(h)$ and:

$$m(w) = 2.693 \times 10^{-6} \times w - 0.002312 \quad \text{and} \quad c(w) = -0.001391 \times w + 1.096 \quad (10)$$

for $m(w)$ and $c(w)$. We can see when Equations 9 and 10 are input into either versions of Equation 8, we obtain the same result:

$$S(h, w) = 2.693 \times 10^{-6} \times h \times w - 0.001391 \times w - 0.002312 \times h + 1.096 \quad (11)$$

While there is some error in this equation due to the linear approximation of sensitivity, this equation provides a reasonable approximation for the waveguide mode sensitivity at various heights and widths.

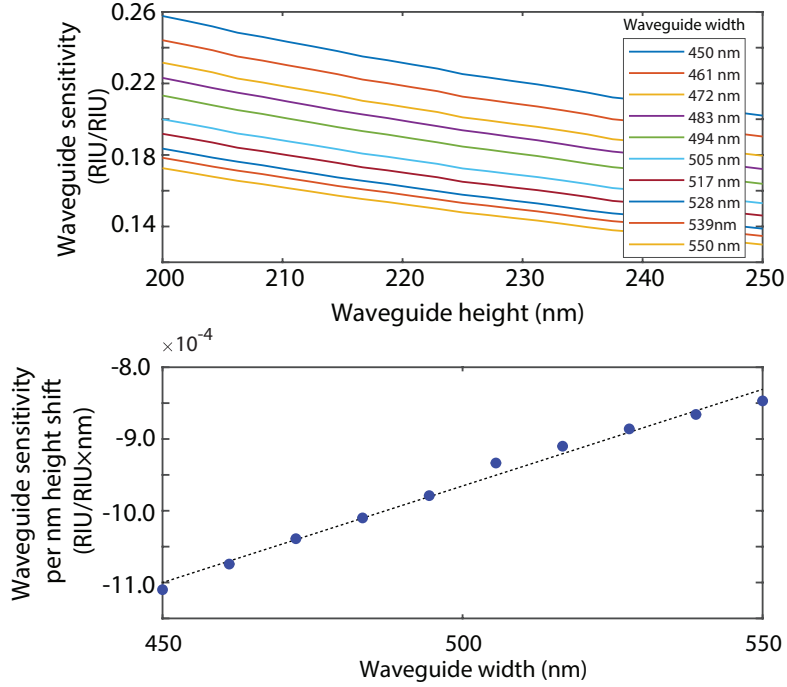


Figure 6. a) Waveguide mode sensitivity versus waveguide height, for different waveguide widths, as shown in the legend. For each width, the curve is linearly fit, and the slope and constants are extracted. b) The slopes extracted from a) as a function of waveguide width.

5. PHASE SHIFTER EFFICIENCY VARIABILITY

In this section, we analyze the effects that fabrication variations can have on the pn-junction phase shifter. Specifically, we will see how changes in the doping concentration can effect the phase shifter efficiency. As described by Equations 6 and 7, the depletion width of the pn-junction is highly dependent on the doping concentrations. Furthermore, the efficiency of the phase shifter is highly dependent on the depletion region, as the depletion of carriers will effect the refractive index, according to Equation 5.

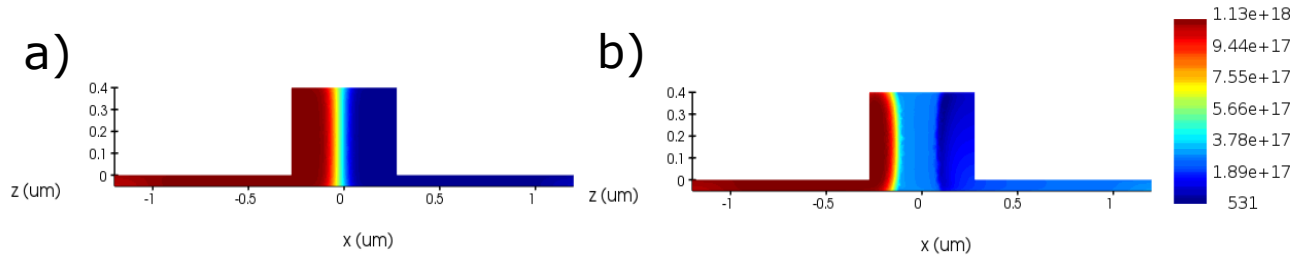


Figure 7. Electron dopant profiles for the cross-section of the waveguide at a) 0 V bias, and b) -4 V bias.

Anslys Lumerical’s CHARGE was used to simulate the doping profile at different bias points, and for different dopant concentrations. The nominal implant doping concentrations were $1.5 \times 10^{17} \text{ cm}^{-3}$ and $2.5 \times 10^{17} \text{ cm}^{-3}$ for electrons and holes, respectively. Fig. 7a shows the electron dopant profile at the cross section of the waveguide at zero bias. When a reverse bias is applied, as in Fig 7b, the dopant profile shifts.

We can then load the dopant profiles into Lumerical’s MODE solver, to calculate the effective index of the waveguide at various bias points. From this, we can extract the phase shifter efficiency, in RIU/V. Next, we repeat this process at different dopant concentrations, ranging from -15% to 15% the nominal concentration value. Fig. 8 displays the results of extracting the phase shifter efficiency at each doping concentration. The phase shifter efficiency (η) as a function of change in dopant concentration (ΔD in % units) can be given by:

$$\eta = 1.2 \times 10^{-7} \Delta D + 2.6 \times 10^{-5} \tag{12}$$

This assumes a linear correlation, which is fairly accurate over a small range. If larger variations occur in the dopant concentrations, a nonlinear fit should be applied.

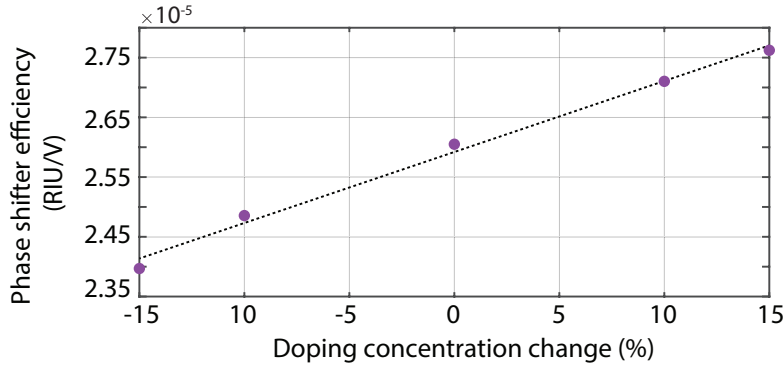


Figure 8. Phase shifter efficiency as a function of change in the doping concentration.

6. SENSOR SYSTEM EFFECTS

Finally, we can combine the variations outlined in the previous sections to see how the sensor performance may be altered by fabrication variations. In a low-cost system that shifts the transmission spectrum rather than scanning the laser wavelength, the shift in transmission of the sensor will be measured as shifts in voltage applied to the tuning component. To convert this change in voltage (ΔV) to change in RIU, we use the following conversion:

$$\Delta \text{RIU} = \frac{\eta}{S} \times \Delta V \tag{13}$$

where η is the phase shifter efficiency, and S is the waveguide mode sensitivity. Here, we assume that the length of the sensor arm and the length of the phase shifter are equivalent, therefore a change in effective index from the sensor or phase shifter arm will produce the same phase shift in the interferometer.

Assuming no variations in the width, height, or doping concentration, the η value will be 2.6×10^{-6} RIU/V, and the sensitivity will be 0.177 RIU/RIU, giving a conversion of $\Delta \text{RIU} = 1.47 \times 10^{-5} \Delta V$. This implies that if we measure a voltage shift of 1 V, the refractive index of the cladding has shifted by 1.47×10^{-5} RIU. However, height, width, or doping concentration variations will change this conversion. For example, if the sensitivity shifts to 0.2 RIU/RIU, a 1 V shift will correspond to a 1.3×10^{-5} RIU shift; however, without the knowledge of the new sensitivity, it will still be read as 1.47×10^{-5} RIU. This corresponds to 11% error in the RIU value.

The combined variations of waveguide width, height, and doping concentration is visualized in Fig. 9. This figure displays the voltage shift required to track a 0.001 RIU shift in the cladding. Here, we see the voltage requirements vary quite dramatically, up to 93% across the entire range of variations used in this report. This 93% difference is higher than what we would expect to see in fabricated devices, as the height and width variations are typically smaller than the range investigated here.

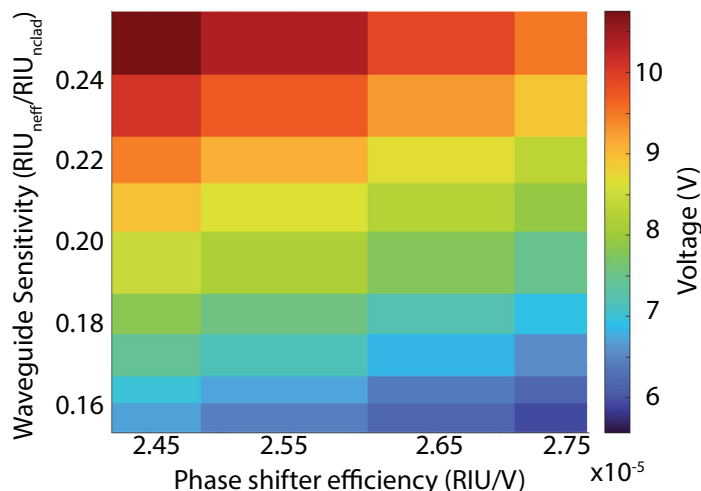


Figure 9. The phase shifter applied voltage required to track a 0.001 RIU shift in the cladding, as a function of waveguide sensitivity and phase shifter efficiency.

Nevertheless, this demonstration illustrates the need to characterize each sensor system before using it for real analyte detection. Without the individual characterization of each sensor, the conversion from volts to RIU would be made using the nominal conversion, which will lead to inaccuracies in the reported results. The waveguide sensitivity and phase shifter efficiency values need to be extracted for each sensor device in order to make the proper conversion.

The phase shifter efficiency could be extracted by scanning the voltage and measuring the voltage requirement for a 2π phase shift. The corresponding change in effective index can then be calculated using Equation 1. By dividing the change in effective index by the change in voltage, the phase shifter efficiency can be extracted, assuming a linear phase shifter response.

The waveguide mode sensitivity is somewhat more difficult to extract, and would require the use of a solution with a known refractive index. Before being used with real analytes, the sensor should be exposed to the known solution, and the change in phase can be extracted. Once again, using Equation 1, the change in effective index can be calculated. By dividing the change in effective index by the known change in refractive index of the solution, the waveguide sensitivity could be extracted.

Finally, the variations included here are just a few of the possible variations that can occur in such designs. For a waveguide, there is also possible variations in the sidewall angle of the waveguide, which will also impact the effective and group indices. For the phase shifter, doping mask position, waveguide height/width, and waveguide loss are other fabrication variations that could effect the phase shifter efficiency. Further investigations are necessary to fully characterize all these effects.

7. CONCLUSION

While silicon photonic sensors show the potential to impact global healthcare, there are still significant manufacturing challenges, which can lead to variability in device performance. In this report, we simulated potential fabrication variations, and analyzed their effect on the overall design performance. Waveguide mode sensitivity variations can arise from variations in the waveguide width and height. Furthermore, phase shifter efficiency is highly dependent on the dopant concentrations, and will also vary if these concentrations fluctuate. When implemented together in a low-cost silicon photonic sensor architecture, these variations can cause false interpretation of the results from the sensor, up to a 93% difference, using the variations in this report. This 93% difference is higher than what we would expect to see in fabricated devices, as the height and width variations are typically smaller than the range investigated here. Nevertheless, fabrication variations do still occur, and the results here highlight the need for initial calibration steps before using these sensors for analyte detection.

REFERENCES

- [1] Mascini, M. and Tombelli, S., “Biosensors for biomarkers in medical diagnostics,” *Biomarkers* **13**(7-8), 637–657 (2008).
- [2] Dhawan, A. P., Heetderks, W. J., Pavel, M., Acharya, S., Akay, M., Mairal, A., Wheeler, B., Dacso, C. C., Sunder, T., Lovell, N., et al., “Current and future challenges in point-of-care technologies: a paradigm-shift in affordable global healthcare with personalized and preventive medicine,” *IEEE journal of translational engineering in health and medicine* **3**, 1–10 (2015).
- [3] Flueckiger, J., *Enhancing the performance of silicon photonics biosensors*, PhD thesis, University of British Columbia (2017).
- [4] Gohring, J. T., Dale, P. S., and Fan, X., “Detection of her2 breast cancer biomarker using the opto-fluidic ring resonator biosensor,” *Sensors and Actuators B: Chemical* **146**(1), 226–230 (2010).
- [5] Chakravarty, S., Lai, W.-C., Zou, Y., Drabkin, H. A., Gemmill, R. M., Simon, G. R., Chin, S. H., and Chen, R. T., “Multiplexed specific label-free detection of nci-h358 lung cancer cell line lysates with silicon based photonic crystal microcavity biosensors,” *Biosensors and Bioelectronics* **43**, 50–55 (2013).
- [6] Chen, Y.-J., Xiang, W., Klucken, J., and Vollmer, F., “Tracking micro-optical resonances for identifying and sensing novel procaspase-3 protein marker released from cell cultures in response to toxins,” *Nanotechnology* **27**(16), 164001 (2016).
- [7] Sterlin, D., Mathian, A., Miyara, M., Mohr, A., Anna, F., Claër, L., Quentric, P., Fadlallah, J., Devilliers, H., Ghillani, P., et al., “Iga dominates the early neutralizing antibody response to sars-cov-2,” *Science translational medicine* (2020).
- [8] Soref, R., “The past, present, and future of silicon photonics,” *IEEE Journal of selected topics in quantum electronics* **12**(6), 1678–1687 (2006).
- [9] Chrostowski, L., Dias, L., Mitchell, M., Mosquera, C., Luan, E., Al-Qadasi, M., Randhawa, A., Mojaver, H. R., Lyall, E., Gervais, A., et al., “A silicon photonic evanescent-field sensor architecture using a fixed-wavelength laser,” in [*Optical Interconnects XXI*], **11692**, 116920W, International Society for Optics and Photonics (2021).
- [10] Estevez, M.-C., Alvarez, M., and Lechuga, L. M., “Integrated optical devices for lab-on-a-chip biosensing applications,” *Laser & Photonics Reviews* **6**(4), 463–487 (2012).
- [11] Chao, C.-Y. and Guo, L. J., “Biochemical sensors based on polymer microrings with sharp asymmetrical resonance,” *Applied Physics Letters* **83**(8), 1527–1529 (2003).
- [12] Zhou, X., Zhang, L., and Pang, W., “Performance and noise analysis of optical microresonator-based biochemical sensors using intensity detection,” *Optics express* **24**(16), 18197–18208 (2016).
- [13] Jokerst, N., Royal, M., Palit, S., Luan, L., Dhar, S., and Tyler, T., “Chip scale integrated microresonator sensing systems,” *Journal of biophotonics* **2**(4), 212–226 (2009).
- [14] Dias, L., Luan, E., Shoman, H., Jayatilleka, H., Shekhar, S., Chrostowski, L., and Jaeger, N. A., “Cost-effective, cmos-compatible, label-free biosensors using doped silicon detectors and a broadband source,” in [*CLEO: Applications and Technology*], ATu4K-5, Optical Society of America (2019).

- [15] Song, J., Luo, X., Tu, X., Park, M. K., Kee, J. S., Zhang, H., Yu, M., Lo, G.-Q., and Kwong, D.-L., “Electrical tracing-assisted dual-microring label-free optical bio/chemical sensors,” *Optics express* **20**(4), 4189–4197 (2012).
- [16] Bogaerts, W., Fiers, M., and Dumon, P., “Design challenges in silicon photonics,” *IEEE Journal of Selected Topics in Quantum Electronics* **20**(4), 1–8 (2013).
- [17] Selvaraja, S. K., *Wafer-scale fabrication technology for silicon photonic integrated circuits*, PhD thesis, PhD thesis, Ghent University (2011).
- [18] Lu, Z., Jhoja, J., Klein, J., Wang, X., Liu, A., Flueckiger, J., Pond, J., and Chrostowski, L., “Performance prediction for silicon photonics integrated circuits with layout-dependent correlated manufacturing variability,” *Optics express* **25**(9), 9712–9733 (2017).
- [19] Chrostowski, L., Wang, X., Flueckiger, J., Wu, Y., Wang, Y., and Fard, S. T., “Impact of fabrication non-uniformity on chip-scale silicon photonic integrated circuits,” in [*Optical Fiber Communication Conference*], Th2A–37, Optical Society of America (2014).
- [20] Luan, E., Shoman, H., Ratner, D. M., Cheung, K. C., and Chrostowski, L., “Silicon photonic biosensors using label-free detection,” *Sensors* **18**(10), 3519 (2018).
- [21] Frey, B. J., Leviton, D. B., and Madison, T. J., “Temperature-dependent refractive index of silicon and germanium,” in [*Optomechanical technologies for Astronomy*], **6273**, 62732J, International Society for Optics and Photonics (2006).
- [22] Nedeljkovic, M., Soref, R., and Mashanovich, G. Z., “Free-carrier electrorefraction and electroabsorption modulation predictions for silicon over the 1–14- μm infrared wavelength range,” *IEEE Photonics Journal* **3**(6), 1171–1180 (2011).
- [23] Bogaerts, W. and Chrostowski, L., “Silicon photonics circuit design: methods, tools and challenges,” *Laser & Photonics Reviews* **12**(4), 1700237 (2018).